CHEMICAL REVIEWS

REVIEW

pubs.acs.org/CR

Plasmons in Strongly Coupled Metallic Nanostructures

Naomi J. Halas,[†,‡,§] Surbhi Lal,[†] Wei-Shun Chang,[‡] Stephan Link,[†,‡] and Peter Nordlander*[,†,§]

[†]Department of Electrical and Computer Engineering, [‡]Department of Chemistry, and [§]Department of Physics and Astronomy, Rice University, Houston, Texas 77005, United States

CONTENTS

1. INTRODUCTION

The vivid optical properties of noble metal nanoparticles have been an object of fascination since ancient times. The ruby red of stained glass windows arises from gold nanoparticles, formed by the reduction of metallic ions in the glass-forming process. While these properties have been known and used for centuries, our scientific understanding of these properties has emerged far more recently, beginning with the development of classical electromagnetic theory. Gustav Mie's application of Maxwell's equations to explain the strong absorption of green light by a subwavelength gold sphere under plane wave illumination established the rigorous scientific foundation for our understanding of this phenomenon.[1] The following decades saw increasing interest in the properties of light scattering by small particles, and in particular, the properties of small metallic nanoparticles, whose collective electronic resonances, known as plasmons, give rise to the strong optical absorption properties of this class of materials.[2−4]

An even more dramatic optical property of metallic nanoparticles is their color change when a dilute suspension of nanoparticles aggregates. This can be seen when molecules or ions, such as a solution of NaCl, or molecular linkers, such as hemoglobin or DNA, are added to a suspension of noble metal nanoparticles. In the case of gold colloid, upon the onset of aggregation, a dramatic red-to-blue color change can easily be seen. When gold or silver nanoparticles begin to aggregate, they form pairs of nanoparticles and their optical spectrum acquires a new peak, red-shifted significantly from the spectral peak of the absorption for the isolated nanoparticle. For a fully aggregated solution, the red-shifted peak dominates the spectrum (Figure 1A).[5] This phenomenon, commonly witnessed by colloidal chemists, requires an understanding of the electromagnetic properties of interacting metallic nanoparticles in close mutual proximity.[5−8]

Special Issue: 2011 Plasmonics

Received: February 18, 2011
Published: May 04, 2011

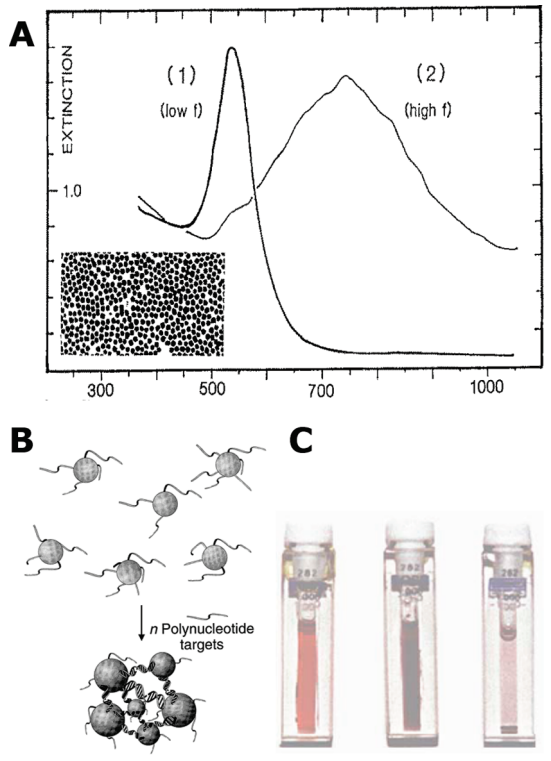

Figure 1. (A) Optical spectra of (1) a sparse Au nanoparticle (d = 20 nm) film and (2) a dense Au nanoparticle film, showing red-shifted plasmon resonance due to interparticle coupling (inset shows TEM image of the film).[5] (B) Schematic representation of oligonucleotide aggregates following hybridization with oligonucleotide molecules (not to scale).[9] (C) Suspensions of (left) a dispersed colloid, (middle) a linked colloid, and (right) linked, fully aggregated nanoparticles.[10] Reprinted with kind permission from refs 5, 9, and 10. Copyright 1991 Springer (ref 5), Copyright 1997 AAAS (ref 9), and Copyright 1996 Nature Publishing Group (ref 10).

The simplest description of this interaction, the coupling of two nearby oscillators, is in the coupling of two nearby dipoles. The interaction energy is given by $V \propto p_1 p_2 / r^3$ where p_1 and p_2 are the magnitudes of the dipole moments and r is the interparticle distance. This interaction energy is sufficiently strong in the case of nearly adjacent metallic nanoparticles to shift their resonant frequencies, resulting in new red-shifted and blue-shifted resonances relative to the resonance of each individual nanoparticle. For the case of two adjacent metallic spheres, the lower-energy resonance corresponds to two longitudinally aligned dipoles, giving rise to the strong red-shifted absorption peak in the optical spectrum. For the higher energy resonance, the coupled dipoles cancel each other, resulting in a resonance with essentially a zero net dipole moment that does not interact with incident light and does not appear in the optical absorption of the particle pair. Higher order multipoles can also contribute to this interaction, depending on nanoparticle size and interparticle distance. While the case of a large, extended ensemble of closely packed, disordered nanoparticles is significantly more complex, the dipole−dipole interaction and red-shifting of the spectrum seen for a pair of nanoparticles captures its essential optical properties. The color change brought about by the close interactions between metallic nanoparticles is extremely robust; and by modifying the surface chemistry of the nanoparticles, it is highly useful for the detection of trace chemicals or biomolecules (Figure 1B).[9,10] The detection of nucleotides, proteins, and cells based on the red-to-blue color change has led to the development of a wide range of assays and tests for medical applications.[11,12]

In the past decade, our understanding of interactions between strongly coupled metallic nanostructures has greatly matured, resulting in a new theoretical paradigm and a host of new structures and novel applications. What has emerged is the ability to control and tailor optical properties, from the nanoscale to the macroscale, through the design and use of metallic nanostructures of various geometries.[13−15] The color-change effect just described, a simple example of the coupling of metallic nanostructures, serves as the starting point for this review. We will start by examining the unique light-focusing properties of strongly coupled plasmonic systems, properties that have resulted in an extraordinary increase in interest in these systems within the chemistry community. We will then describe a theoretical picture, plasmon hybridization (PH), that takes advantage of the analogy between plasmons and the wave functions of simple quantum systems to provide a simple, intuitive explanation of the properties of complex plasmonic systems. We then examine a broad range of geometries that give rise to strong plasmon coupling and their properties. Next, we look at coupled plasmonic systems where the classical electromagnetic description of coupled plasmons is no longer adequate and a quantum mechanical description is necessary to understand their behavior. This section is followed by a discussion of plasmons in extended systems, such as chains, arrays, and wires. We then review some very recent work on plasmonic Fano resonances. Finally, we discuss applications of coupled plasmonic systems, including the use of interacting plasmons for nanoscale metrology, as plasmon rulers, as surface-enhanced Raman and infrared spectroscopic substrates, and for localized surface plasmon resonance (LSPR) sensing. We conclude by speculating about plasmon coupling in future scientific research and technological applications.

2. PLASMON COUPLING

2.1. Nanoparticle Pairs and "Hot Spots"

An observation even more dramatic than the color change of colloidal aggregates is the ability of gold or silver nanoparticles, under certain conditions, to give rise to extraordinarily large enhancements of the Raman scattering spectra of adsorbed or adjacent molecules. The first reports of Raman scattering greatly enhanced by the presence of a metal substrate appeared in 1978, an effect that became known as surface-enhanced Raman scattering (SERS).[16] The million-fold enhancements initially reported by the discoverers of this effect were attributed largely to the excitation of surface plasmons of the metallic substrate,[17] with further enhancements by chemical effects. While the initial observations of SERS were indeed striking, they were followed in 1997 by reports of single-molecule detection using SERS that captured the attention of the scientific world.[18,19] The initial report of single-molecule SERS was obtained for silver colloid, "activated" by a low concentration of NaCl, with a dilute solution of methyl violet consistent with the detection of individual molecules. The possibility of obtaining chemical signatures of single molecules, with chemical spectroscopy at the sensitivity level of fluorescence, has the potential to elicit breakthroughs in fundamental chemistry at the single-molecule level, the study of biochemical pathways, and even the supramolecular chemical dynamics within living cells. However, the mystery behind these enormous enhancements, initially determined to be in the 10^{14} to 10^{15} range, was indeed complex. Based on analyses that had been performed for molecules adsorbed to metallic nanoparticles, the origin of these enhancements was unclear.

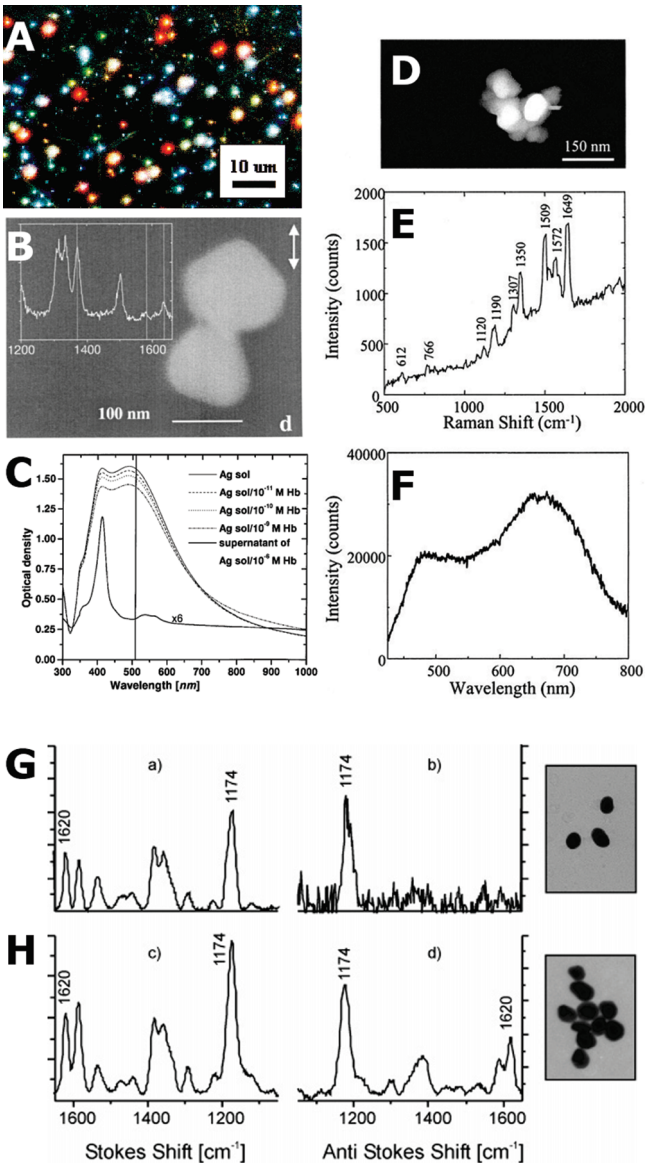

Figure 2. (A) Ag nanoparticles incubated with NaCl solution then imaged using dark field microscopy.[20] (B) Scanning electron microscope image of two adjacent Ag nanoparticles with a "hot spot" giving rise to the SERS spectrum of an individual hemoglobin molecule.[21] (C) Spectra of Ag nanoparticles dispersed in H_2O solution and spectra of aggregated Ag nanoparticles formed by the addition of Hb molecules to the solution.[21] (D) Ag nanoparticle cluster producing a "hot spot".[22] (E) SERS spectrum of a molecule obtained from a cluster.[22] (F) Dual-peaked spectrum of cluster aggregates.[22] (G, H) Stokes and anti-Stokes SERS spectrum of crystal violet obtained (G) from isolated Au nanoparticles and (H) from aggregated Au nanoparticles. Anti-Stokes spectrum shows increased enhancement by aggregated nanoparticles.[24] Reprinted with kind permission from refs 20−22 and 24. Copyright 1999 American Chemical Society (ref 20), Copyright 1999 American Physical Society (ref 21), Copyright 2000 American Chemical Society (ref 22), and Copyright 2006 American Chemical Society (ref 24).

As researchers began to investigate this effect, it soon became apparent that the extremely intense SERS signals were obtained from only certain specific nanoparticles. The optical extinction spectra of individual colloidal silver particles obtained with a dark field microscope revealed a remarkably heterogeneous distribution of particles, with widely varying spectral properties[20] (Figure 2A). When these were correlated with single-molecule SERS spectra of the same particles, it was discovered that virtually all the nanoparticles giving rise to SERS spectra themselves had complex, red-shifted, typically multiply peaked spectra,[20] not the blue-centered extinction spectrum of an isolated individual silver nanoparticle. From these observations, it was inferred that the extraordinary enhancements experienced by certain molecules were due to properties of strongly interacting metallic nanoparticles. This hypothesis was soon substantiated by direct measurements of single-molecule SERS at the individual nanoparticle or nanoparticle cluster level:[21,22] in these studies, it was independently observed that colloidal clusters as simple as two directly adjacent nanoparticles (Figure 2B−F) gave rise to a multiply peaked extinction spectrum and to a single-molecule SERS signal. Dense, not sparse, clusters produced a far greater enhancement of the anti-Stokes spectra of molecules (Figure 2G,H).[23,24]

From these pioneering experiments, it could be inferred that the junction between adjacent nanoparticles, occurring for pairs, larger clusters, or even aggregate films of nanoparticles, can give rise to highly intense and localized electromagnetic fields when excited by incident light of the appropriate polarization. In a near-field optical microscopy interrogation of a metal island film, these highly localized, high-intensity regions could be measured directly (Figure 3A).[25] From these studies, the interjunction regions were nicknamed "hot spots". While these high-intensity regions were observed for many complex nanocluster geometries, it became clear that the nearest-neighbor coupling between two adjacent metallic nanoparticles, not long-range or radiative coupling, was responsible for this electromagnetic focusing effect. In a combination single-particle Raman and AFM experiment, bright SERS signals resulting directly from adjacent nanoparticle pairs were identified (Figure 3B,C).[26] Electrodynamic calculations of an adjacent nanoparticle pair of the same material and geometry directly showed the intensity of the hot spot and its dependence on the polarization of incident light for its excitation (Figure 3D).[26]

These studies established a new and important property of directly adjacent nanoparticle pairs, their ability to focus light via plasmon excitation far below the diffraction limit of classical optics to volumes commensurate with the interparticle junction.[27−40] Further experimental efforts concentrated on the development of nanojunctions or "nanogaps" using methods developed from other fields, such as molecular electronics (Figure 3E). The ability to fabricate nanoscale gaps that could be spanned by a single molecule existed in these fields; using the same approaches to develop nanojunctions for SERS was very promising. As a result of this approach, single-molecule SERS could be correlated with other single-molecule measurements, specifically molecular conductance (Figure 3F).[41,42] Electromigrated junctions were fabricated that showed a strong and simultaneous correlation between blinking in the SERS spectrum of an individual molecule and its conductance fluctuations. Recent work has established more accurate assessments of the electromagnetic fields within nanoscale junctions, the enhancements required for single-molecule SERS, and a range of innovative approaches that has enabled the fabrication of sub-10-nm junctions by numerous methods, for more detailed studies of these systems.

2.2. A Theory for Interacting Plasmons: Plasmon Hybridization

Although a variety of computational tools have been developed for modeling the electromagnetic properties of metallic nanostructures,[43−49] an analytical theoretical method has also

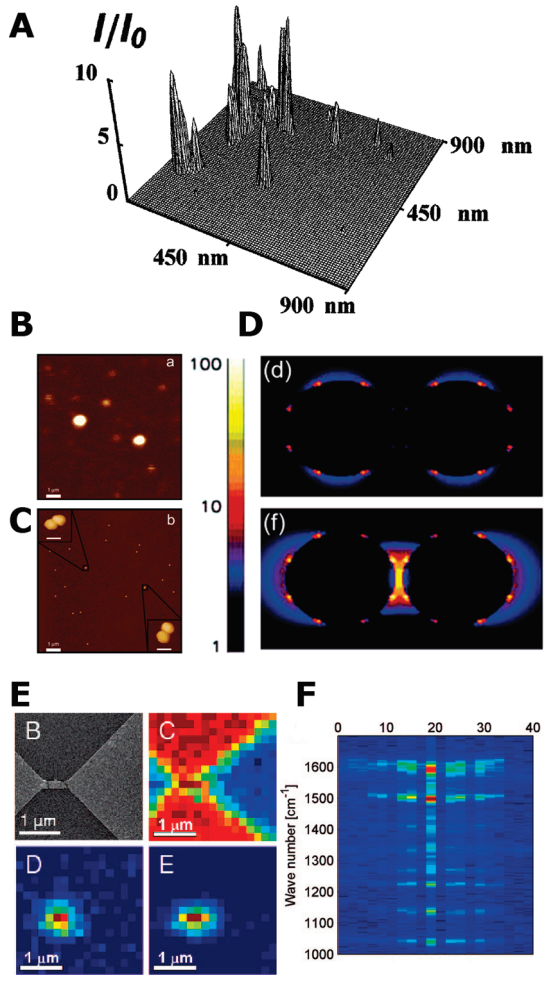

Figure 3. (A) Scanning near-field optical microscope image of hot spots in a metal island film;[25] (B) hot spots in a Raman image of Au nanoparticles arising from (C) condensed nanoparticle pairs;[26] (D) FDTD calculations of adjacent nanoparticle pairs showing a hot spot in the junction for incident polarization along the interparticle axis; for incident polarization orthogonal to the interparticle axis, no hot spot occurs;[26] (E) nanoscale gaps formed by electromigration show a SERS hot spot; (F) blinking observed in single-molecule SERS arising from an electromigrated gap correlates with single-molecule conductance fluctuations.[42] Reprinted with kind permission from refs 25, 26, and 42. Copyright 1999 American Physical Society (ref 25), Copyright 2005 American Chemical Society (ref 26), and Copyright 2008 American Chemical Society (ref 42).

been developed that provides a physically intuitive picture of coupled plasmons in complex nanostructures.[50] In the plasmon hybridization method, the plasmon modes of a complex nanostructure are expressed in terms of interactions between the plasmon resonances of its elementary components. The hybridized plasmon modes obtained are formed in rigorous analogy with the formation of molecular orbitals from the hybridization of individual atomic wave functions in molecular orbital theory. This method provides a simple and conceptually straightforward understanding of how plasmon resonances in a complex or multicomponent structure arise from the plasmon modes of their individual components. Since its initial demonstration, this approach has been utilized for the analysis of an ever larger variety of plasmonic systems.[51−70]

In the plasmon hybridization approach, the conduction electrons of a nanostructure are treated as if they were an incompressible, irrotational fluid of uniform electron density, confined to a uniform positive background with dielectric permittivity ε_∞. The incompressible deformations of a fluid are described by its velocity field $\vec{v}(\vec{r})$ which represents the velocity $\vec{v}$ of a volume element at position $\vec{r}$. Incompressible deformations are expressed as the gradient of a scalar potential that satisfies the Laplace equation. One can find a complete set of such scalar potentials $\phi_\mu(\vec{r})$, where μ is an index for the individual basis functions, in any given geometry. For example, for an individual nanoparticle in a spherical geometry, μ would denote the multipolar indices (l, m); in a planar geometry, μ would be the parallel wavevector. An arbitrary deformation of the electron fluid in a multicomponent structure can therefore be written as

$$\vec{v}(\vec{r}) = \sum_{i\mu} \frac{\mathrm{d}}{\mathrm{d}t} A_{i\mu}(t) \nabla \phi_{i\mu}(\vec{r}) \qquad (1)$$

Here $|i\mu\rangle$ is the primitive plasmon mode m on nanoparticle i, with its velocity field $\nabla\phi_{i\mu}(\vec{r})$ and time-dependent amplitude $\mathrm{d}(A_{i\mu}(t))/\mathrm{d}t$. The primitive plasmon amplitude $A_\mu(t)$ describes the spatial displacement of the primitive plasmon $|\mu\rangle$. Due to the incompressibility of the electron gas, deformations result in surface charges on the nanostructure.

In a complex geometry, such as multiple coupled nanoparticles or a multilayer nanoparticle, the primitive plasmon modes interact via the Coulomb potential and are therefore no longer the eigenmodes of the system. To obtain the normal modes of the coupled system, harmonic motion for all modes is assumed, and self-sustained solutions are sought, that is, modes that exist with finite amplitude in the absence of an external applied field. The energies of the primitive plasmons of the coupled system can then be calculated directly from their velocity fields. Surface charge distributions, in particular screened charges that also take into account the background dielectric permittivities, must also be included. The potential energy of this system will contain nondiagonal elements due to the coupling of the primitive plasmon modes through the Coulomb interaction. The new eigenmodes of the coupled system are obtained by diagonalizing the Lagrangian for this system. The resulting hybridized modes will therefore be superpositions of the individual primitive plasmon modes. From the equations of motion, the optical absorption of the complex coupled nanostructure can be calculated.

2.3. Thin Films and Complex Nanoparticles

The analogy between coupled plasmonic systems and molecular orbital theory is extremely useful in understanding interacting plasmonic systems of increasing complexity. In this section, we discuss the plasmon modes of several structures that have been fabricated and studied by numerous groups, focusing on the picture provided by this description of the resonant energies of these systems.

2.3.1. Nanoparticle Pairs: "Dimers". For the case of two directly adjacent nanoparticles illuminated by light polarized along the interparticle axis, the mutual coupling between the plasmons of each individual nanoparticle is well described by the hybridization picture (Figure 4A). In this case, the nanoparticle pair and its spectrum of mode energies closely resemble its electronic analog, a homogeneous diatomic molecule, and its molecular orbital diagram. Based on this parallelism, coupled metallic nanoparticle pairs are referred to as plasmonic "dimers", and the red-shifted collective plasmon mode is referred to as the

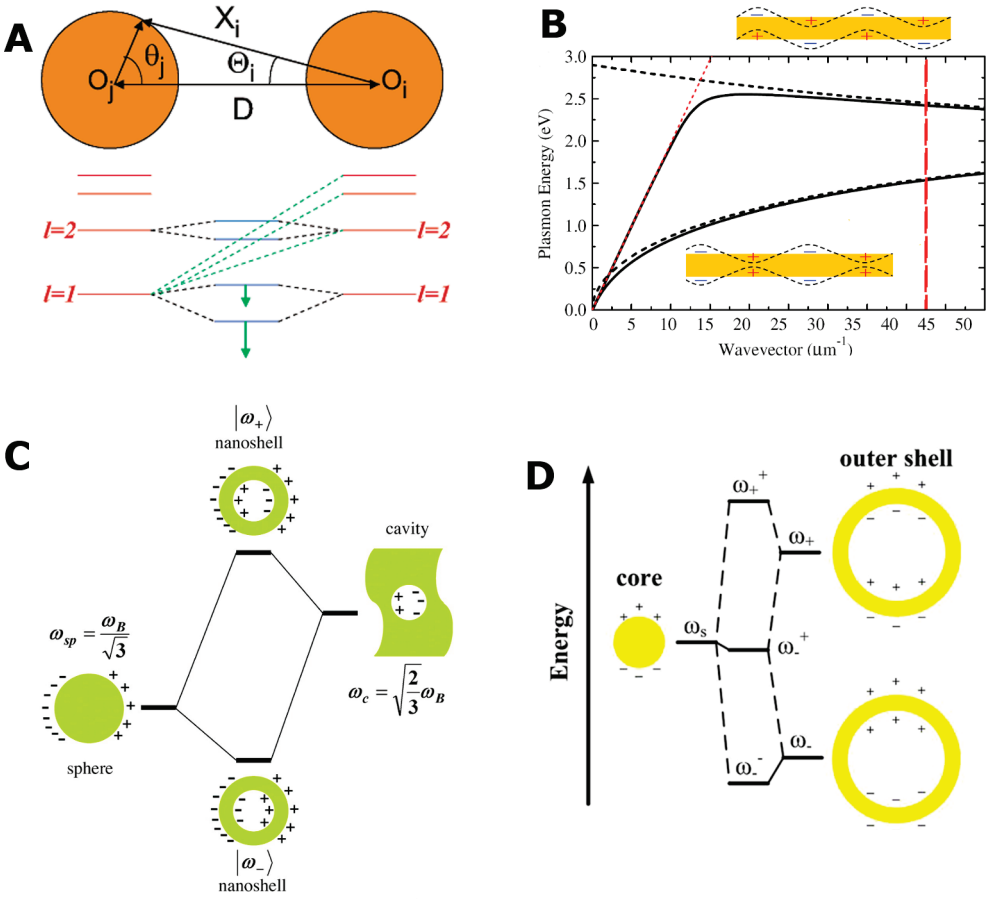

Figure 4. (A) Schematic picture illustrating the plasmon hybridization in a nanoparticle dimer. The individual nanosphere plasmons on the two particles interact and form bonding and antibonding dimer plasmons. In the dimer geometry, nanosphere plasmons with a given angular momentum l interact also with plasmons of different angular momentum on the other particle at small interparticle distances.[112] (B) Exact retarded calculation of the bonding and antibonding film plasmon dispersion. Insets show schematic surface charge density distribution for the bonding (bottom) and antibonding (top) film plasmon.[75] (C) An energy-level diagram describing the plasmon hybridization in metal nanoshells resulting from the interaction between the sphere and cavity plasmons. The two nanoshell plasmons are an antisymmetrically coupled (antibonding) plasmon mode and a symmetrically coupled (bonding) plasmon mode.[50] (D) Plasmon hybridization diagram for a gold−silica−gold layered nanoparticle.[60] Reprinted with kind permission from refs 50, 60, 112, and 75. Copyright 2004 American Chemical Society (ref 112), Copyright 2009 Elsevier (ref 75), Copyright 2003 AAAS (ref 50), and Copyright 2009 Springer (ref 60).

"bonding" plasmon mode. In Figure 4A, the plasmonic dimer and its collective modes are shown. The dipolar (l = 1) plasmon mode of each individual nanoparticle is split into two distinct collective modes, known as the low-energy "bonding" mode and the higher-energy "antibonding" mode. As discussed earlier, these two modes differ in their coupling to incident light: the lower-energy mode has mutually aligned longitudinal dipoles, resulting in a mode with a large induced dipole and a strong coupling to the far field. Hence the optical properties of a plasmonic dimer are dominated by its bonding plasmon. Such radiative modes, modes that couple well to the far field, are known as "bright" plasmon modes. The higher energy l = 1 collective dipolar mode is known, in analogy with molecular systems, as the "antibonding" plasmon mode. Here the dipoles on each individual nanoparticle are antialigned, resulting in no net dipole moment and the inability of this mode to couple to the far field. This is an example of a "dark" or "cavity-like" mode. Also shown here is the mixing between the l = 2 quadrupolar modes of the individual nanoparticles, which would be observable in the limits of small interparticle distance and larger nanoparticle size. In the limit where the nanoparticles are nearly touching, mixing between the l = 1 states and all higher order modes of the neighboring nanoparticle will occur.[71] The resulting hybridization results in an increased redshift of the bonding l=1 dimer mode with decreasing dimer separation. This behavior is characteristic of a dimer excited by light polarized along its interparticle axis. For light polarized orthogonal to this axis, interparticle coupling is minimal, and a small blue shift of the individual nanoparticle plasmon is observed.[72−74]

2.3.2. Thin Metallic Films. An important system of coupled plasmons that is relevant to many plasmonic geometries is that of a thin metallic film (Figure 4B).[75] For this structure, the primitive plasmon modes are the freely propagating surface plasmons on the top and bottom metal−dielectric interfaces of the metal film. The Coulomb interactions between the surface charges that arise due to deformations of the electron fluid, under the constraint of its incompressibility, result in two coupled plasmon modes between the upper and lower metal interfaces. The lower-energy "bonding" plasmon has the positive and negative charges aligned symmetrically on either side of the film, whereas the higher-energy "antibonding" plasmon corresponds to an antisymmetric charge distribution. These charge configurations and their

corresponding mode energies are counterintuitive: one would anticipate that the symmetric charge distribution has the greater Coulomb repulsion and therefore corresponds to the higher energy mode. In the plasmon hybridization picture, the charge distribution of a primitive plasmon on one side of the film sets up a secondary charge distribution on the opposite side of the film, due to the incompressibility of the electron fluid. When this secondary attractive charge distribution is taken into account, the symmetric mode is found to be the lower-energy mode (Figure 4B, insets).

2.3.3. Nanoshells. The symmetric configuration of the charge distribution for the lowest mode of an infinite film also holds for a thin metallic film around a spherical dielectric core. This dielectric core/metallic shell geometry is known as a nanoshell (Figure 4C).[76−80] The plasmonic properties of this nanostructure can be understood as the hybridization of the surface plasmons on the inner and outer surfaces of the metallic shell layer. This interaction, mediated by the thickness of the shell layer, determines the mode energies: the shell thickness corresponds to the interparticle distance of a plasmonic dimer, following the same scaling law.[72] In a nanoshell, the lowest energy mode has a symmetric charge distribution similar to that of the thin film plasmon. The thin metallic layer of a core−shell nanoparticle can also be thought of as the hybridization of two simpler plasmons, of a solid metallic sphere and of a cavity. In the nanoshell case, this distribution results in a strong induced dipole for this lowest energy mode, making this bonding mode the bright mode of the two hybridized plasmons. The higher-energy mode corresponding to an antisymmetric charge distribution has a much smaller dipole moment and is therefore a dark mode.

2.3.4. Nanomatryushka. The sphere−cavity hybridization picture that describes the energies and charge distributions for a nanoshell can be generally applied to multilayer metallodielectric core−shell nanoparticles. Two such systems involve a particle with a metallic core, a dielectric (silica) layer, and a metallic shell (Figure 4D)[59,60,81,82] or a silica−gold nanoshell embedded inside another silica−gold set of layers.[50,83] Both these structures are known as nanomatryushkas (a matryushka is a nested set of dolls found in Russian folk art). In the case of a solid metal core nanomatryushka, the nanoparticle possesses hybridized modes due to mixing between the bonding plasmon of the nanoshell with the nanosphere mode. This hybridization gives rise to two bright modes. The antibonding mode, when the dipole moment of the inner sphere oscillates in phase with that of the shell layer, has the strongest absorption of any mode in this system. The lowest energy bonding mode is produced by the coupling of the nanoshell bonding mode out-of-phase with the nanosphere mode. This also produces a bright mode but with significantly lower intensity. The third mode, which is composed of the antibonding mode of the nanoshell coupled to the nanosphere mode, has only very weak coupling and is therefore designated a nonbonding mode. For larger multilayered nanoparticles, hybridization occurs between the quadrupolar ($l = 2$) plasmon modes independently of the dipolar modes; however, the lowest-energy hybridized quadrupolar mode can appear at lower energies than the highest-energy dipolar hybridized mode. The presence of multiple overlapping modes in this concentric-sphere geometry gives rise to coherent coupling effects, such as Fano resonances: this topic will be discussed in a subsequent section of this review.[82]

2.3.5. Coupled Nanorods. A system of nanoparticles with interesting coupling properties is that of two coupled nanorods. A single nanorod possesses two orthogonal plasmon resonances, a long wavelength longitudinal plasmon for light polarized along its long axis and a shorter wavelength transverse plasmon, for light polarized orthogonal to the nanorod long axis. Two nanorods can interact with each other in an orientationally dependent manner. Surface charge plots of two interacting nanorods are shown in Figure 5A. In each of the cases illustrated here, the plasmon response is highly polarization dependent. For end-to-end coupling with incident polarization along the interparticle axis, the nanorod dimer plasmon is red-shifted strongly from its uncoupled energy. For side-to-side coupling, shown here for the case of polarization along the long axis of the nanoparticles, a small blue shift of the collective plasmon mode occurs. This behavior is consistent with the behavior of a spherical dimer. Additionally in this system, changes in orientation of one nanoparticle with respect to the other can be studied: both a T-shaped dimer and an L-shaped dimer can be constructed. Each of these configurations yields two orthogonal modes. Modes where the polarization is perpendicular to the junction are strongly red-shifted, as in the spherical dimer case. For the opposite polarization, the mode energies are perturbed only slightly: for the T-configuration, they are red-shifted, but for the L-configuration, they are slightly blue-shifted. Rod−rod coupling is in general much weaker than its spherical analog, requiring small (1−2 nm) interparticle distances for appreciable mode shifting to be observed. A detailed hybridization diagram has been developed for interrod coupling that identifies the mode energies of all these interactions.[58,84]

2.3.6. Nanostars. One important aspect of the plasmon hybridization picture is its usefulness in understanding the plasmon modes of highly complex and irregular geometries. This can be seen in a study of the plasmonic modes of a nanostar (Figure 5B). Nanostars are multipointed noble metal nanoparticles, each with its own individual highly complex multipeaked spectrum. A general understanding of the modal properties of these highly irregular particles can be obtained by deconstructing a nanostar into its component parts, in this case a central, spherical core and a collection of rodlike tips. The hybridized modes of this structure arise due to the coupling between the core and tip plasmon modes. Although the plasmon hybridization method is analytical, it can still be applied to a structure as complex as this one, by relying on electromagnetic simulations of the deconstructed components, such as those obtained by the finite-difference time domain method, and by analyzing the symmetry and the charge distributions obtained for modal identification. This serves as an illustrative example of how the plasmon hybridization picture can be adapted to plasmonic systems of arbitrary complexity to understand and interpret numerical simulation results in terms of the underlying modes of the structure.[85]

2.3.7. Transverse Excitations, Magnetic Atoms, and Metamaterials. The previously discussed case of coupled nanorods addressed orientational effects; however, there is another excitation mode in these systems that is of great interest in the development of metamaterials. Specifically, the case of two adjacent nanorods aligned in a transverse orientation gives rise to two types of collective excitations, where the oscillating dipoles are in phase and where the dipoles are in antiphase (Figure 5C). This configuration of two stacked antiphase nanorods is also known as a "magnetic resonance".[86−89] This is because the currents in the two wires, combined with the displacement currents between the wires, result in a resonant excitation of the magnetic dipole moment of this structure at or near optical frequencies, for geometries at or near the nanoscale. This type of optical frequency magnetic response is essential for the development of negative refractive index materials in the frequency range corresponding

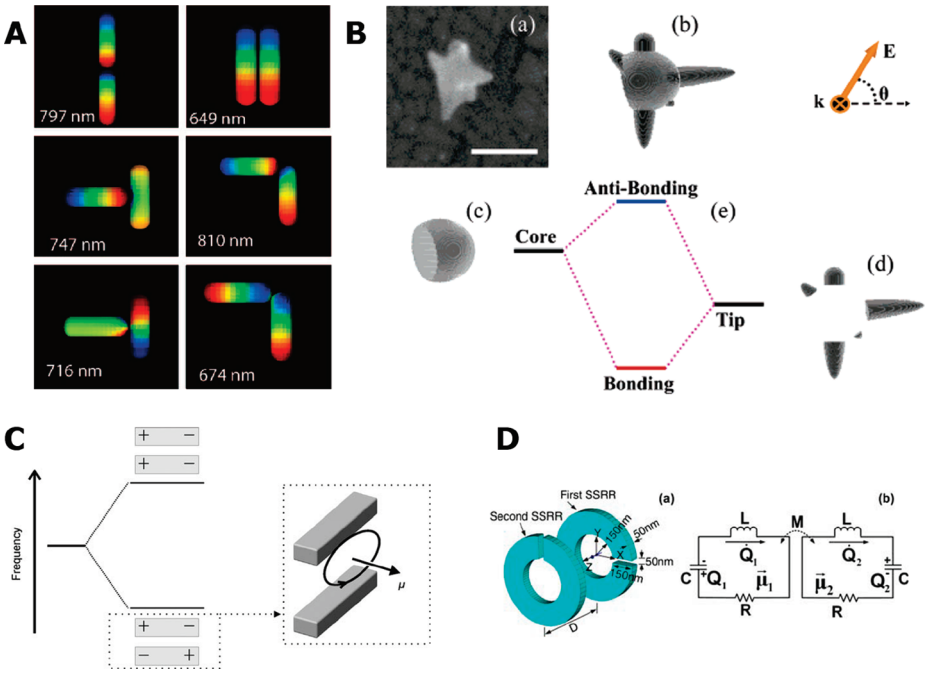

Figure 5. (A) Surface charge density of interacting cylindrical, spherically capped gold nanorods placed 1.5 nm apart and with dimensions 78 nm × 24 nm, calculated using the electrostatic approximation, where blue represents one charge and red the opposite charge of the dipole. The plasmon resonance for a single rod of these dimensions calculated using this method is 707 nm. The wavelength shown is the resonance wavelength for the coupled plasmon mode.[58] (B) A gold nanostar: (a) an experimental scanning electron micrograph; the scale bar is 100 nm; (b) theoretical model, consisting of (c) a truncated spherical core and (d) tips consisting of truncated prolate spheroids; (e) hybridization diagram for this nanostructure. The core plasmons interact with the tip plasmons and form bonding and antibonding nanostar plasmons. The polarization angle is defined in the upper right corner.[85] (C) Transverse coupling of two coupled metallic nanorods or nanowires. A magnetic dipole moment can be excited in the antisymmetric mode, so the structure behaves as a magnetic "atom".[90] (D) (left) Two adjacent split-ring resonators (SRRs) interact through magnetic dipole−dipole coupling; (right) an equivalent circuit model can be developed to describe the behavior of these and other coupled plasmonic systems.[51] Reprinted with kind permission from refs 58, 85, 90, and 51. Copyright 2009 American Chemical Society (ref 58), Copyright 2007 American Chemical Society (ref 85), Copyright 2010 (ref 90), and Copyright 2009 (ref 51) Wiley-VCH Verlag GmbH &Co. KGaA.

to this resonance (typically the infrared or visible region of the spectrum), since magnetic responses cannot occur at such high frequencies in naturally occurring materials. This stacked two-wire structure has been dubbed a "magnetic atom" and is considered one of the fundamental building blocks of metamaterials. Other geometries with an optical frequency magnetic moment include u-shaped metallic structures, as well as cut-ring structures; these and other variants are known as split-ring resonators (SRRs). These types of structures can simultaneously possess both magnetic and electric dipoles; therefore, elucidating their properties requires that both electric and magnetic dipolar coupling be taken into account.[90] In Figure 5D, a configuration of two adjacent split-ring resonators separated by a distance D is shown. This is a magnetic dimer,[51] where the hybridization and coupling occurs due to the magnetic dipole−dipole interaction between the structures. An equivalent circuit model for the magnetic dimer is also shown, illustrating another useful analog for plasmonic systems, the analogy between coupled plasmons and coupled lumped-element resonant circuits.

2.4. Nanoparticle over a Surface

Metallic nanoparticle interactions with a nearby substrate or surface represents a class of systems of fundamental importance and of great utility in applications.[59,91−104] The presence of any substrate, dielectric, semiconducting, or metallic, breaks the symmetry of the nanoparticle environment and has a strong influence on the modes of the nanoparticle. Here we consider the basic physics of the nanoparticle−substrate interaction in several contexts, the role of plasmon interactions, and the properties of several coupled nanoparticle−substrate systems.

A metallic nanoparticle placed near any substrate will be attracted to it, through the image charges induced in the substrate by its presence. For the case of a dielectric substrate where no plasmons exist, the image charges are weak, screened by the factor $(\varepsilon - 1)/(\varepsilon + 1)$ where ε is the permittivity of the substrate medium. This weak interaction can be sufficient to break the symmetry of the dielectric environment of the nanoparticle, lifting the degeneracy between its plasmon modes.[105] For the case of a metallic nanoparticle near a metallic substrate, this interaction is much stronger: a nanoparticle interacting with the surface plasmons in an infinite metallic substrate is similar, in many aspects, to a nanoparticle dimer. The interaction with its image charges alone will red shift the nanoparticle plasmon for light excitation polarized perpendicular to the metallic surface. In addition to the image-like interactions, there is a strong interaction between the localized plasmons of the nanostructure and the propagating plasmons of the substrate. While this problem has been examined using a variety of approaches,[106−112] we will use the plasmon hybridization picture to obtain an understanding of this coupled system.[111,112] Hybridization in this system produces either a red shift or a blue shift in the nanoparticle plasmon, depending on the relative energies of the nanoparticle and surface plasmons. A schematic of this interacting system is shown in Figure 6: the nanoparticle induces

dx.doi.org/10.1021/cr200061k |*Chem. Rev.* 2011, 111, 3913–3961

a set of attractive image-like charges in the metal (Figure 6A) and the (l = 1 and l = 2) localized plasmons of the nanoparticle hybridize with the surface plasmons of the extended metal. The reduced symmetry of this geometry enables an effective hybridization of the dipolar and quadrupolar plasmons of the nanoparticle. The hybridized plasmon energies are a strong function of the distance, Z, between the nanoparticle and the metallic surface, decreasing in energy strongly with decreasing particle−surface separation. Because the Coulomb potential is the same as in the dimer case, the distance dependence of this red shift closely resembles the interparticle distance dependence of the plasmon energies of a plasmonic dimer for larger Z distances. However, the plasmon red shift is faster when the nanoparticle approaches a surface than when it approaches an equivalent nanoparticle. This is because of contributions from higher-order angular momentum states of the nanoparticle plasmon that are weaker in the dimer case. This basic picture holds for the case where the surface plasmon of the substrate is at the same or higher energy than the localized surface plasmons of the nanoparticle. When that is not the case, such as if the surface and the particle were made of different plasmonic materials, that is, aluminum and gold, the hybridization picture changes significantly: a blue-shifting of the hybridized nanoparticle plasmons with decreasing particle−surface separation is anticipated.

This picture of particle−substrate coupling is altered significantly when the dimensions of the extended metallic substrate are reduced to the dimensions of the nanoparticle. This can be realized in the case of a plasmonic nanoparticle interacting with a thin metallic film or with a metallic structure confined in more than one dimension, such as a nanowire.[105,113−115] In these cases, the image-based interaction between the particle and the substrate is no longer a valid model. To address these regimes, one can apply the plasmon hybridization method to these systems. The case of a nanoparticle interacting with a metallic film substrate is depicted in Figure 6B. The interaction between the localized surface plasmons of a metallic nanoparticle and the propagating plasmons of a continuous underlying metallic substrate, such as a film or a nanowire, can be seen as the hybridization of the discrete plasmon modes of the nanoparticle with the continuum of plasmon modes of the underlying substrate. This is the electromagnetic analog of the spinless Anderson−Fano model, which describes the interaction between localized states in electronic systems, such as impurities, with a continuum of delocalized states, that is, the band structure of a metal.[116] An important aspect of the particle−substrate interaction in this case, which becomes clear from the plasmon hybridization picture, is the dependence of the particle−substrate coupling on the density of continuum states of the substrate. For example, as the thickness of the film substrate is decreased, the nature of the coupling between the particle plasmon and the underlying substrate is modified. The particle−film hybridized states change in character, depending on this interaction. This model describes (1) the image-like interaction of a nanoparticle with a metallic film of thickness much larger than the particle diameter, (2) an intermediate regime where the particle diameter and film thickness are roughly equivalent, giving rise to hybridized broadened resonances, and (3) a regime where the film thickness is much smaller than the nanoparticle diameter, which gives rise to a resonant particle−film virtual state. The hybridized states in these mixed systems provide a mechanism for the efficient excitation of surface plasmons at specific energies associated with the hybridized

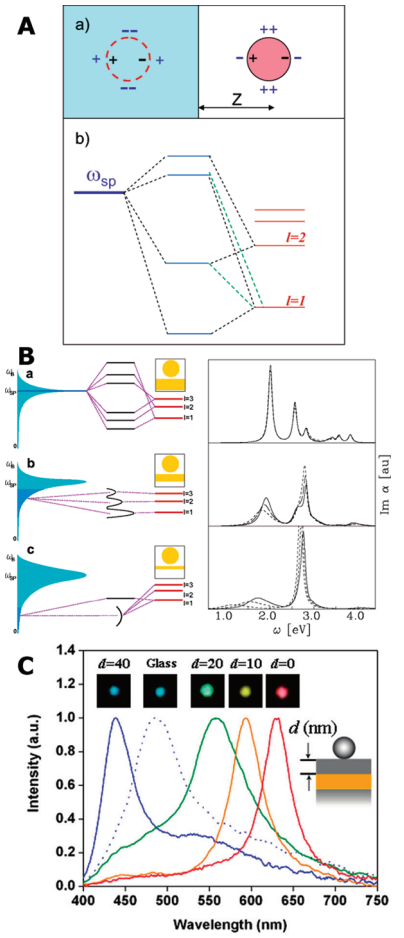

Figure 6. (A) Schematic illustrating the interaction of a nanosphere with a metallic surface. Panel a shows the image forces obtained assuming a perfect response of the surface for an l = 1 and an l = 2 sphere plasmon. The surface mediates an interaction between plasmons of different l, resulting in a distance-dependent hybridization of the nanosphere plasmons in a manner similar to the nanosphere dimer. Panel b shows plasmon hybridization in this system. The nanoparticle plasmons interact with the surface plasmons, resulting in shifts and an effective hybridization between nanoparticle plasmons of different angular momentum l.[111] (B) The three interaction regimes (a−c) for a plasmonic nanoparticle and the surface plasmons of a thin metallic film. For each case, the left panel illustrates the energetics of the interaction regime, while the right panel shows the corresponding calculated dipolar optical absorption spectrum for various film thicknesses corresponding to this regime. The plasmonic density of states is illustrated in light blue, the effective continuum of the film is illustrated in dark blue and the resulting hybridized plasmons are shown in black. (a) the regime corresponding to the thick film limit (much thicker than the nanoparticle diameter), where the effective continuum of the film lies at higher energies than the nanoparticle plasmon. (b) left panel: the intermediate regime (on the order of the nanoparticle diameter), where the nanoparticle plasmon is resonant with the effective continuum of the film. (c) the regime of the thin film limit (significantly smaller than the diameter of the nanoparticle), where the effective continuum of film plasmons lies at lower energies than the nanoparticle plasmon.[115] (C) Examples of optical scattering spectra for individual silver nanoparticles on a silica layer of varying thickness above a 50 nm gold film. Insets show a dark field image of each individual nanoparticle. The dotted spectrum represents an individual silver nanoparticle over a glass substrate.[97] Reprinted with kind permission from refs 111, 115, and 97. Copyright 2004, 2005, and 2010 American Chemical Society.

particle−continuum modes. Intense local fields or "hot spots" arise at these energies, resulting in large field enhancements similar to those obtained in the dimer geometry.

These three regimes of nanoparticle−thin film interaction are experimentally accessible and have been studied in a range of plasmonic systems. With dark field microscopy, the scattering spectra of individual 60 nm diameter silver nanoparticles above a 50 nm gold film, held off by a silica spacer layer of varying thickness, were studied. This material−geometry combination corresponds to a regime where the plasmon energies red shift strongly with decreasing nanoparticle−film distance. The scattering spectra in this progression span the entire visible spectrum (Figure 6C).[97] A nanoparticle−film geometry that approaches the thin film limit was used to construct individual nanoparticle−film hot spots and use them for surface-enhanced Raman spectroscopy (Figure 7A).[103] In this case, the virtual state formed by the particle−film interaction is responsible for the high-intensity local field obtained here that gives rise to extremely large SERS enhancements. The particle−film sandwich geometry, where the SERS-active molecules are sandwiched between the thin film and the nanoparticle, is ideal for SERS. Another regime yet to be studied in detail is that of nanoparticle−film coupling where the shape of the nanoparticle is varied. In this case, one would anticipate that the higher-order multipolar contributions to the particle−film interaction may be modified, but the basic properties of the junction would be largely independent of nanoparticle shape. This result was obtained experimentally for a wide variety of nanoparticle geometries in a SERS "sandwich" configuration (Figure 7B).[117]

2.5. Plasmonic Oligomers

Just as molecular orbital theory can be applied to complex, multiple-atom molecules, there has been interest in extending coupled plasmon systems beyond the plasmonic dimer to multi-nanoparticle systems, as "plasmonic artificial molecules". Two major strategies have been pursued for the synthesis/fabrication of these systems: chemical/physical assembly processes, and clean-room nanofabrication techniques. Both basic strategies can ultimately produce supramolecular plasmonic structures with strong interparticle coupling and collective effects. There has been interest in the optical properties of controlled plasmonic aggregates for some time,[8,118−124] and analyzing the plasmonic properties of clusters with more complex geometries than the nanoparticle pair is a topic of increasing interest.

The controlled chemical assembly of noble metal nanoparticle clusters or aggregates of well-defined particle number and geometry using traditional wet chemistry methods is a daunting challenge. Typically, when nanoparticle surface chemistry is modified to enhance the attraction between nanoparticles in solution or suspension, it is nonselective, resulting in nanoparticle aggregation. The extensive literature on the creation of aggregates by chemical methods is the subject of a recent comprehensive review.[125] To control this process in greater detail, such that only a pairwise dimer or a well-defined few-particle cluster such as a trimer, quadrumer, or tetramer is formed, requires additional methods to direct the assembly of the nanoparticle constituents. While the chemist's goal may be to achieve a single type of assembled entity in high yield, thus far, directed assembly has more often been used to construct well-defined clusters in very low yield (one or two structures) for further physical studies. The goal in this case is to characterize a specific assembled cluster by nanoscale imaging methods, such as

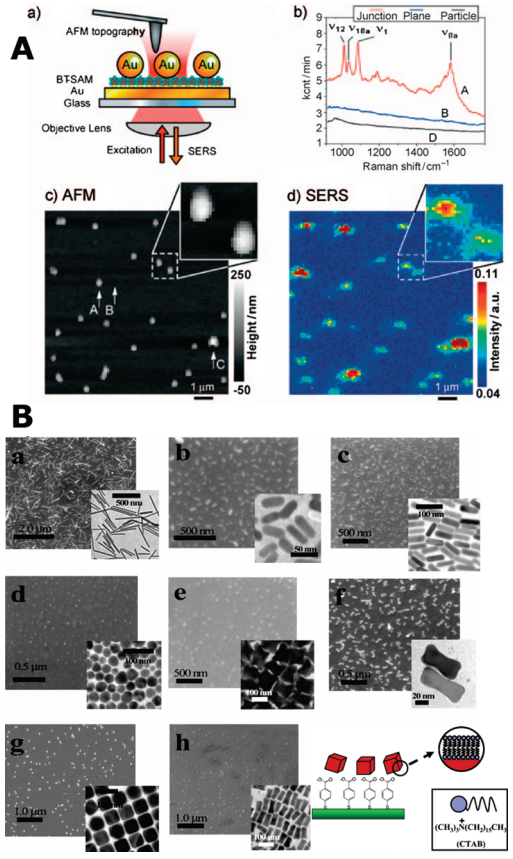

Figure 7. (A) (a) Experimental setup and sample structure. The AFM tip scans above the sample, and the illumination and detection are carried out in the epi-direction. (b) SERS spectra obtained from the nanoparticle−benzenethiol (BT)−plane junction position (red line, position A in panel c), BT−plane (blue line, position B in panel c), and a BT-coated gold nanoparticle on glass. (c) AFM topography and (d) confocal SERS images of the nanoparticle−BT−plane sample obtained simultaneously. The inset images in panels c and d are the magnified scans (1.3 μm × 1.3 μm) of the squared areas. The scale bars represent 1 μm length scale. The position C is an aggregate of nanoparticles (two or three) on the surface that produce visibly stronger SERS signals than average.[103] (B) SEM and TEM (inset) images of (a) aspect ratio 16 rods, (b) aspect ratio 3.2 rods, (c) aspect ratio 4.4 rods, (d) spheres, (e) tetrapods, (f) dogbones, (g) cubes, and (h) blocks immobilized on 4-mercaptobenzoic acid (MBA) SAMs and scheme of the nanoparticle−SAM sandwich geometry for SERS of 4-MBA.[117] Reprinted with kind permission from refs 103 and 117. Copyright 2008 (ref 103) Wiley-VCH Verlag GmbH &Co. KGaA and Copyright 2005 American Chemical Society (ref 117).

scanning electron microscopy or atomic force microscopy, and then to probe the structures optically at the individual cluster level (using dark field microscopy, electron energy-loss or cathodoluminescence techniques). This combination of detailed structural and physical data enables the direct and quantitative comparison with theory. This focus on the characterization of well-formed plasmonic clusters at the individual cluster level also makes clean-room methods, such as e-beam lithographic patterning, highly practical for the study and development of these types of systems.

One of the most promising approaches for the chemical assembly of plasmonic clusters is DNA-based assembly.[10,126,127] This approach has been used extensively in the formation of

DNA-based polyhedra, such as triangles, pyramids, and cubes.[128−132] To form plasmonic clusters, one chemically modifies the noble metal nanoparticle surfaces with specific strands of DNA. Single-stranded DNA with a terminal thiol group can exploit the remarkably strong bond between the thiol group and noble metals (126−46 kJ/mol for S−Au) and form a submonolayer on the nanoparticle surface. By functionalizing nanoparticles with specifically designed DNA sequences, the nanoparticles, when mixed, will form predesigned clusters as the DNA hybridizes. The double-stranded DNA will then serve as a linker molecule, spanning the interparticle distance. While there are challenges to this approach, such as maintaining high yield for specific cluster geometries and achieving interparticle distances that provide strong plasmon coupling, it appears to be a promising chemical method for constructing well-controlled and complex two- and three-dimensional plasmonic clusters. In Figure 8A, a DNA-assembled noble metal tetramer is shown.[133] This three-dimensional structure would be extremely difficult to make by alternate methods and is of interest in the development of isotropic optical frequency magnetic and negative index media (Figure 8B).[134] This synthetic approach has also been quite successful for the fabrication of plasmon rulers, discussed in the Applications section of this review.

Another useful strategy for the assembly of plasmonic clusters is template-guided chemical self-assembly.[135−138] This approach makes use of a substrate, patterned and passivated in certain regions to direct nanoparticles to specific areas and away from others, preventing the nonspecific deposition of nanoparticles on the sample. Functionalization of the patterned regions and of the nanoparticle surfaces can then facilitate electrostatic attraction between the particles and the deposition areas and assembly of clusters. A template showing a variety of clusters made by this method is shown in Figure 9.[139] Here the 40 nm diameter nanoparticles have been densely assembled, facilitating plasmon coupling, onto a thin, 10 nm Au film substrate patterned and functionalized to facilitate cluster formation. Modification of the cluster properties by the presence of this thin substrate layer will be needed to fully elucidate the coupled modes of these structures.

A simple plasmonic cluster beyond the dimer structure that has been synthesized and studied is a trimer structure, formed by three equilaterally placed plasmonic nanostructures.[121] The properties of this structure are already remarkably different from that of the plasmonic dimer and provide an initial introduction to these new nanoscale materials. Lithographically defined equilateral nanodisks have been fabricated that show significant plasmon coupling within the three-element structure (Figure 10A).[140] The optical spectrum of this cluster appears as a double-peaked band. The 3-fold symmetry allows us to take advantage of group theoretical analysis to identify the plasmon modes of the trimer in terms of the irreducible representations of the D_{3h} group (Figure 10B).[141] From the symmetry-adapted coordinates obtained from group theory, two in-plane modes with a net dipole moment, that is, the bright modes of the in-plane-excited trimer, can be identified as the two modes observed in the optical spectrum. Another approach to understanding the properties of trimer structures is examining how the properties of a plasmonic dimer are modified by the introduction of a third nanoparticle, toward the dimer interparticle junction (Figure 10C).[142] As the third nanoparticle approaches the dimer, a strong modulation in the excitation polarization is observed. This transition highlights one of the major differences between these two types of plasmonic clusters: the dimer maintains a strong polarization dependence of its optical spectrum, while a fully symmetric trimer has, by symmetry, a polarization-isotropic extinction spectrum.

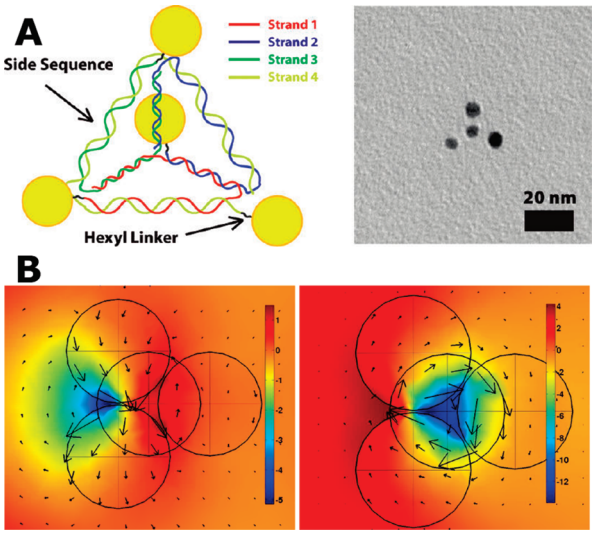

Figure 8. (A) Schematic and TEM image of DNA−nanocrystal pyramids.[133] (B) Field profiles at the two primary resonances of a tetramer consisting of four Au nanospheres of 80 nm diameter with interparticle spacing of 2 nm: (left) electric dipole resonance at λ = 756 nm; (right) magnetic dipole resonance at λ = 935 nm. Color shows intensity of the out-of-plane magnetic field, $\mathbf{H}_z$, in the plane containing centers of three spheres; arrows show in-plane electric induction (D^x,D^y) in the same plane (horizontal axis, x; vertical, y).[134] Reprinted with kind permission from refs 133 and 134. Copyright 2009 (ref 133) American Chemical Society and Copyright 2007 Optical Society of America (ref 134).

3. FROM THE CLASSICAL TO THE QUANTUM REGIME

The electromagnetic (EM) field enhancements in junctions between coupled metallic nanoparticles depend strongly on the widths of the gaps separating the nanoparticles. For spherical particles, the dimer modes red shift and the field enhancements increase monotonically with decreasing gap separation.[125,143−147] In surface enhanced spectroscopy (SES) applications such as SERS, it is therefore advantageous to use nanostructures with narrow gaps.[41,148−162] However, too narrow gaps may enable electron transfer between the two adjacent nanostructures.[42,58,155,163−173] When conductive overlap is established, the field enhancements are reduced and the energy of gap plasmons can be strongly shifted compared with the situation with no conductive overlap. For a proper description of the EM field enhancements in sub-nanometer gaps, it is therefore necessary to include quantum mechanical (QM) effects such as electron tunneling across the gap and nonlocal screening of the induced fields.

In this section, we will discuss theoretical modeling of the plasmonic properties of narrow gaps with an emphasis on quantum effects. We will start with a discussion of the classical modeling of the optical properties of touching nanoparticles. We will then discuss how the phenomenological inclusion of nonlocal effects can improve the classical modeling. We will then discuss fully quantum mechanical calculations of the optical properties, which provide a correct first principles modeling of the dielectric function, including both nonlocal and electron screening effects. This discussion will be followed by a description of a full QM modeling of the plasmonic properties of

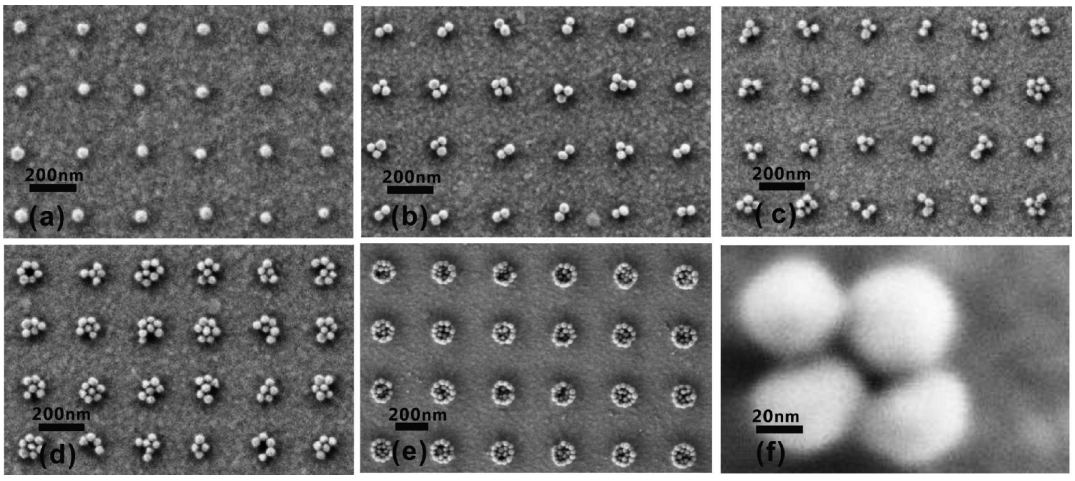

Figure 9. SEM images from extracts of nanoparticle cluster arrays with varying diameters of e-beam defined binding size D = 50 nm (a), 80 nm (b), 100 nm (c), 130 nm (d), and 200 nm (e). The SEM images confirm that through control of the diameter of the e-beam fabricated binding site, the cluster size can be continuously varied. The enlargement of an individual cluster in panel f shows junctions and crevices between nearly touching particles.[139] Reprinted with kind permission from ref 139. Copyright 2009 American Chemical Society.

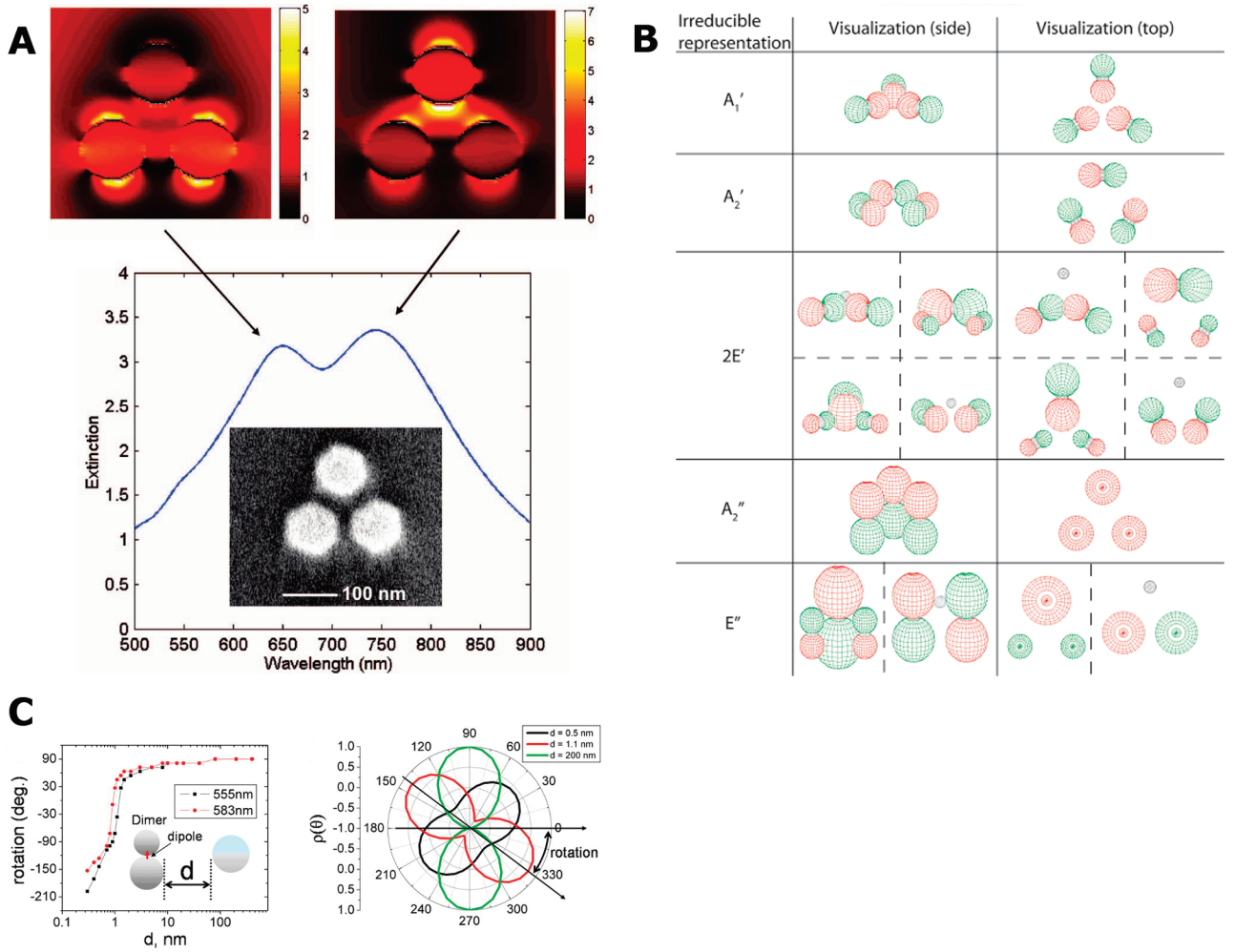

Figure 10. (A) A trimer of planar Ag nanodisks supports two plasmon resonances. The optical spectrum, electromagnetic calculations of the near-field at each resonance, and a scanning electron micrograph of the structure are shown.[140] (B) Group theory analysis of an equilateral nanosphere plasmonic trimer.[141] (C) Trimer formation as the perturbation of a plasmonic dimer: modifications in the spectrum and in the excitation polarization dependence are shown.[142] Reprinted with kind permission from refs 140−142. Copyright 2008 American Chemical Society (ref 140), Copyright 2006 American Chemical Society (ref 141), and Copyright 2008 National Academy of Sciences, U.S.A. (ref 142).

dx.doi.org/10.1021/cr200061k |*Chem. Rev.* 2011, 111, 3913–3961

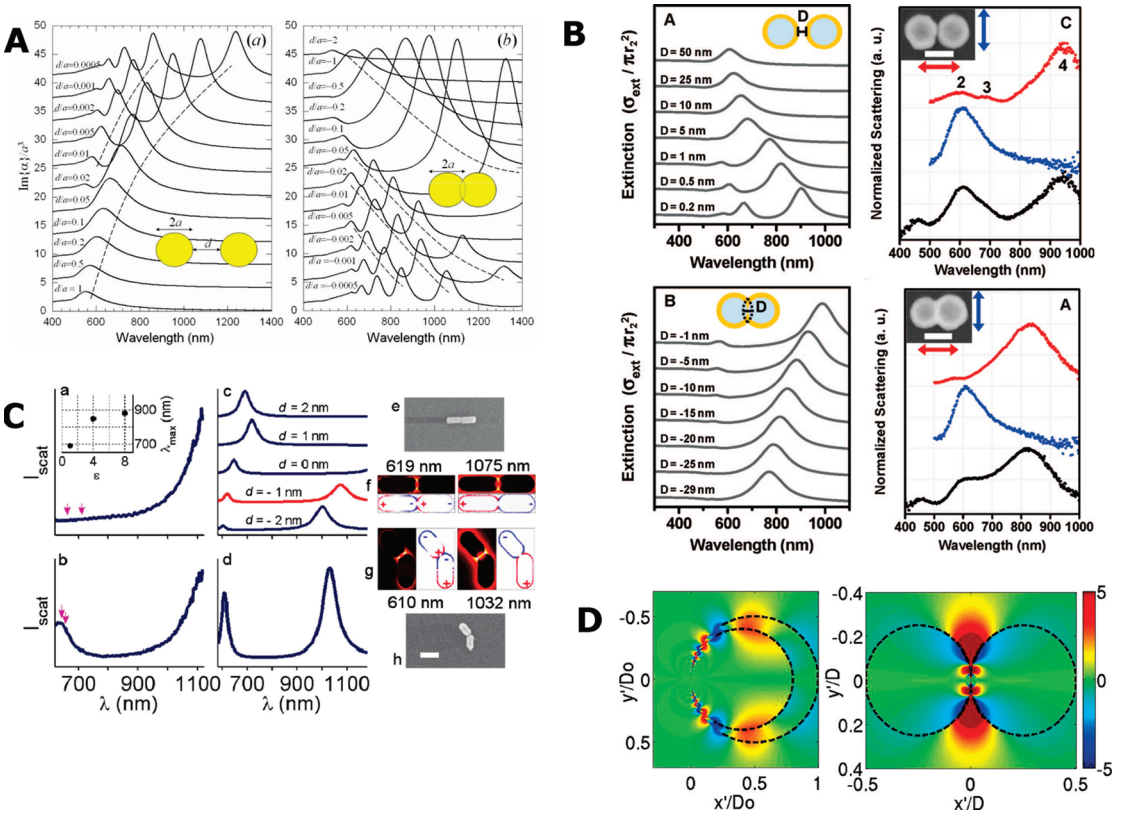

Figure 11. (A) Effect of conductive overlap on the optical properties of a touching gold nanosphere dimer.[174] (B) Effect of conductive overlap for a nanoshell dimer: (left) simulation; (right) experimentally measured scattering spectra.[176] (C) Effect of conductive overlap for a gold nanorod dimer: (left) measured scattering spectra; (middle) simulations; (right) SEM image and calculated electric field enhancements.[177] (D) Field enhancements for touching nanostructures calculated using transformation optics: (left) a touching nanocrescent; (right) touching nanocylinders.[180] Reprinted with kind permission from refs 174, 176, 177 and 180. Copyright 2006 (ref 174) Optical Society of America and Copyright 2008 (ref 176), 2010 (ref 177), and 2010 (ref 180) American Chemical Society.

nanoparticle dimers. We will then discuss the optical properties of nanoparticles connected by a conductive bridge as a platform for optical measurement of molecular conductance and as a device for efficient optical switching. Finally the section will be concluded by a brief discussion of the coupling between plasmonic nanoparticles and excitonic systems such as quantum dots.

3.1. Classical Electrodynamic Modeling of the Optical Properties of Touching Nanoparticles

In the classical approach, a nanoparticle is modeled by assigning a dielectric permittivity to its material. The nanoparticles are modeled as homogeneous objects with infinitely sharp surfaces. As the two nanoparticles approach each other, the capacitive coupling between the plasmon modes of each nanoparticle results in hybridized "dimer modes", which red shift monotonically with decreasing separation.[112] Due to the hybridization of the individual nanoparticle modes, dimer plasmons originating from dark quadrupolar and higher multipolar nanoparticle plasmon modes become visible in the spectrum because of the admixture of dipolar modes in their hybridized states.

The intrinsic problem with the classical modeling of the optical properties of touching nanoparticles was discussed by Romero et al. for the case of two touching gold nanospheres, shown in Figure 11A.[174] The left panel shows the evolution of the polarizability (absorption spectrum) as the nanoparticles are moved closer to each other. The bonding dipolar plasmon (BDP) of the dimer exhibits a monotonic red shift, and higher multipolar bonding dimer modes such as the bonding quadrupolar plasmon (BQP) appear in the spectrum. The right panel shows that when a conductive overlap is established between the two particles, the hybridized dimer modes begin to blue shift with increasing overlap. In addition, the intensity of the hybridized higher multipolar dimer modes begins to decrease. This blue shift and disappearance of the hybridized peaks is because of the decreased coupling of the individual nanosphere plasmons, due to the onset of electron transfer between the particles. This short-circuiting of the dimer junction reduces the EM coupling and the electric field enhancements. It is interesting to note that the spectra for $d = 0.0005$ and $d = -0.0005$, which corresponds to a separation difference of 0.6 Å are distinctly different. This discontinuity is an artifact of the classical model, which assumes that the surfaces of the nanospheres are infinitely sharp. For the touching nanoparticle dimer, the plasmonic wave function consists of a superposition of individual nanoparticle plasmons, just as in the nontouching case, and, in addition, the admixture of a charge transfer plasmon mode involving monopolar plasmon modes of each nanoparticle. These monopolar modes are enabled because electrons can transfer between the nanoparticles. The resulting dimer plasmon can be described as a charge transfer plasmon (CTP). Such a CTP will be enabled for any conductive overlap between the particles. For very small overlap, the CTP will be strongly red-shifted. The energy of the CTP is proportional to the conductance of the junction.[175]

Subsequent experimental and theoretical investigations of the optical properties of touching nanoshells were performed by Lassiter et al., as shown in Figure 11B.[176] The theoretical simulations displayed in the left panels show the extinction spectrum as a function of nanoshell separation for nontouching dimers. As for the nanospheres, a monotonic red shift with decreasing separation is apparent. For the touching nanoshells, the spectra blue shift with increasing overlap. The experimental spectra, presented in the right panels, clearly show this effect. The blue-shifted resonance shown in the bottom right panel is a CTP where the junction field essentially has disappeared and the plasmon induced charges reside on the opposite ends of the dimer just as for the dipolar plasmon of an individual nanorod.

The above-mentioned effects are not restricted to spherical nanoparticles. In a recent experiment by Slaughter et al.,[177] the optical properties of touching nanorods were investigated. The left panel in Figure 11C shows the measured spectra for two different touching nanorod dimers. For these particular systems, the conductive overlap is relatively weak, resulting in a CTP that is strongly red-shifted compared with the nontouching nanorod dimer plasmon. The extreme sensitivity of the energy of the CTP to separation is shown in the right panels of Figure 11C.

Recently a novel approach for studying the optical properties of touching nanoparticles based on transformation optics has been developed.[178−181] This approach is based on the invariance of Maxwell's equations under conformal coordinate transformations. With use of a suitable conformal transformation, a composite finite interacting nanostructure can be mapped into simpler interacting extended structures where analytical solutions are available. This classical approach can provide a rigorous analytical description of the optical properties of touching metallic nanoparticles. Some examples of this approach are given in Figure 11D, showing the electric field enhancements for a nanocrescent and a nanoparticle dimer.[180] Although this approach neglects QM effects, it holds significant promise for the analytical calculation of optical properties and EM field enhancements in dimer junctions of complex geometries.

Clearly the major deficiency of the classical approaches is the assumption of an infinitely sharp surface of the nanoparticles. This deficiency can be addressed by modeling the nanoparticles using more realistic nonlocal dielectric functions.

3.2. Incorporation of Nonlocal Dielectric Functions

In the conventional classical EM modeling of the optical properties of nanostructures, such as finite-difference time-domain (FDTD), finite element method (FEM), boundary element method (BEM), or discrete dipole approximation (DDA) (for a detailed discussion of their implementation and merits, see, for example, ref 182), the materials enter Maxwell's equations through the frequency-dependent dielectric permittivity, $\varepsilon(\omega)$. This quantity is assumed to be constant within the material, then to abruptly change to the value of the background medium at the interfaces of the nanostructure. For instance, for a gold sphere of radius R in vacuum, the dielectric permittivity is modeled as

$$\varepsilon(\omega, \vec{r}) = 1 + \Theta(R - r)\varepsilon_{\mathrm{Au}}(\omega) \qquad (2)$$

where $\Theta(x) = 0$ for $x < 0$ and $\Theta(x) = 1$ for $x > 0$ and r is the distance to the center of the sphere. In some sense, the dielectric function is thus spatially dependent, that is, nonlocal, but this simple form does not properly account for the true spatial dependence and nonlocality of the dielectric function of a realistic material. To understand this, it is instructive to consider the definition of the dielectric function, which relates the displacement field $\vec{D}$ to the electric field $\vec{E}$. For an arbitrary finite nanoparticle, this relation takes the form

$$\vec{\mathrm{D}}(\vec{r}, t) = \int_{-\infty}^{t} \mathrm{d}t' \int_{V} \mathrm{d}V'\, \varepsilon(t - t', \vec{r}, \vec{r}')\, \vec{\mathrm{E}}(t', \vec{r}') \qquad (3)$$

This general expression relates the induced displacement field at a position $\vec{r}$ to the electric field at $\vec{r}'$. The dielectric permittivity $\varepsilon(t - t', \vec{r}, \vec{r}')$ is nonlocal in a double sense since it explicitly depends both on $\vec{r}$ and $\vec{r}'$.

For an infinite translationally invariant homogeneous material the spatial dependence of the dielectric permittivity becomes much simpler: $\varepsilon(t - t', \vec{r}, \vec{r}') = \varepsilon(t - t', \vec{r} - \vec{r}')$. While the dielectric function for this system is still nonlocal (dependent on the separation between $\vec{r}$ and $\vec{r}'$), the assumption of translational invariance introduces a considerable simplification in eq 3, which can be written

$$\vec{\mathrm{D}}(\vec{r}, t) = \int_{-\infty}^{t} \mathrm{d}t' \int_{V} \mathrm{d}V'\, \varepsilon(t - t', r - r')E(t', r') \qquad (4)$$

In the harmonic approximation and using a plane wave basis, this equation can now be written compactly as $\vec{D}(\omega, \vec{k}) = \varepsilon(\omega, \vec{k})\vec{E}(\omega, \vec{k})$. Simply put, the dielectric response of an infinite homogeneous material depends on the shape (wavevector $\vec{k}$) of the electric field.

As described above, in typical EM applications, one also neglects this $\vec{k}$ dependence and models the nanoparticle using the simple local expression given in eq 2. This is clearly a rudimentary approximation and amounts to a neglect of many important screening effects, such as the presence of evanescent electrons outside the surfaces of nanostructures and the intrinsically nonlocal screening properties of any bulk metal. The former effect is particularly important for points around the surfaces of the nanoparticles. Despite these complications, phenomenological corrections for nonlocality can be achieved by inclusion of an empirical $\vec{k}$ dependence in the dielectric function. These applications typically focus on the nonlocality introduced by the $\vec{k}$-dependent dielectric function for a bulk material and neglect the significantly more complicated case of nonlocality introduced by the surface.

The importance of including nonlocal effects in the description of the optical response of metallic nanoparticles was recognized some time ago.[147] Since then, many types of nonlocal dielectric functions for bulk materials have been derived. In Figure 12A, we show the results from a nonlocal modeling of the dielectric function for gold in a gold nanosphere dimer.[183] This calculation uses the full dielectric function derived by Mermin for bulk gold. The figure clearly shows that the spectrum is strongly affected by nonlocal effects. In particular for small separation, the nonlocal calculation predicts a weaker red shift of the BDP. Figure 12B shows the results for 2D gold nanoshells using a nonlocal $\vec{k}$-dependent dielectric function derived from a hydrodynamic description of the electron gas.[184] In this application, novel peaks appear in the spectra. Figure 12C shows an application to the plasmon resonances of a metallic nanowire using the nonlocal plasmon pole approximation.[185] In this application, nonlocal effects are found to increase the energy of the plasmon resonances. Figure 12D shows a comparison of the optical spectra for a small silver nanoshell calculated using two different nonlocal descriptions of bulk silver, the hydrodynamic model and the Lindhardt−Mermin dielectric model.[186]

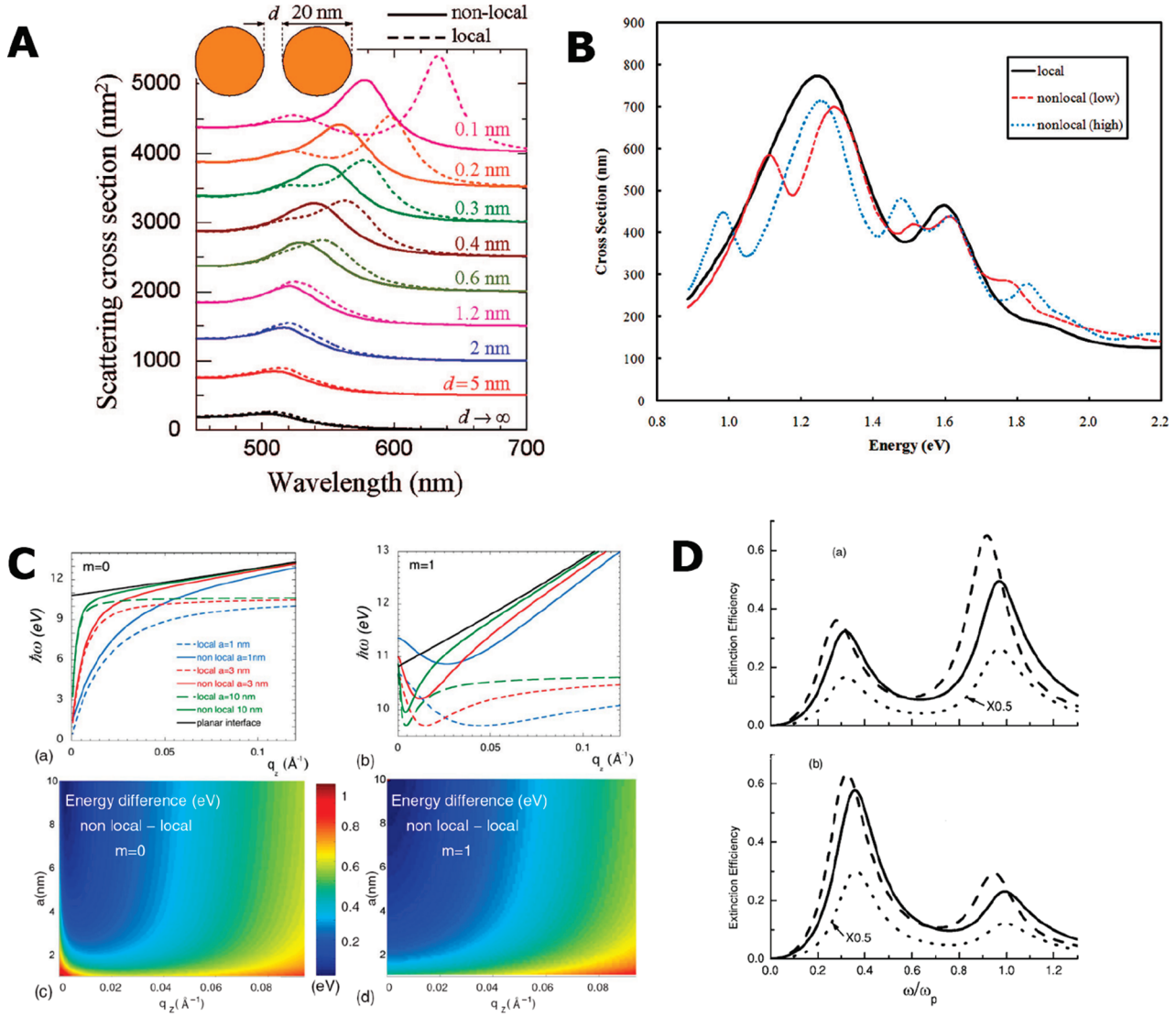

Figure 12. Different approaches for inclusion of nonlocal dielectric screening in classical EM simulations: (A) Gold sphere dimer for different gaps.[183] (B) Optical response of gold nanoshell.[184] (C) Silver nanowire plasmon dispersion for $m = 0$ (top left) and $m = 1$ (top right) and the corresponding energy difference between nonlocal and local calculation for different wavevectors.[185] (D) Silver nanoshell with a glass core (top) and with a vacuum core (bottom).[186] Reprinted with kind permission from refs 183−186. Copyright 2008 American Chemical Society (ref 183), Copyright 2010 American Chemical Society (ref 184), Copyright 2008 American Physical Society (ref 185), and Copyright 2006 American Physical Society (ref 186).

For this system, the effect of nonlocality is a blue shift of the plasmon resonances.

From the above discussion, it is clear that the proper inclusion of nonlocal screening effects is a difficult and somewhat ambiguous endeavor. For a proper investigation of nonlocal effects, it is necessary to perform fully QM calculations of the nonlocal dielectric functions, including both the $\vec{k}$-dependence present even for infinite bulk systems and the nonlocality introduced by the surfaces. Such quantum models provide the right results from which the validity of nonlocal classical approaches can be assessed. In the next two sections, we will review several such fully QM approaches for *ab initio* calculations of the optical properties of nanoparticles.

3.3. Quantum Plasmonics: Individual Nanostructures

The fully QM calculation of the optical properties of metallic nanoparticles represents a formidable and unsolvable problem.[187,188] The most convenient approach for such calculations is the time-dependent density functional theory (TDDFT).[189] This approach was used early on to model the electronic and optical properties of small nanoparticle clusters.[190−193] For free-electron-like metals such as noble metals, the optical response is determined by plasmons, that is, by the conduction electrons. The essential features of the dynamics of the conduction electron liquid are well described by a jellium model, where the confining potential from the positive ionic background is replaced by a constant box potential. If the parameters of this box potential are chosen so that the nanoparticle has the correct work function, the resulting electron density profile is similar to the electron density of a real metal. The jellium model has been very successful and has been used extensively in a wide range of calculations of the chemical, physical, and optical properties of metals.[194−197] The jellium model is defined by the conduction electron density parameter, r_S, which is the radius of a sphere of the material containing one electron, and the background polarizability,

dx.doi.org/10.1021/cr200061k |*Chem. Rev.* 2011, 111, 3913–3961

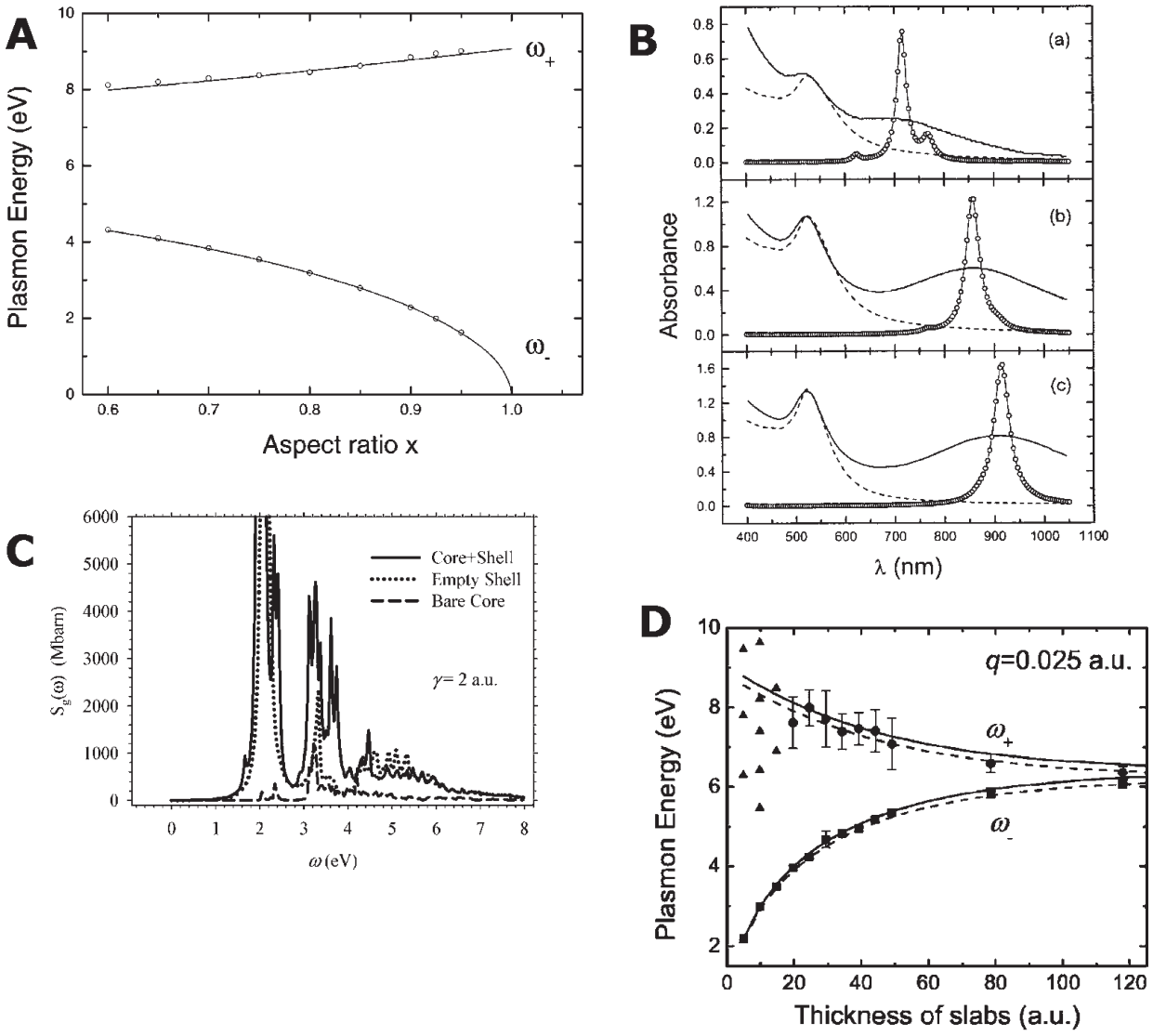

Figure 13. Fully quantum mechanical calculations of the absorption spectra of individual nanostructures. (A) Comparison of bonding and antibonding nanoshell plasmon resonances as a function of nanoshell aspect ratio calculated using TDDFT and classical Mie theory.[200] (B) Comparison of TDDFT spectra and experimentally measured extinction spectra for gold nanoshell with gold sulfide core.[203] (C) Effect of the dielectric core on the TDDFT spectrum for small nanoshells.[204] (D) TDDFT calculations of the energies of bonding and antibonding film plasmon resonances as function of film thickness. Solid lines are the results from classical EM modeling.[55] Reprinted with kind permission from refs 200, 203, 204, and 55. Copyright 2003 American Chemical Society (refs 200 and 203), Copyright 2004 American Chemical Society (ref 204), and Copyright 2006 American Physical Society (ref 55).

ε_J (sometimes also denoted ε_∞ or ε_B) of the lattice, which is the effective polarizability of the ions.

The theoretical procedure in TDDFT involves first performing a self-consistent calculation of the electronic structure of the system. In this step, the positive background representing the metallic lattice of the nanostructure is represented by a pseudopotential with parameters that are chosen so that the work function and electron density in the interior of the nanostructure correspond to the experimentally measured values. The electron−electron interactions are accounted for by an exchange correlation potential, which depends on the local electron density. From the self-consistent equilibrium electronic structure (wave functions and their energies), one then calculates the independent electron response function, χ^0 (Lindhardt susceptibility). With linear response theory and the random phase approximation (RPA), the interacting response function, χ, can then be calculated from an integral equation. The dielectric function, ε^{RPA}, can then be directly obtained from χ.[189]

Even though TDDFT represents a considerable simplification of the problem, such calculations are extremely time-consuming and require the use of supercomputers.[198,199] Their computational complexity scales as the cube of the number of electrons in the system. While the original calculations in the 1980s for small metallic clusters were limited to less than 100 electrons, modern parallel computers can handle up to several million electrons in systems with a high degree of symmetry such as spheres.

Plasmons are collective modes and can be expressed as coherent superpositions of electron−hole pair excitations. For a small nanoparticle, the plasmon mode is not fully formed and the optical response is best described in molecular terms. As the particle becomes larger, the energy difference between the electronic levels in the nanoparticle decreases and the collective

plasmon mode appears. Although a plasmon-like mode in a spherical nanoparticle can appear already for 50 electrons, its energy and properties exhibit quantum confinement effects until the metallic sphere is sufficiently large to contain nominally 500 electrons.

The first tunable plasmonic nanoparticle that was investigated using TDDFT was the metallic nanoshell.[200−203] This system possesses spherical symmetry, and self-consistent field calculations can be performed for nanoparticles containing up to a million electrons.[200] In Figure 13A, we compare the results from TDDFT and Mie theory for the bonding and antibonding nanoshell plasmon modes as a function of nanoshell aspect ratio (inner radius/outer radius) for a free electron metal with $r_S = 3$ and $\varepsilon_J = 1$.[200] The figure demonstrates a remarkable agreement between classical and QM calculations for the plasmon energies. In Figure 13B, the calculated and measured spectra for small gold sulfide core/gold shell nanoparticles of different aspect ratios are compared.[203] For the smallest nanoshell, the plasmon resonance overlaps electron−hole pair excitations and is therefore split into a double resonance. In the bottom panel showing the spectrum for a nanoshell of inner diameter 26 nm and outer diameter of 30 nm consisting of around 2 million electrons, the density of states is bulk-like and the plasmon resonance has a clear Lorentzian line shape.[203] The results demonstrate excellent agreement between TDDFT and the measured spectra. The experimental measurements were for an ensemble of nanoshells of slightly different aspect ratios. More detailed theoretical calculations taking into account the nanoshell size dispersion result in similar linewidths. In Figure 13C, results from the time-domain TDDFT calculations of the effect of the dielectric core on the optical absorption of small nanoshells are depicted.[204] The results agree with the frequency-domain calculations presented by Prodan et al.[200,203] In Figure 13D, the TDDFT method was applied to the plasmon resonances of a thin metallic film.[55] As for the metallic nanoshell, for a given wave vector, there are two hybridized film plasmons, a bonding mode with symmetrically aligned surface charge densities and an antibonding mode with antisymmetric alignment.[75] The results from the QM TDDFT calculations are found to be in excellent agreement with the results from classical models. However, for the width of the film plasmons, quantum effects are significant and cannot be modeled using classical theory.

Figure 14 shows applications of TDDFT to nanorod structures. Figure 14A shows the absorption spectrum of atomically thin metallic Na wires of various lengths. The spectrum displays a strong red shift of the wire plasmons with increasing length.[205] Such a red shift is characteristic of the nanorod geometry where the longitudinal resonance is known to red shift with increasing length/diameter ratio. In Figure 14B, the absorption spectra of small silver nanorods calculated using an atomistic description of the silver atoms are illustrated. Although these clusters are too small to exhibit a pure plasmon resonance, the calculation shows a red shift of the absorption peak with increasing aspect ratio of the nanorod as expected from classical electrodynamics simulations.[206] In Figure 14C, the absorption spectra for silver nanorods modeled using a jellium description for different polarizations and aspect ratios are shown.[207] With increasing aspect ratio, the longitudinal and transverse plasmons red shift and blue shift, respectively, in almost perfect agreement with classical EM simulations.

In the applications discussed so far, it was found that the energies of the plasmon resonances obtained using TDDFT were very similar to the energies obtained using simple classical EM modeling. However, the widths of the resonances can be very different, in particular when quantum size effects are present for very small systems. Another important property of plasmonic nanoparticles is the plasmon-induced EM field enhancements. This subject has already been discussed in the context of SERS. Figure 14D shows a comparison of the field enhancements calculated using TDDFT and classical EM theory.[207] These results demonstrate that the classical calculations drastically overestimate the field enhancements near (0.5 nm) the nanoparticle surfaces. This is not surprising, since a real nanoparticle will have a spill-out electron density in the surface region, which will effectively screen the local electric fields. Another contributing factor is the nonlocal aspect of the screening due to the surface electrons. In a classical model, the surface charges reside in an infinitely thin region at the interface, while in a realistic calculation, the screening charges are smeared out over a finite region around the surface. The finding of strong nonlocal QM induced screening near the surface of a nanoparticle means that field enhancements obtained from classical EM calculations cannot be trusted within a region of 0.5 nm around the surfaces of the nanoparticles.

We now turn to the case of quantum effects in strongly coupled plasmonic nanoparticles with narrow gaps.

3.4. Quantum Plasmonics: Coupled Nanoparticles with Narrow Gaps

The theoretical implementation of TDDFT for nanoparticle dimers is considerably more difficult than the application to nanoparticles with spherical symmetry.[208,209] But because of the significance of strongly coupled metallic nanoparticle dimers in SES applications, this is an important system to investigate. In Figure 15A, the TDDFT optical properties of linear chains of Na atoms are shown for both longitudinal and transverse polarization.[210] This calculation is performed using an atomistic description of the Na atoms. Although the system has very few electrons (up to 18 for the longest chain), the spectra exhibit plasmon-like excitations. As for a nanorod, the longitudinal excitation red shifts with increasing chain length, while the transverse excitation exhibits a weak blue shift.

Figure 15B shows TDDFT calculations of the absorption spectra and plasmon-induced EM field enhancements of a strongly coupled nanoparticle dimer modeled using a jellium description with $r_S = 3$ and $\varepsilon_J = 1$ for different dimer separations.[211] The calculated spectra reveal a BDP resonance that red shifts with decreasing dimer separation. For intermediate separations, a hybridized BQP mode appears with an intensity that increases with decreasing dimer separation. For dimer separations shorter than around 1 nm, the red shift of the BDP saturates and begins to blue shift with decreasing separation. This crossover from red-shifting to blue-shifting is because of the reduced coupling between the plasmons on the different nanoparticles due to electron tunneling between the particles. For the smallest dimer separations, the conductive overlap between particles is sufficiently strong that a higher order CTP is enabled. The QM calculated optical spectra are in sharp contrast to the results from classical calculations shown in Figure 11A,B, which exhibit a discontinuous jump between the touching and non-touching regimes. It is interesting to note that because of the conductive overlap and the onset of the CTP, the spectra obtained using QM are different from the spectra obtained using classical EM. This finding is different from the optical spectra of

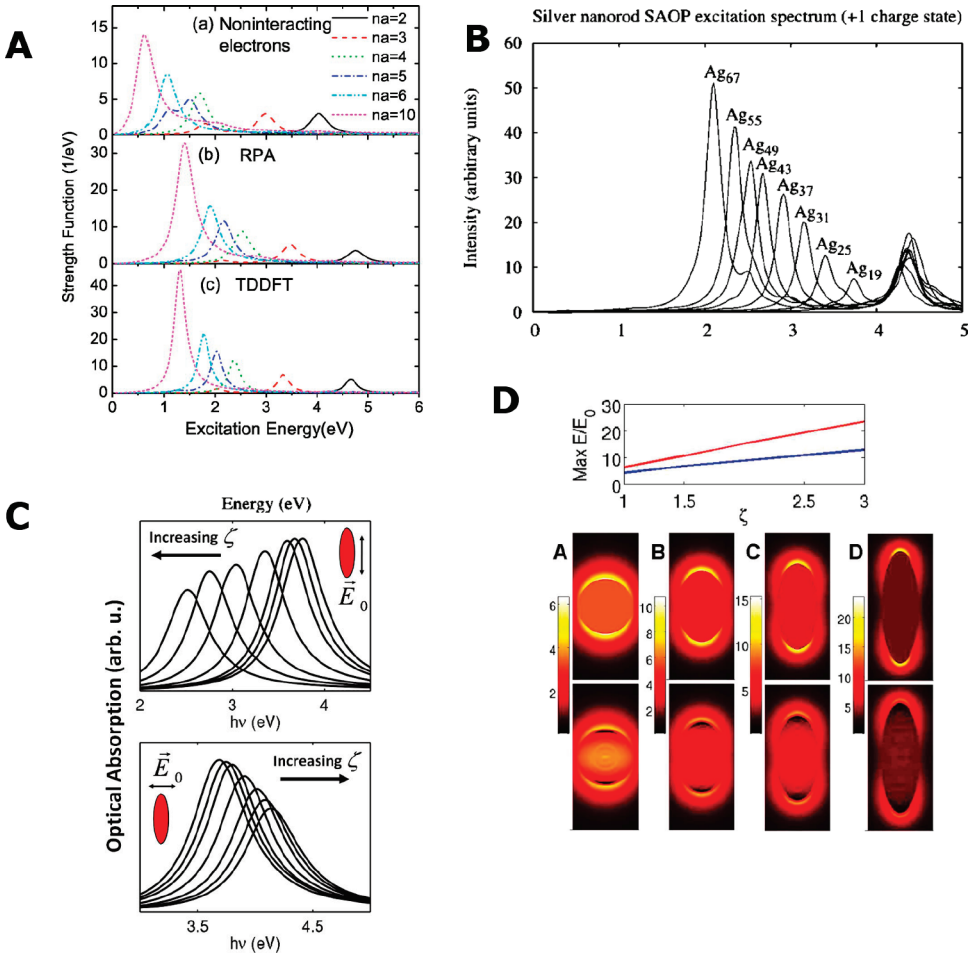

Figure 14. TDDFT calculation of the optical properties of nanorod structures. (A) Optical properties of atomically thin Na wires of different lengths using different response functions.[205] (B) TDDFT spectra for small silver nanorod clusters calculated using an atomistic description of the silver atoms.[206] (C) TDDFT calculations of the optical spectra of silver nanorods for different aspect ratios and polarization.[207] (D) (top) Comparison of the field enhancements for silver nanorod calculated using classical EM (red) and TDDFT (blue); (middle) the classical EM results and (bottom) the TDDFT results for different nanorod aspect ratios.[207] Reprinted with kind permission from refs 205−207. Copyright 2005 American Physical Society (ref 205), Copyright 2009 American Chemical Society (ref 206), and Copyright 2010 American Chemical Society (ref 207).

individual nanoparticles described in section 3.3 where the plasmon resonances obtained using QM and classical EM agreed very well. Also, the field enhancements in the nanoparticle junctions exhibit strong QM effects. In the right panel of Figure 15B, the field enhancements obtained from TDDFT and classical EM are compared. For dimer separations smaller than 1 nm, the classical calculations drastically overestimate the EM field enhancements.

Figure 15C shows the results of a TDDFT calculation of the instantaneous potential energy difference in a strongly coupled silver nanoplate dimer, following a step-like laser excitation.[212] The calculation reveals damped oscillations with a decay rate that strongly depends on the separation between the two nanoplates. This decay rate is directly related to the tunneling probability between the two structures and shows that electron tunneling begins to play an important role for separations below 1 nm, in agreement with the results shown in Figure 15B. In Figure 15D, the results from a TDDFT calculation of the potential difference between two metallic nanoparticles with a sodium atom placed in the center of the dimer are shown as a function of dimer separation.[213] The top panel shows the current amplitude as a function of the frequency of the incident light. Two resonances are clearly visible, a lower energy resonance around 1 eV corresponding to a CTP and a stronger resonance around 4 eV corresponding to the excitation of the BDP. The middle panel shows that the voltage across the junction is largest for the excitation of the BDP. With decreasing dimer separation, this voltage is reduced due to the short-circuiting of the junction caused by electron tunneling across the gap. The lower panel of Figure 15D shows the conductance of the junction. The increased conductance at the CTP energy is due to tunneling through the Na 3s state and will be discussed further in the next subsection.

The finding of strong QM effects in narrow plasmonic gaps offers some novel interesting applications. While much work has been focused on optimizing dimer geometries for large electric field enhancements and the resulting giant enhancement of SERS signals, another application may be to use the strongly plasmon induced electron currents in a narrow nanoparticle junction to study electronic excitations of molecules present in the gap.[214−222] It is quite possible that such current-induced molecular excitations may show up as satellite peaks and/or result in shifted or broadened absorption spectra. This phenomenon could quite

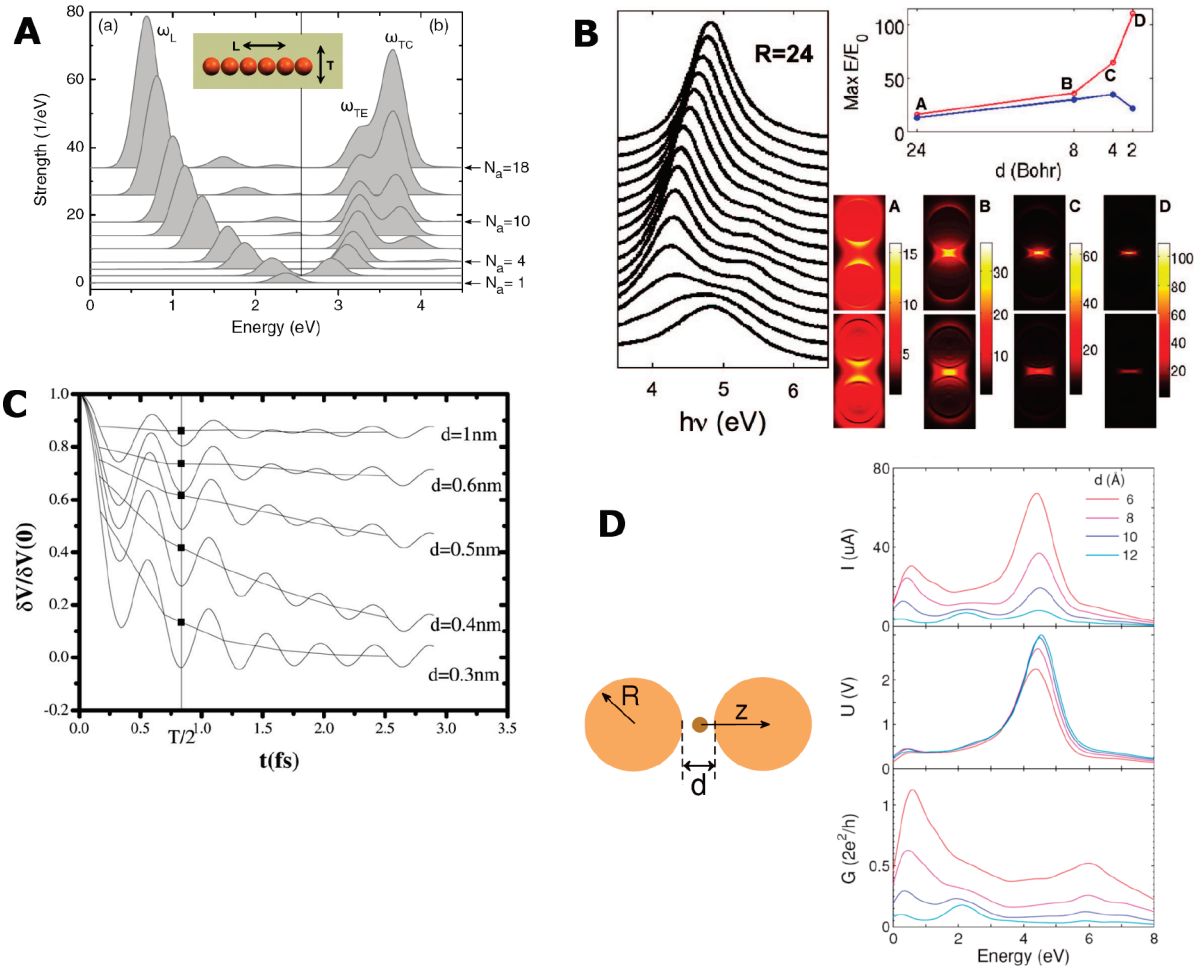

Figure 15. TDDFT calculation of the optical properties of strongly coupled nanoparticles. (A) Optical spectra for Na atom chains of different lengths and polarizations.[210] (B) Optical spectra for a nanoparticle dimer for different separations (left). The top right panel shows a comparison of the maximum field enhancements in the junction calculated using TDDFT (blue) and classical EM (red). The right middle panel shows the field enhancements calculated using classical EM, and the bottom panel is the result from TDDFT.[211] (C) Instantaneous voltage difference across the gap in a silver nanoplate dimer following a step-like excitation.[212] (D) Tunneling current (top), gap voltage (middle), and tunneling conductance (bottom) of a Na atom in a nanoparticle dimer as a function of the frequency of the incident light.[213] Reprinted with kind permission from refs 210−213. Copyright 2007 American Physical Society (ref 210), Copyright 2009 American Chemical Society (ref 211), and Copyright 2009 (ref 212) and Copyright 2011 (ref 213) American Institute of Physics.

possibly open up a new approach for molecular spectroscopy and molecular sensing and is likely to be explored in the future.

3.5. Effect of Conductive Junctions for Strongly Coupled Nanoparticle Dimers

Here we present a qualitative discussion of how a conductive bridge across a nanoparticle dimer junction will influence the optical properties of the dimer. Such a conductive bridge could consist of either conducting molecules or nanowires or the same material as the nanoparticles.[223,224] Figure 16A shows a classical EM investigation of how the conductance of a cylindrical conductive junction in a nanoparticle dimer gap influences the optical spectrum.[175] As the conductance is increased, the BDP around 800 nm begins to blue shift until it saturates at a value that corresponds to a screened BDP (SBDP). The SBDP is a capacitively coupled dimer plasmon where the surface charges on the opposite ends of the conductive junction have been short circuited by charge transport through the junction. The energy difference between the BDP and the SBDP thus depends on the area of the junction. Also the width of the BDP peak is changing although this is difficult to see on the large wavelength scale of the figure. For large conductance, a CTP appears prominently around a wavelength of 3000 nm, with an intensity that increases strongly with the conductance. The physical reason for the blue shift of the BDP is the neutralization of the plasmon induced surface charges on the nanoparticle−junction interfaces, as illustrated in the top part of the figure, which shows the field enhancements in the junction for the different modes. Simply put, an electron current short-circuits part of the junction and thus reduces the capacitive coupling between the two nanoparticles. The Ohmic dissipation associated with the charge transport across the junction is also responsible for the change in the line width of the BDP. For the CTP, there is significantly more charge transfer. The narrowing of the CTP with increasing junction conductance is due to reduced Ohmic dissipation in the junction. The electric field contour plot for the CTP at 3000 nm in the upper panel of Figure 16A shows that also the electric field enhancements outside the conductive bridge have

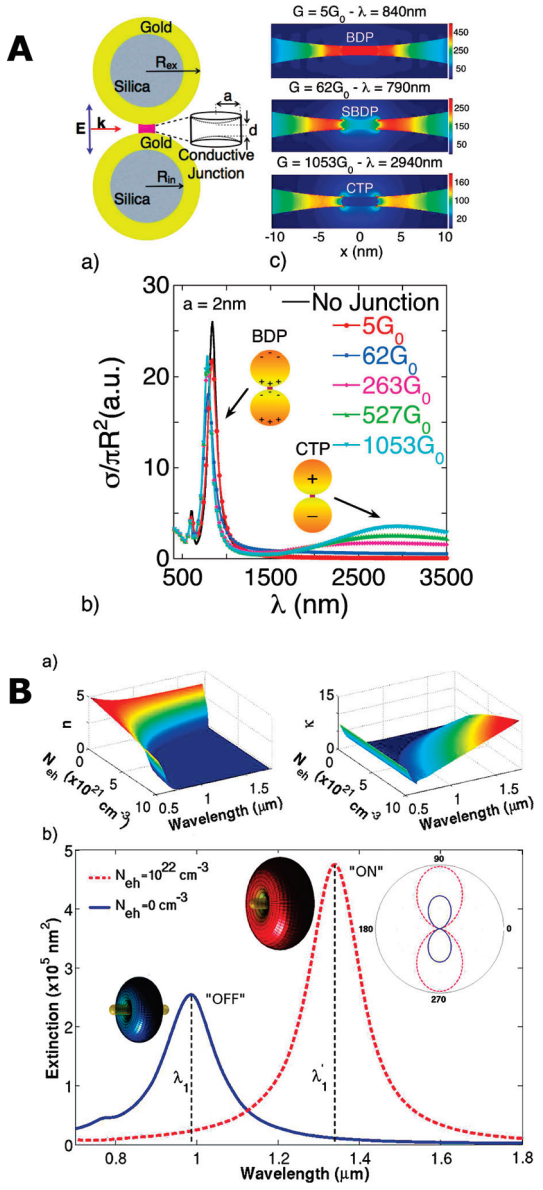

Figure 16. (A) Effect of conductive junctions on the plasmonic properties of nanoparticle dimers. (a) A nanoshell dimer with a conductive bridge linking the two nanoshells.[175] (c) The contour plots show the electric field enhancements associated with the BDP, SBDP, and CTP. (b) The extinction spectra for different junction conductances. (B) (a) Effect of free carrier density on the real and imaginary refractive index of amorphous silicon.[226] (b) Extinction spectra of a gold nanorod dimer linked by amorphous silicon for carrier density zero and for 10^{22} cm^{-3}. Reprinted with kind permission from refs 175 and 226. Copyright 2010 American Chemical Society.

been reduced. For the CTP, the electric current across the junction is much larger than for the BDP resulting in a significant reduction of the EM field enhancements in the gap.

The energies of both the BDP and CTP modes depend strongly on the conductance and geometry of the junction. Thus by measuring the optical spectrum, it is possible to deduce the conductance of the conductive bridge at the BDP and CTP frequencies. By changing the geometry of the dimer and thereby tuning the energies of its plasmon modes, it may be possible to measure such molecular conductance over extended wavelength regimes. Such an all-optical approach for measuring molecular conductance may be of importance for the field of molecular electronics where the conventional electrical conductance measurements have thus far been constrained to DC frequencies.

The possibility to control the optical properties of a plasmonic system using conductive linkers offers novel and interesting approaches for ultrafast optical switching devices.[225] Large et al. noted that the dielectric permittivity of amorphous silicon depends strongly on the free carrier density, which can be controlled using photoexcitation.[226] The top panel of Figure 16B shows the real and imaginary parts of the refractive index of amorphous silicon as a function of the free carrier density. For sufficiently large carrier density, amorphous silicon becomes a conductor. Thus by filling the cavity between two nanorods and controlling the free carrier density of the material, it is possible to switch the plasmonic response from a BDP to a CTP. The spectra shown in the lower panel of Figure 16B show that the effect can be very significant. In the "off" state (no free carriers), the plasmon mode is located around 1000 nm, but for the "on" state, the plasmon mode appears at 1350 nm. Further generalizations of this concept using other types of photoconductive materials hold much promise for fabrication of active plasmonic devices.[227,228]

3.6. Coupling between Plasmonic and Excitonic Systems

An emerging topic in plasmonics is the study of the interaction of plasmonic and excitonic systems. Although the proper description of this phenomenon would require a quantum mechanical approach, the qualitative aspects of this interaction can be modeled using classical EM methods. When a quantum dot or quantum emitter is placed near a plasmonic nanoparticle, the EM interaction between the exciton and plasmon can result in hybridized states, consisting of bonding and antibonding mixed states.[229−231] The wave functions of these hybrid states are mixtures of the collective plasmon mode and the exciton and are sometimes referred to as plexcitons,[229] to highlight their mixed plasmonic/excitonic character. There are many applications of such plexcitonic systems. For instance, by exciting excitons in quantum dots near a plasmonic structure, it is possible to compensate for plasmon decay and achieve gain, a property that has recently resulted in the experimental realization of plasmonic lasers.[232] The strong coupling between excitons and plasmons can also be exploited to study energy transfer through a plasmonic structure between two quantum dots.[233−235] The strong local electromagnetic field enhancements induced near a plasmonic nanostructure can be used in energy applications such as upconversion of light,[236,237] to enhance the excitation of carriers in nearby molecules or materials,[238−240] and even to enhance chemical reactions.[241] In several recent studies, it has been shown that the radiative lifetime of a exciton can also be modified by the interaction with a plasmon through the Purcell effect.[242−244] The coupling between quantum dots and plasmonic systems can also be exploited to image the local field distribution on the surface of a plasmonic nanostructure. The excitation of a nearby quantum dot is proportional to the local electric field intensity, and the intensity of the luminescence is thus a monitor of the plasmon-induced near field.[245−247]

4. EXTENDED STRUCTURES

As already discussed for small nanoparticle assemblies such as dimers, trimers, and oligomers, the type and strength of plasmon

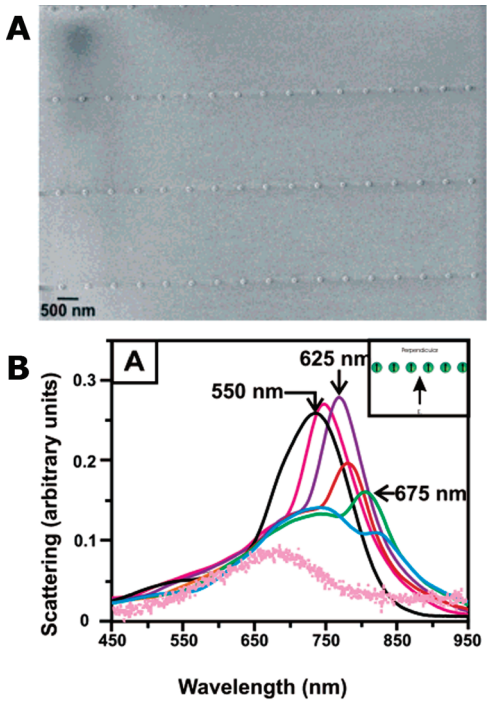

Figure 17. (A) SEM image of an array of silver nanoparticle chains with interparticle separation of 632 nm. The line spacing was 2 μm to avoid interactions between nanoparticle chains. The diameter and height of the nanoparticles were 130 and 30 nm, respectively. (B) Ensemble scattering spectra of nanoparticle chain arrays. The interparticle distance was varied between 400 and 700 nm. The nanoparticles were embedded in a medium with a uniform refractive index of 1.5. The excitation polarization and wave vector were perpendicular to the chain axis as shown in the inset. The single particle spectrum is given by the dotted line and has a peak wavelength of 660 nm. For interparticle distances close to the single nanoparticle resonance wavelength, diffractive coupling leads to a spectral narrowing of the collective plasmon response of the nanoparticle chain.[250] Reprinted with kind permission from ref 250. Copyright 2005 American Chemical Society.

coupling in extended nanoparticle structures also depends most critically on the nanoparticle separation. In arrays with interparticle distances d on the order of the wavelength of the light and comparable to the isolated nanoparticle resonance, far-field diffractive coupling dominates, with a d^{-1} distance dependence. As the interparticle distance decreases to dimensions comparable to the nanoparticle size, near-field interactions take over and follow a d^{-3} distance dependence. Both far- and near-field plasmon coupling in extended structures lead to a variety of new effects, such as narrow linewidths ideal for surface plasmon sensing or energy transport along a nanoparticle chain acting as a plasmonic waveguide with subwavelength dimensions. This section will give an overview of these and other phenomena observed for extended structures that were fabricated by several different methods.

4.1. Plasmon Coupling in Periodic 1D and 2D Nanoparticle Arrays

Most of the quantitative studies on plasmon coupling have come from nanoparticle arrays that were made by top-down fabrication.[248−258] The ability to produce arrays with homogeneous nanoparticle sizes and shapes as well as regular interparticle separations using lithography techniques has provided invaluable

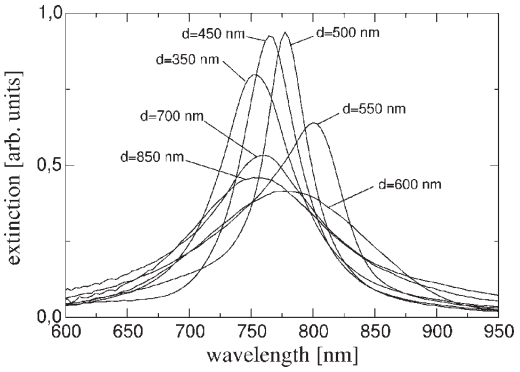

Figure 18. Extinction spectra of two-dimensional gratings of gold nanoparticles. The diameter and height of the nanoparticles were 150 and 14 nm, respectively. The grating constant d varied from 350 to 850 nm. Radiative plasmon coupling leads to a spectral narrowing as a function of grating constant.[252] Reprinted with kind permission from ref 252. Copyright 2000 American Physical Society.

insight into the far- and near-field interactions of surface plasmons in periodic metal nanoparticle structures.[248,249,252,255,257,259−262] Electron-beam lithography has the advantage of producing arrays of nanoparticles that all have the same size, shape, and interparticle distance, allowing quantitative measurements to be carried out even with ensemble techniques. More recently, nanoparticle arrays have also been fabricated by laser printing[263,264] and nanoimprinting techniques.[265] These methods allow one to precisely pattern chemically synthesized nanoparticles using top-down approaches.

In nanoparticle arrays with the interparticle distance comparable to the surface plasmon resonance wavelength of the isolated nanoparticle, far-field interference causes a narrowing of the plasmon mode.[249,250,252] Hicks et al. investigated the line shape of collective plasmon modes in linear arrays of silver nanoparticles with a diameter or 130 nm and a height of 30 nm.[250] For the chains shown in Figure 17A, they observed that the scattering spectra (Figure 17B) contained several features including a long wavelength shoulder, which significantly gains in intensity and narrows spectrally for interparticle distances comparable to the resonance wavelength of an isolated nanoparticle. Lamprecht et al. reported a spectral narrowing for the extinction spectrum of 2D gratings, as shown in Figure 18.[252] The gratings consisted of gold nanoparticles with a diameter of 150 nm and a height of 14 nm. The narrowest lineshapes of the collective plasmon mode were found in a regime for the grating constant where radiative fields can strongly couple in phase for neighboring nanoparticles and evanescent fields are less important. Simulations using the coupled dipole approximation have shown that the width of the collective plasmon mode induced by far-field diffractive coupling can be smaller than 1 nm, which is important for applications such as surface plasmon resonance sensing since the sensitivity improves for narrower linewidths.[266]

Near-field coupling in linear nanoparticle chains has attracted considerable attention, mainly because the transverse and longitudinal modes supported by the chains are no longer localized on the individual nanoparticles but can propagate along the chain axis, allowing electromagnetic energy transport in waveguide structures smaller than the diffraction limit of the excitation light.[254,259,267−273] Coupling of light to propagating surface plasmons makes it possible to direct energy along a chain of

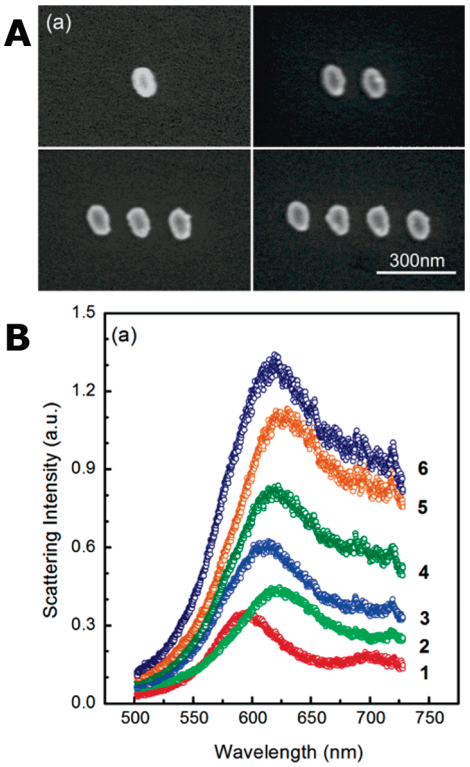

Figure 19. (A) SEM images of chains composed of one, two, three, and four gold nanoparticles. The length of the long and short axes of these elliptical nanoparticles were 102 and 74 nm, respectively. The thickness was 30 nm, and the center-to-center distance was 153 nm. (B) Scattering spectra of chains that contain an increasing number of nanoparticles. The red shift of the chain plasmon peak does not follow a monotonic trend due to phase retardation effects.[257] Reprinted with kind permission from ref 257. Copyright 2004 American Chemical Society.

nanoparticles.[267,274−277] Especially interesting are the characteristics of bending light around corners or splitting it into two or more branches with nanoparticle arrays that have other geometries, such as T-shaped structures.

For extended structures where near-field coupling between nearest neighbors dominates, increasing the number of nanoparticles from a dimer to a linear chain while keeping the interparticle distances constant leads to an increasingly red-shifted longitudinal plasmon resonance of the chain.[248,251,253−255,257,278] On the other hand, the transverse plasmon mode only slightly blue shifts, which leads to a pronounced splitting between the perpendicularly polarized transverse and longitudinal plasmon resonances. This energy splitting increases with the number of nanoparticles in the chain and can be viewed similarly to the corresponding plasmon resonances that emerge as a spherical nanoparticle is elongated to form a nanorod. However, both experiments and calculations have demonstrated that the plasmon shift saturates and the infinite chain limit is typically reached for chains consisting of about 10 nanoparticles because near-field interactions scale as d^{-3} and become negligible for larger separations.[253,268,279] Wei et al. have furthermore shown that phase retardation effects are important for chains of nanoparticles as the plasmon resonance peak wavelengths are red-shifted but do not follow a monotonic trend with increasing particle number as do chains of smaller nanoparticles.[257] Figure 19 shows SEM images (Figure 19A) of chains consisting of elliptical gold nanoparticles and optical scattering spectra (Figure 19B) illustrating this effect.

Surface plasmon propagation in nanoparticle chains has been analyzed by calculating the dispersion curves for infinite chains.[267,273,279−284] Within the quasi-static (dipole) approximation, the energy splitting between the transverse and longitudinal plasmon modes can be related to the plasmon propagation loss.[253,267] This theory predicts that the largest group velocity for a propagating surface plasmon with the smallest loss occurs for excitation at the plasmon resonance of an isolated nanoparticle. However, subsequent studies have shown that it is important to also include retardation and far-field coupling in simulations for chains of nanoparticles that have a finite size.[282,285] Compared with the quasi-static limit, more complex dispersion curves are obtained, which suggest larger bandwidths and greater group velocities. For example, Koenderink and Polman directly accounted for ohmic damping, radiation damping, and retardation in the calculation of the dispersion relation for infinite chains of 60 nm silver nanoparticles.[282] As shown in Figure 20, they found that retardation is responsible for the splitting of the dispersion relation for transverse modes into two anticrossing branches.

Because the theoretical studies mentioned thus far considered only dipole interactions, the results mainly apply to structures with interparticle distances comparable to the nanoparticle radius, prepared using electron-beam lithography.[267,273,279−283,285] Interestingly, Engheta et al. have investigated plasmon propagation in nanoparticle chains that were excited at the quadrupole plasmon resonance and found a larger bandwidth for the propagating surface plasmons.[286] In general, for decreasing nanoparticle separations, multipolar plasmon modes become increasingly important as studied theoretically by Park and Stroud who calculated dispersion relations using a generalized tight-binding approach.[284]

Finite chains of nanoparticles, which represent more realistic optical waveguides,[251,257,287,288] have also been analyzed theoretically.[269,279,285,289,290] For finite chains, nondegenerate coupled plasmon modes can be subradiant and therefore suffer smaller radiative losses compared with the super-radiant dipole mode.[277,291,292] Excitation at energies corresponding to subradiant modes therefore leads to longer propagation distances. In addition to subradiant modes, far-field radiative coupling must also be considered even at small interparticle distances.[248,251,255,293] For example, de Waele et al. have shown that phase retardation and interference in linear chains of 110 nm × 50 nm silver nanodisks with 150 nm center-to-center distances cause the localization of different wavelengths at opposite ends of the nanoparticle array.[248]

Although several theoretical studies have investigated plasmon propagation in nanoparticle chain waveguides and propagation lengths of several micrometers have been calculated,[259,267−269,271−273,294] only a few experimental realizations have been reported.[254,270] Maier et al. have observed energy transport in a linear chain of 90 nm × 30 nm silver nanorods with 50 nm gaps.[254] A SEM image and the corresponding extinction spectra of a chain and an isolated nanoparticle are shown in Figure 21A. Using a near-field scanning optical microscope to excite coupled transverse modes (Figure 21B), a plasmon propagation distance of 500 nm was determined by measuring the width of the intensity of fluorescent nanospheres that were placed close to the nanoparticle waveguide (Figure 21C). Another experimental study was carried out by Nomura et al., who have measured a plasmon propagation

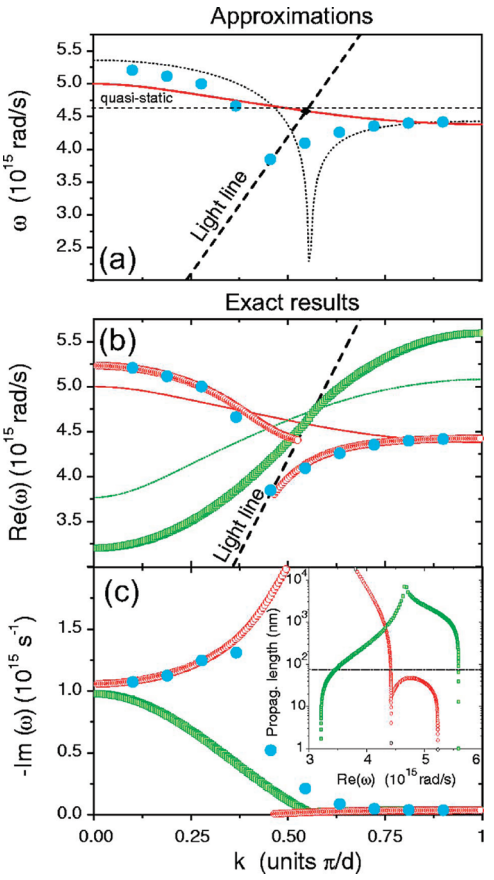

Figure 20. (a) Ten normal-mode frequencies for a chain of ten 30 nm silver nanoparticles (blue dots) are compared with the dispersion curves of an infinite chain obtained using quasi-static calculations (red curve) and a perturbative treatment (dotted curve), which both fail to describe the results for the finite chain. (b) Real part of the frequency for roots of the exact infinite chain dispersion for transverse (red open circles) and longitudinal (green open squares) plasmon modes. Two branches anticross at the light line (dashed line) for the transverse mode. The result agrees well with the finite chain dispersion (blue solid circles) but not with quasi-static calculations for the infinite chain (red thin curves). (c) Imaginary part of the frequency for the modes in panel b. The damping rate diverges near the light line for the transverse plasmon modes. The inset shows plasmon propagation lengths versus frequency for longitudinal (green open squares) and transverse (red open circles) plasmon modes with the horizontal line specifying the center-to-center distance of 75 nm.[282] Reprinted with kind permission from ref 282. Copyright 2006 American Physical Society.

length of 4 μm for a chain of 230 nm gold nanoparticles with gaps of 70 nm.[270] The main limitation for nanoparticle chain waveguides has been significant losses causing short propagation distances. Nanowires as discussed below have therefore emerged as a more promising building block for optical waveguides with subwavelength dimensions. However, losses might also be overcome in the future by amplifying surface plasmons using gain from surrounding excitonic media.[232,295−298]

4.2. Plasmon Coupling in Nanoparticle Assemblies

Chemical synthesis and bottom-up assembly of nanoparticles lead to complementary structural and optical properties compared with top-down fabrication methods. In particular, chemically synthesized nanoparticles are single crystalline and hence

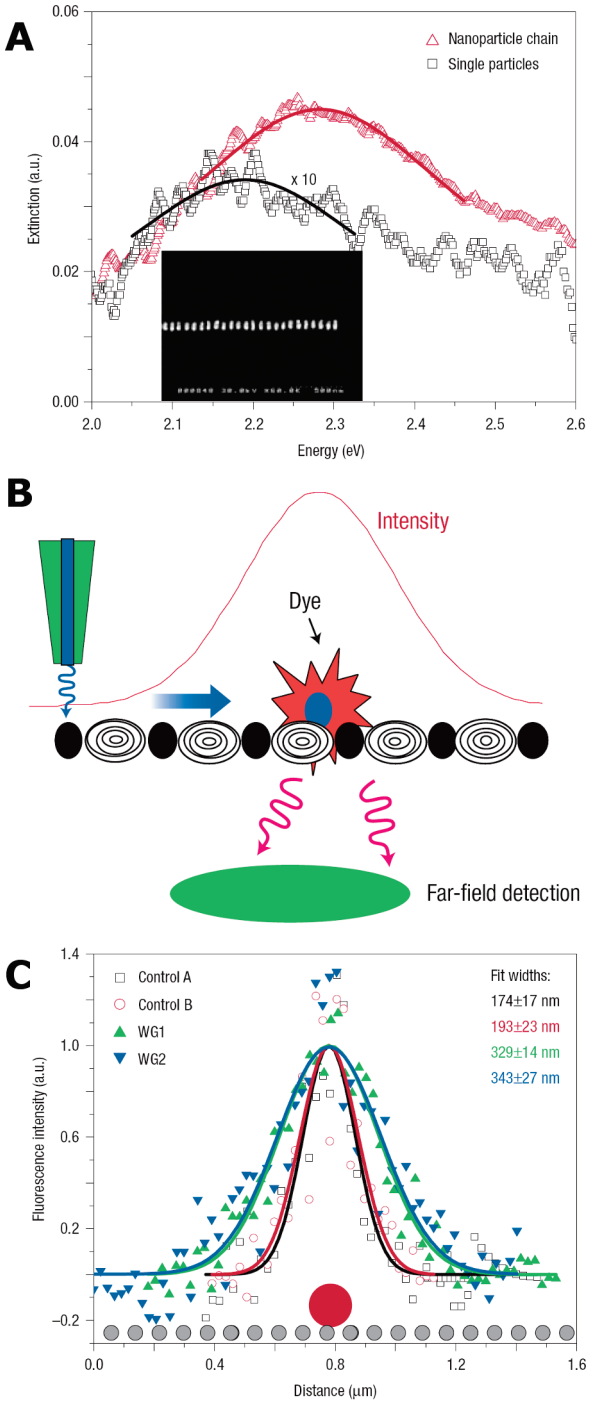

Figure 21. (A) Extinction spectra for nanoparticle chains and single nanoparticles. The dimension of the rod-like silver nanoparticles were 90 × 30 × 30 nm^3. The interparticle gap was 50 nm. (B) Experimental scheme used to measure the plasmon propagation length in nanoparticle chain waveguides. The tip of a near-field optical microscope locally excites a coupled transverse plasmon mode that propagates along the nanoparticle waveguide thereby transferring energy to a fluorescent nanosphere. The fluorescence intensity is then recorded by far-field optics as a function of tip position. (C) Fluorescence intensity line sections measured for nanospheres on top of the plasmonic waveguide and on the substrate as control. The broader width of the former is evidence of surface plasmon propagation along the nanoparticle chain.[254] Reprinted with kind permission from ref 254. Copyright 2003 Nature Publishing Group.

mostly free of internal scattering defects. In addition, the interparticle distance is only limited by the thickness of the surface capping material and can be varied by changing the size of surface bound molecules or polymers. Interparticle distances of a few nanometers are therefore easily achievable. However, distributions in nanoparticle size and shape are not as uniform as nanoparticles prepared by electron-beam lithography. Furthermore, interparticle distance and orientation are much harder to control in chemically prepared nanoparticle assemblies, making quantitative ensemble studies of plasmon coupling as a function of morphology more difficult. As discussed next, important applications have been developed based on plasmon coupling in colloidal extended structures, and the issue of sample heterogeneity can be overcome using single-particle spectroscopy methods.

It has been well recognized that colloidal gold nanospheres undergo a color change from red to blue when aggregation is induced in solution, as described in the Introduction to this review (Figure 1).[2] The reduced interparticle distances due to reversible aggregation enable efficient 3D plasmon coupling, which leads to a broadening and red shift of the plasmon resonance in accordance with the visible color change. This effect of 3D plasmon coupling in colloidal solutions has been developed for colorimetric sensors of biomolecular recognition events with DNA-functionalized gold nanoparticles.[9,299] However, quantitative correlations between the plasmon resonance shift and the size and shape of the aggregate are difficult to obtain for a broad distribution of aggregate morphologies in solution.

While reversible nanoparticle aggregation in solution allows one to build cost-effective and very sensitive sensors based on the strong plasmon extinction coefficients and near-field interactions, more quantitative correlations between the plasmon resonance shift and the interparticle distance have been gained from 2D nanoparticle assemblies.[125,300−303] Well-ordered and close-packed metal nanoparticle superlattices have been extensively studied and can be prepared by controlled evaporation of the solvent or in a Langmuir−Blodgett trough. The latter preparation method has the advantage that the interparticle distances can be controlled by varying the surface pressure in addition to the size of the capping material. For example, Collier et al. found a reversible insulator-to-metal transition for Langmuir monolayers of 4 nm silver nanoparticles when the interparticle distance was decreased to below 5 Å as evidenced by a metal-like reflectance and the disappearance of the plasmon resonance.[304] Chen et al. prepared hexagonal close-packed 2D superlattices of 11 nm gold nanoparticles and varied the interparticle distance between ~2 and 3.5 nm by changing the chain length of the alkanethiol capping material.[301] They observed a red shift in the plasmon resonance maximum with decreasing interparticle distance, which was argued to be in good agreement with results obtained for nanoparticle dimers. Chumanov and co-workers observed a distance-dependent narrowing of the plasmon resonance for a self-assembled 2D array of 100 nm silver nanoparticles, which they attributed to constructive interference due to coherent quadrupolar plasmon interactions similar to the far-field diffractive coupling in linear nanoparticle chains.[303] As the interparticle distance was increased by stretching of these arrays embedded in a polymer matrix, the plasmon resonance of the isolated nanoparticle was recovered.

Although the controlled assembly of nanoparticles into 1D chains is a much more challenging task compared with 2D structures, much attention has focused recently on nanoparticle

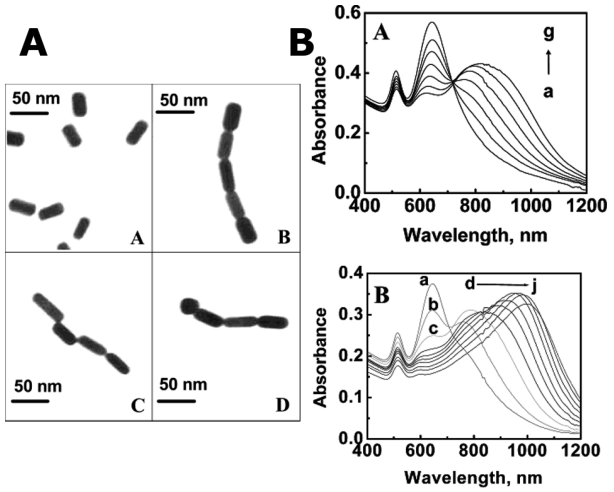

Figure 22. (A) TEM images of nanorods and nanorod assemblies linked by 3-mercaptopropionic acid. The average aspect ratio of the rods was 3. (B) (A) Extinction spectra of nanorods in solution (acetonitrile/water = 4:1) measured immediately after adding 3-mercaptopropionic acid at various concentrations: (a) 0, (b) 3.6, (c) 4.5, (d) 5.4, (e) 6.3, (f) 7.2, and (g) 8.1 mM. (B) Extinction spectra of nanorods in solution (acetonitrile/water = 4:1) recorded at different time intervals after adding 15 mM 3-mercaptopropionic acid: (a) 0, (b) 4, (c) 8, (d) 12, (e) 16, (f) 20, (g) 30, (h) 45, (i) 60, and (j) 120 min.[325] Reprinted with kind permission from ref 325. Copyright 2004 American Chemical Society.

chains, partially motivated by the demonstration of plasmonic waveguiding in linear nanoparticle arrays made by electron-beam lithography.[305] Preparation strategies for 1D assemblies can be broadly defined as methods that employ a template,[137,306−308] apply an external force,[309−311] or chemically link nanoparticles together.[312−318] Some examples of nanoparticle chains produced by these approaches include (i) the selective loading of nanoparticles into nanoporous alumina membranes[306,307] or holes[319] and trenches[137,308] fabricated by lithography, (ii) the magnetic field induced formation of chains from bimetallic (magnetic and plasmonic) nanoparticles[320] or the electric field assisted fabrication of nanoparticle chains,[311] and (iii) the molecular linking of nanospheres using alkanedithiols,[318] mercaptoethanol,[321] or cysteine[322] as bridges. Interparticle distances can be controlled through the size of the capping material and the linker molecule or by first coating the nanoparticles with a silica shell of varying thickness.[323] An interesting approach of connecting spherical nanoparticles in a designed and controllable manner includes the selective functionalization of alkanethiol-protected gold nanospheres at the two polar defects, followed by linking them with a molecular bridge in a condensation reaction.[315] Other elegant approaches are the covalent attachment of asymmetrically functionalized gold nanospheres to polymer chains[314] and the preparation of left-handed gold nanoparticle double helices using specifically designed peptides.[324]

Despite the reduced symmetry of nanorods compared with spheres, it is actually straightforward to align gold nanorods end-to-end by taking advantage of the fact that the nanorod ends are composed of a different crystallographic facet compared to the nanorod sides, allowing the selective end-binding of thiols.[313,317,325−328] For example, Thomas et al. have used thioalkylcarboxylic acid based bifunctional molecules to longitudinally link gold nanorods.[325] The thiol groups are thought to

bind to the nanorod ends, while polymerization is facilitated through hydrogen bonding. Figure 22A shows TEM images in the absence and presence of the molecular linker. The extinction spectra recorded for different concentrations and various times after adding the linker molecules are given in Figure 22B, which shows the emergence of a coupled plasmon resonance that is even further red-shifted than the longitudinal mode of the constituent gold nanorods. Through binding of hydrophobic polymer chains to the ends of hydrophilic gold nanorods, metal−polymer analogues of amphiphilic triblock copolymers have also been created.[327] Controlling the solvent quality for this amphiphilic ABA system then yields a variety of other structures, including chains and rings. Rings of nanoparticles have also been prepared by using breath figures as dynamic templates.[329,330]

Optical characterization of 1D nanoparticle assemblies has been performed mostly by ensemble spectroscopy on chemically linked nanoparticle chains in solution showing that plasmon coupling causes a second red-shifted band to emerge.[321,322,331−333] Because of the distributions in nanoparticle size, chain length, and geometry (i.e., straight, coiled, branched, etc.) and a dynamic averaging in solution over different chain orientations and conformations, the spectra mainly show two broad plasmon resonances. One resonance is peaked at the same wavelength as the monomer, and a second one is shifted to longer wavelengths. The amount of red-shifting was found to depend on interparticle separation[332] and chain length,[321,322] in agreement with calculations.[322,331,334,335] Because this behavior resembles that of nanorods with different aspect ratios, calculations have modeled these extinction spectra to a first approximation as arising from straight linear chains with varying length.[333,335] Qualitative agreement between the calculated and experimentally observed spectral features was indeed achieved. In order to simulate the optical properties of more realistic chains, the geometry of a typical nanoparticle chain was taken from a TEM image obtained after depositing the chains from solution.[331] Considering that the geometry of a single chain is only a representative example of all the other chains and their possible conformations present in solution, good agreement was observed for the comparison of the calculated single chain spectrum with the ensemble extinction measurement.

Because of the structural inhomogeneities that give rise to a spectrally broad plasmon response and an often unknown solution phase chain conformation, a quantitative analysis of the plasmonic properties of 1D nanoparticle chains made by chemical methods as a function of chain composition and geometry is difficult to obtain by ensemble spectroscopy techniques. In order to solve this problem, correlated structural imaging and optical spectroscopy on the same isolated nanoparticle chains can be performed (as also described in section 2.5). Single particle spectroscopic techniques have proven to be ideally suited for examining and distinguishing distributions in heterogeneous samples of molecules.[336,337] However, because of the limited spatial resolution of optical microscopy, it is furthermore necessary that each individual nanostructure to be probed optically is also imaged by SEM or TEM to understand complex structure−function relationships. Using specifically patterned substrates that allow one to identify the same nanoparticles in electron and optical microscopes has made it possible to match plasmonic properties with the morphology of single nanoparticles and nanoparticle dimers.[58,176,177,338−347] A few such studies exist also for extended 1D nanoparticle chains prepared by chemical synthesis and assembly.[320,348−351] For example, Odom

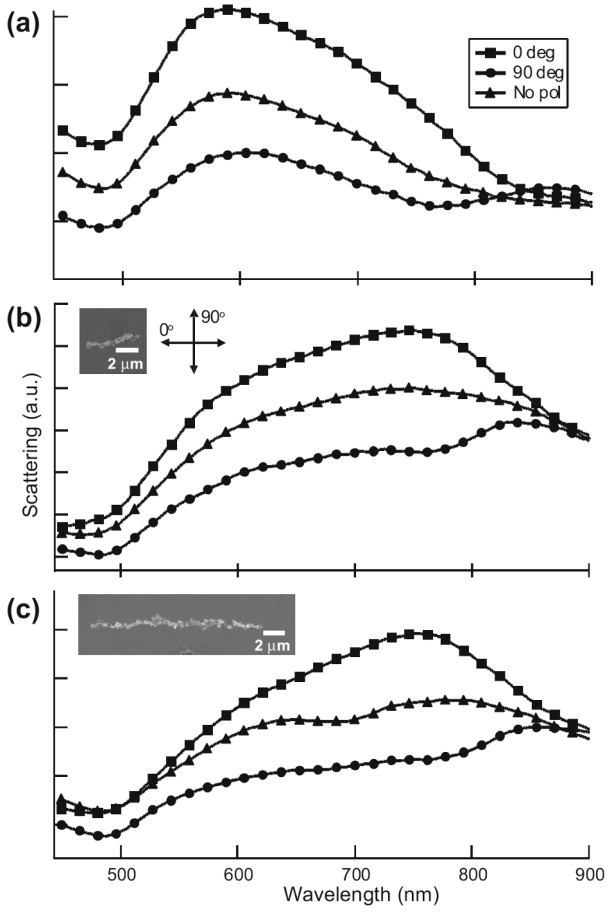

Figure 23. (a) Ensemble scattering spectra of six isolated and randomly orientated Au/Ni pyramids. (b,c) Polarized scattering spectra of 1D chains that were 5 (b) and 17 (c) μm long as shown by the SEM images in the insets. The excitation polarization is also displayed in the inset of panel b. The increased scattering intensity at longer wavelengths for excitation polarized parallel to the chain axis indicates longitudinal plasmon coupling along the chain of pyramids.[320] Reprinted with kind permission from ref 320. Copyright 2007 Wiley-VCH Verlag GmbH & Co. KGaA.

and co-workers measured the polarized dark-field scattering spectra of single Au/Ni bimetallic pyramid chains that were several hundred micrometers long and were aligned by applying an external magnetic field.[320,348] Figure 23 shows ensemble and single chain scattering spectra with the chain morphology given by the SEM images in the insets.[320] The polarization-dependent spectra demonstrate that the plasmon resonances are mainly polarized parallel to the chain axis.

Another example of correlated structural and optical imaging of nanoparticle assemblies is given in Figure 24. Chang et al. have used polarization-sensitive dark-field microscopy and spectroscopy to investigate the near-field plasmon coupling of 40 nm gold nanoparticles that were self-assembled into rings having diameters of 5−10 μm.[350] Scattering spectra recorded along the ring circumference display multiple red-shifted plasmon resonances, polarized parallel to the quasi-1D assembly. Because of the absence of a ring diameter dependence for the spectral position of the collective plasmon peaks, the observed modes have been assigned to multipolar longitudinal resonances of local ring segments. The emergence of several new collective resonances is qualitatively different from the single red-shifted peak

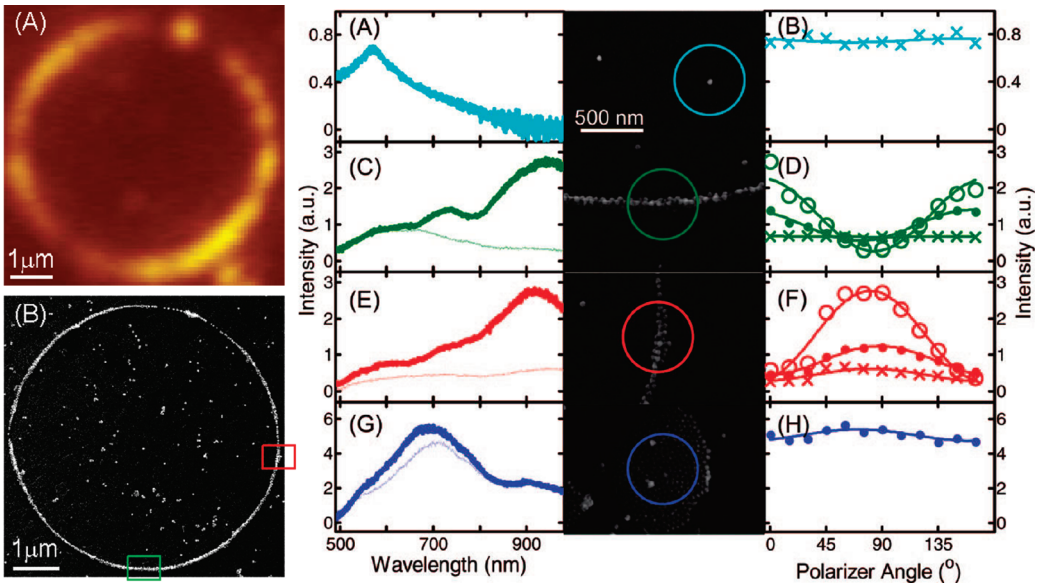

Figure 24. (left) (A) Dark-field scattering and (B) SEM images of a ring composed of 40 nm gold nanoparticles. (right) (A) Scattering spectra of a single nanoparticle, local segments of the ring marked by the green (C) and red (E) squares in the SEM image, and a random aggregate (G). The thick (thin) lines represent scattering spectra recorded with the detection polarization parallel (perpendicular) to the long axis of the ring segment. The SEM images in the middle show the corresponding structures probed by the scattering spectra with the detection areas marked by colored circles. Panels B, D, F, and H illustrate the polarization dependence of the scattering spectra, which was probed at the three scattering maxima for the ring segments.[350] Reprinted with kind permission from ref 350. Copyright 2009 American Chemical Society.

due to the bonding dipole mode observed in other nanoparticle chains.[253−255,257,278] This difference has been attributed to phase retardation effects caused by the large ring thickness of about 100 nm because the rings were several nanoparticles wide, which is also consistent with the fact that multipolar plasmon resonances in nanorods gain strength with increasing nanorod width as discussed more in the next subsection.[352,353] Considering that the individual gold nanoparticles are too small to support multipolar plasmon modes and considering the strong polarization dependence of the dark-field scattering spectra, the plasmon resonances of the nanoparticle ring shown in Figure 24 suggest a collective coupling over several nanoparticles in these quasi-1D nanoparticle assemblies.

The short interparticle distances and resultant strong plasmon coupling achievable in assemblies of colloidal nanoparticles is expected to lead to improved collective properties as well as interesting new phenomena. Further advances in the controlled large scale fabrication of specific nanoparticle based structures are still needed. Plasmonic waveguiding, for example, has been reported on a random dendritic aggregate of 50 nm silver nanoparticles.[354] Surface plasmon mediated energy transfer occurred over a very long distance of 99 μm. However, the absence of an overall aggregate shape prevented directional plasmon propagation, which is a requirement for building and integrating a functional plasmonic waveguide.

4.3. Continuous 1D Nanostructures

Multipolar surface plasmon modes in large nanorods result from phase retardation effects, which lead to broadening and red shifts of the dipole mode as well as excitation of higher-order plasmon resonances at shorter wavelengths.[347,352,355−358] When the size of the nanoparticles becomes comparable to the wavelength of the interacting light, the electrons cannot all be excited in phase with each other. Higher-order plasmon modes in nanorods have been visualized directly by near-field scanning optical microscopy,[359−361] cathodoluminescence spectroscopy,[362] and photoelectron emission microscopy.[363,364] They can be interpreted as standing waves with the longitudinal plasmon resonance occurring when the nanorod length equals about half the resonant wavelength.[352,353,355,357,365−369] Higher-order modes occur at multiple integers of the fundamental dipole mode. This scaling similarity has invoked the analogy of plasmonic nanowires to antennas operating at radio and microwave frequencies. The similarity to radio antennas has therefore sparked interest in using plasmonic nanorods to concentrate and localize optical radiation, beating the diffraction limit of conventional optics. Theoretical modeling of the plasmon modes of metallic nanoantennas has revealed, however, that the nanowire length is typically less than half the wavelength of the dipole resonance because the metal is not a perfect conductor at optical frequencies.[357,365] Furthermore, the resonance maxima depend not only on nanorod length but also on nanorod width.

Experimental characterization of nanorods and nanowires supporting multipolar plasmon modes has been carried out using both ensemble[358,367,370] and single-particle spectroscopy techniques.[347,356] Nanorods with varying length and diameter can be prepared chemically by a seed-growth method,[347,371−373] electrochemical deposition of metals into porous aluminum oxide templates,[358] or electron-beam lithography.[367] An interesting study by Kim et al. reported that the plasmon resonances of large gold nanorods prepared by electrochemical deposition into aluminum oxide templates are preserved when the rod is broken up in smaller pieces by inserting metal spacers in between two smaller gold nanorods.[358] Nickel was chosen as the spacer, which allowed for plasmon coupling between the gold blocks and thereby preserved the overall plasmon modes compared with the continuous nanorods.

dx.doi.org/10.1021/cr200061k |*Chem. Rev.* 2011, 111, 3913–3961

In addition to these antenna modes, nanorods and nanostripes support propagating plasmon modes. Plasmon waveguiding has been observed in metal stripes fabricated by electron-beam lithography[374−378] and chemically grown nanorods.[113,379−388] Improved plasmon propagation can be achieved in single-crystalline nanorods prepared by colloidal synthesis techniques because these wires contain fewer internal defects and have smooth surfaces, which reduce scattering losses.[380,385,386,387,389−393] For example, silver nanowires sustain plasmon propagation over distances of more than 10 μm at near-infrared wavelengths.[379]

For plasmonic nanowires shorter than the propagation length, excitation at one nanowire end and coupling of the plasmons back into free space at the other end can be observed directly in the far-field by emission of photons, because the symmetry breaking at the tips allow for momentum matching between plasmons and photons.[380,381,386,387,394] Similarly, sharp kinks in bent wires can also act as local output as well as input couplers. Dickson and Lyon have demonstrated distal end emission for silver and gold nanowires, which strongly depends on the incident wavelength consistent with the metal dielectric functions.[379] Figure 25A shows end excitation, plasmon propagation, and distal end emission for gold and silver nanowires at 532 and 820 nm. Compared with the gold nanowire, light output is also observed for 532 nm excitation in the silver nanowire because silver is less lossy. In addition to end emission, part of the propagating plasmon wave is reflected at the nanowire ends creating a nanowire Fabry−Perot-type resonator.[385,389,395,396] The emitted light intensity by itself is therefore often not a sufficient parameter for measuring the plasmon propagation length. However, the plasmon decay distance can be determined in the far-field using multiple or variable input and output couplers such as nanoparticles and other plasmonic as well as dielectric waveguides that are positioned at different locations along the nanowire.[113,380,386]

On the other hand, with near-field techniques such as near-field scanning optical microscopy or photoemission electron microscopy, the plasmon propagation length can be measured directly.[364,385,396−398] Especially powerful is the use of phase-sensitive detection in near-field scanning optical microscopy, which allowed Verhagen et al. to investigate the excitation of propagating surface plasmons in gold nanowires by adiabatic mode transformation.[397] Figure 25B shows near-field amplitude and phase of a gold nanowire and a launch pad to its left consisting of a hole array and a tapered waveguide.

By taking advantage of energy transfer between the near-field and fluorescent nanoparticles or molecules, it is possible to indirectly visualize the near-field of propagating plasmons in nanowires using a far-field fluorescence microscope.[391,399] Instead of recording the fluorescence emitted from the fluorophores, Solis et al. exploited the photobleaching of a thin fluorescent polymer film coated on top of gold nanowires thereby creating a permanent map of the plasmon propagation.[400] Figure 25C illustrates this method of bleach imaged plasmon propagation (BlIPP) for gold nanowires excited at 532 nm. Fluorescence images were collected at low excitation powers before and after exposure of the left nanowire end to a focused 532 nm laser beam. The nanowire was visible due to plasmonic enhancement of the polymer fluorescence, which is bleached in response to direct laser excitation, but also away from the laser spot along the wire because of coupling between the propagating plasmons and the polymer chromophores. The bleached fluorescence intensity parallel to the nanowire, as obtained from the difference image, gave the plasmon propagation length. Note that under these conditions the propagation length was too short to observe distal end emission consistent with the results in Figure 25A.

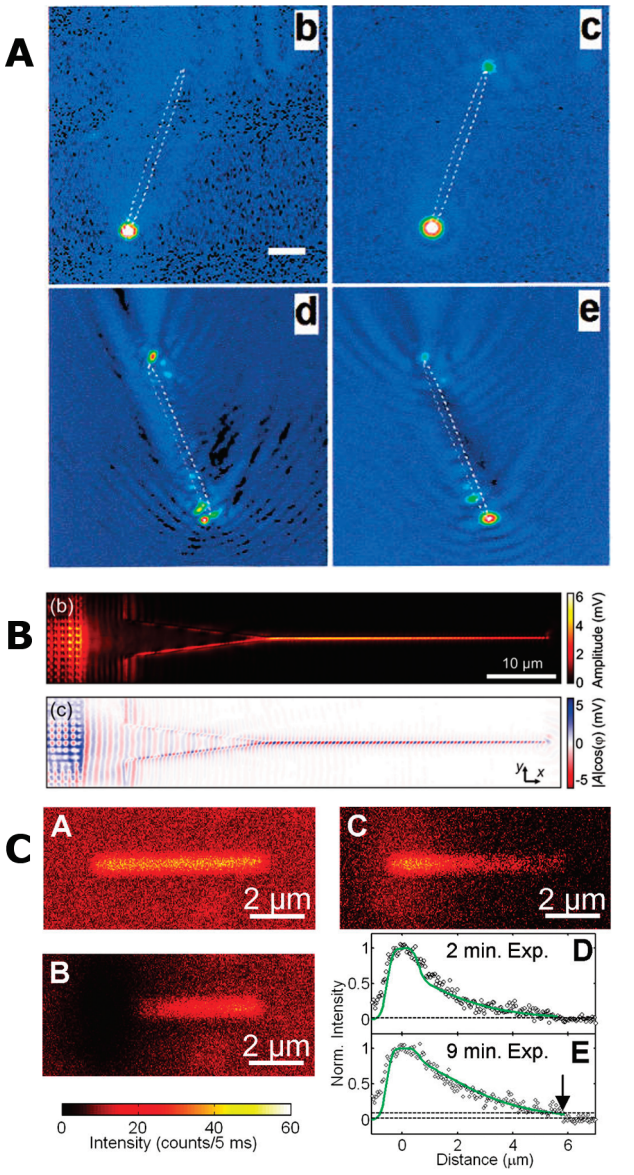

Figure 25. (A) Images of Au (b, c) and Ag (d, e) nanowires exposed to illumination by prism total internal reflection. The dashed lines indicate the positions of the nanowires. The excitation wavelengths were 532 nm for (b, d) and 820 nm for (c, e). Distal end emission is observed except for the gold nanowire excited with 532 nm light (b).[379] (B) Amplitude (b) and phase (c) of surface plasmon propagation in a gold nanowire recorded by the near-field scanning optical microscopy. The width of the nanowire was 150 nm and the excitation wavelength was 1550 nm.[397] (C) Confocal fluorescence image of a 6 μm long gold nanowire coated with a fluorescent polymer before (A) and after (B) continuous illumination of the left wire end with 40 nW at 532 nm for 9 min. The images were recorded with a lower excitation power of 4 pW. (C) Difference image obtained by subtracting panel b from panel a. Width-averaged intensity line sections along the nanowire from the difference images after 2 and 9 min illumination are shown in panels D and E, respectively. The green line is a fit to the data, which yielded a propagation length of 1.7 μm.[400] Reprinted with kind permission from refs 379, 397, and 400. Copyright 2000 American Chemical Society (ref 379), Copyright 2009 American Physical Society. (ref 397), and Copyright 2010 American Chemical Society (ref 400).

As already mentioned, coupling to other nanowires and nanoparticles has been observed, as well as the remote excitation of SERS from molecules located in the junctions between a nanowire and an adjacent nanoparticle.[113,114,383,384,388] Near-field interactions of propagating plasmons with localized nanoparticle plasmons acting as nanoantennas for local interconversion between photons and plasmons are indeed very important, because the direct excitation of propagating plasmon modes at metal−dielectric interfaces is forbidden by momentum conservation and hence is inefficient.[113,114,384,388] Plasmon−photon conversion through coupling to excitons of semiconductor nanoparticles has also been demonstrated and creates even more possibilities for integrating plasmonic components in optoelectronic devices.[292,401−404] Particularly interesting is plasmon coupling between branched nanowires as recently demonstrated in pairs of angled silver wires.[405] Fang et al. found that plasmon coupling and hence the transfer of energy between the nanowires can be controlled through the wavelength and polarization of the incident light, so that distal end emission occurs selectively from either of the two nanowire ends even though only one of the wires is excited.[405] Figure 26 gives an example of two perpendicularly orientated nanowires, as shown in the SEM image, and the controlled output of light at either the same nanowire end for excitation polarized parallel to the wire (top right) or the far end of the other nanowire for the opposite polarization (top left). As shown in the polar plots in Figure 26, the relative emission intensity at the two output positions can be varied continuously by changing the input polarization and incident wavelength. Hence by tuning the wavelength and polarization of the excitation light, it is possible to control the output intensity for both wires and direct light preferentially along either of the nanowires. Such branched nanowire configurations therefore allow one to create controllable plasmon routers, multiplexers, and logic gates for integrated circuits based on nanowires.[405]

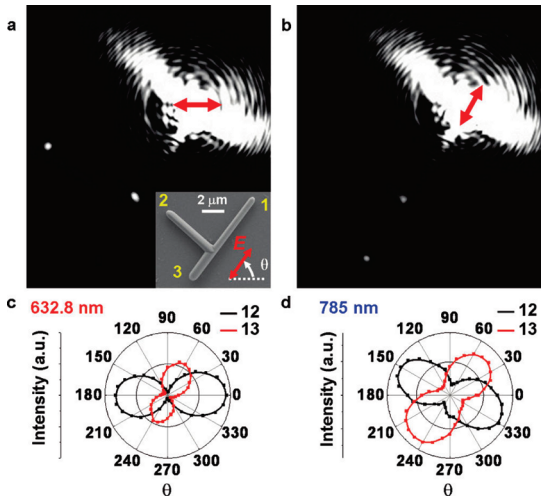

Figure 26. (a, b) Optical images of a pair of branched silver nanowires excited with a 633 nm laser at one of the wire ends. The red arrows indicate the direction of excitation polarization. The inset in panel a shows a SEM image of the two silver nanowires orientated perpendicular to each other. For panel a, the input polarization is adjusted so that all light output occurs at the end of the second wire, position 2, while in panel b, the polarization is optimized for output at the distal end of the wire that is excited, position 3. (c) Emission intensity as a function of excitation polarization θ detected at positions 2 (black) and 3 (red). Excitation was carried out at position 1 with a wavelength of 633 nm. (d) Same as in panel c for 785 nm excitation.[405] Reprinted with kind permission from ref 405. Copyright 2010 American Chemical Society.

5. PLASMONIC FANO RESONANCES

In this section, we will discuss radiative interference and coherence effects such as subradiance, super-radiance, and Fano interference. Although this is a relatively old topic that has been studied extensively in the context of atomic and condensed matter physics, there has recently been a resurgence of interest in these phenomena, more recently observed in interacting plasmonic systems. Plasmonic nanostructures offer a very convenient platform for the study of coherent effects, since the relevant interaction parameters can be tuned straightforwardly by changing the geometry and composition of nanostructures. The topic of Fano resonances in metamaterials and in plasmonic systems has recently been reviewed.[90,406,407] In this section, we will therefore focus more on chemical applications than on applications of negative refractive index materials.

The physical mechanism underlying Fano resonances is the interference between broad continuum-like modes and narrow localized modes.[116] While the original work on Fano interference concerned the quantum mechanical description of autoionizing electronic states of atoms, it has since then been demonstrated that Fano interference is a quite common phenomenon occurring in a wide range of coupled classical oscillator systems. Perhaps the most simple example of Fano interference is provided by the coupled harmonic oscillator model introduced by Alzar et al.[408] The essential physics of the problem, two interfering channels, one of which undergoes an energy-dependent (dispersive) phase shift, is elegantly captured by this simple analytical model. More elaborate models based on coupled mode theory also provide a general and physically intuitive approach for describing Fano resonances.[409,410]

Although Fano interference in plasmonic structures can result from the intrinsic interference of absorption channels such as excitation of conduction electrons and interband transitions,[411,412] we will focus here on Fano resonances caused by the more tunable and pronounced radiative interference between plasmon modes. The key elements underlying these Fano resonances are radiative interference and symmetry breaking. In the following subsection, we will illustrate how structural control of strongly coupled nanostructures can be used to control radiative interference for the creation of broad (super-radiant) and narrow (subradiant) modes. In subsection 5.2, we will discuss how the structural symmetry breaking of a nanostructure can introduce a coupling between subradiant and super-radiant modes and enable Fano interference. In the Applications subsection 6.2, we will discuss how Fano resonances can be used in sensing applications.

5.1. Subradiant and Super-radiant Plasmon Modes

The line width of a plasmon mode is proportional to its lifetime, which is determined by damping mechanisms. The damping of plasmon modes occurs through nonradiative and radiative processes. The nonradiative intrinsic damping processes, such as electron−hole pair excitations and coupling to phonons, are proportional to the imaginary part of the dielectric permittivity at the wavelength of the plasmon. For small nanoparticles, intrinsic damping is the dominant decay mechanism.

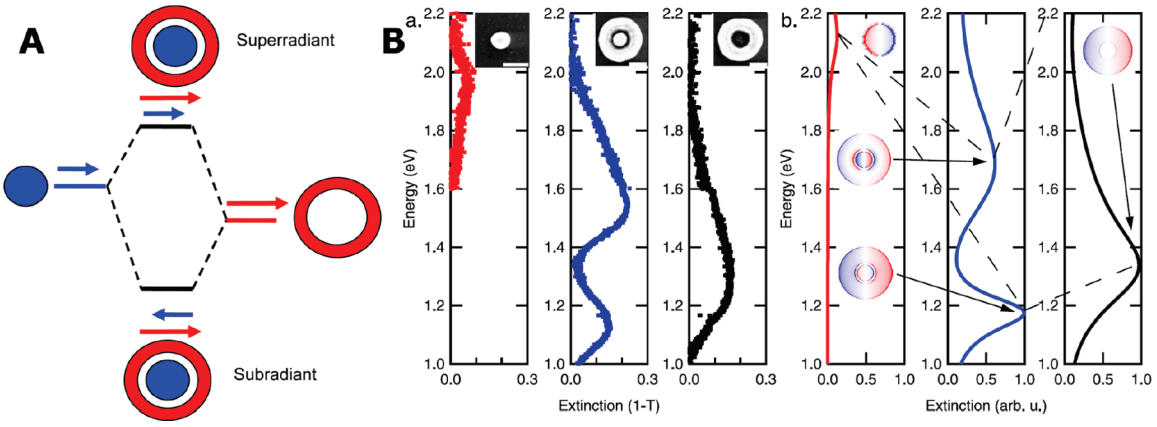

Figure 27. Sub- and super-radiance in a concentric ring−disk cavity. (A) Schematic showing the orientation of the dipole moments of the disk and the ring plasmons in the hybridized states. (B) (left) measured extinction spectra for individual disk, CRDC, and ring; (right) calculated spectra.[425] Reprinted with kind permission from ref 425. Copyright 2010 American Chemical Society.

Radiative damping depends on the multipolar symmetry of the plasmon. Although quadrupolar and higher multipolar charge oscillations in principle can radiate, the dominant damping channel for such modes in submicrometer size particles is intrinsic damping.

The total damping of a dipolar charge oscillation is proportional to the square of the second time derivative of its dipole moment. Since both the dipole moment and the effective mass of a plasmon resonance are proportional to the volume of the nanoparticle, the effective radiative damping of a dipolar plasmon will be proportional to the nanoparticle volume. For dipolar plasmon resonances of nanoparticles of overall diameters larger than 50 nm, radiative damping is typically the dominant decay channel.[413,414]

For a general asymmetric nanostructure, the plasmon modes will have a mixed multipolar composition and several modes may possess finite dipole moments. The damping of such plasmon modes is proportional to the dipolar admixture. Plasmon resonances with small dipole moments are typically referred to as "dark" modes, while modes with a larger dipole moment are referred to as "bright" modes. An example of a simple dark plasmon mode is the antibonding longitudinal dipolar dimer mode discussed in subsection 2.2, where the instantaneous dipolar moments of the two interacting nanoparticles are 180° out of phase, resulting in a cancelation of the total dipole moment of the mode. The probability for excitation of a plasmon mode using an incident plane wave is roughly proportional to the square of its dipole moment (in the strongly retarded limit, the multipolar components of a plane wave can cause direct excitation of multipolar plasmon modes). Thus bright modes will be visible in the optical spectrum and will be broadened. Dark modes cannot be excited with plane waves and are not radiatively broadened. However, dark modes can be excited using near-field excitation or fast electrons, as in electron energy loss spectroscopy.[56,292,415−417] Dark modes are of significant interest in many plasmonic applications, since they can be excited to large quantum numbers (plasmon amplitudes) and provide large EM field enhancements.[418−420]

Since the radiative damping is proportional to the square of the acceleration of the charges in a system, the total radiative damping in an interacting plasmonic structure can exhibit interference effects. For instance, for an ensemble of N nanoparticles, the total dipole moment is the sum of the dipole moments of the individual particles,

$$\vec{P}^{\,\mathrm{tot}} = \sum_{i=1}^{N} \vec{p}_i$$

where $\vec{p}_i$ is the dipole moment of particle i. For a system of identical particles where all the particles oscillate in phase, the total dipole moment is thus $\vec{P}^{\,\mathrm{tot}} = N\vec{p}$, leading to an enhanced radiative damping rate of $R = N^2\ddot{P}^2$. Such a collective enhancement of the damping rate of a bright plasmon mode is a classical analogue of the quantum optical phenomenon of super-radiance. For a plasmon mode where the individual nanoparticles oscillate out of phase, the total dipole moment $\vec{P}^{\,\mathrm{tot}} = 0$, and the mode does not radiate. Such a dark plasmon mode is the classical equivalent of a subradiant mode. We emphasize that the terminology of subradiance and super-radiance are quantum optical phenomena and considerably more intricate than what is discussed above. In the present discussion, which concerns plasmons, our terminology refers to their classical analogues.

Radiative interference effects can be particularly important for arrays of nanoparticles and extended planar nanostructures, where both narrow subradiant and broad super-radiant modes can be excited for different angles of incidence.[249,421,422]

In Figure 27, examples of hybridized sub- and super-radiant plasmon modes in lithographically fabricated concentric ring−disk cavities (CRDC) are shown.[384,423−425] In Figure 27A, the plasmon hybridization scheme for this structure is illustrated. The relevant parent modes are the dipolar disk and ring modes illustrated with the blue and red arrows. Since the system is cylindrically symmetric, the interaction between disk and ring plasmons is diagonal in multipolar index, that is, dipolar disk modes will not interact with quadrupolar or higher multipolar ring modes and vice versa. The resulting hybridized modes are a bonding mode with opposite alignment of the ring and disk dipoles and an antibonding mode with a parallel alignment. The bonding mode with its reduced total dipole moment is subradiant, and the antibonding mode is super-radiant. Figure 27B shows the measured and calculated extinction spectra for CRDC and for the individual disk and ring. The figure clearly shows the reduced width of the bonding mode compared with the parent

disk and ring modes. By increase of the disk diameter while the ring structure is fixed, the bonding mode becomes increasingly subradiant and narrows further.[423,425]

As discussed in the introduction to this section, Fano resonances result from the interference between continuum-like broad super-radiant modes and narrow subradiant modes. In the next subsection, we will show how symmetry breaking can introduce a coupling between such modes.

5.2. Symmetry Breaking and Plasmonic Fano Resonances

Even the simplest possible symmetry breaking, such as replacing one of the nanoparticles in a nanoparticle dimer with a differently sized particle, can lead to coupling between dark and bright modes.[426,427] Another simple example of symmetry breaking is depositing a spherical or cubic nanoparticle on a dielectric substrate as discussed in subsection 2.4. The anisotropic screening introduced by the dielectric substrate (image potential) can mediate a hybridization of the dipolar and quadrupolar plasmon modes of the nanoparticle resulting in a multiply peaked scattering spectrum including Fano interference.[105,428] A large number of recent papers have investigated how more complex structural symmetry breaking can introduce a coupling between dark and bright plasmon modes, resulting in a multitude of new plasmon resonances in the optical spectra.[57,59,61,62,429−442]

For a well-developed Fano resonance, it is also required that the dark mode spectrally overlap the bright mode. Such a spectral overlap can be achieved by tuning the geometry of the nanostructure. If the dark mode is positioned outside the continuum of the bright mode, it will show up as a weak symmetric resonance. The reason that the dark mode appears in the optical spectrum is its interaction with the bright mode, which results in a hybridized mode with some admixture of the bright mode with its larger dipole moment. As the energy of a dark mode approaches the energy of the bright mode, the Fano interference results in a resonance of a characteristic asymmetric line shape. If the dark mode is tuned to lie at a similar energy as the bright mode, the Fano interference results in an antisymmetric line shape, an antiresonance. This situation is commonly referred to as plasmonic electromagnetically induced transparency (EIT). Again, this terminology is borrowed from the significantly more complex quantum optics EIT concept. However, the effect on light transmission is qualitatively the same. Over a narrow wavelength window, the nanostructure does not scatter or reflect light but appears transparent.

Much work has been done recently on plasmon-induced EIT and Fano resonances in lithographically fabricated structures.[52,60,292,442−453] In Figure 28, we show a few examples of Fano interference in systems that have been fabricated and characterized experimentally. Figure 28A shows a Fano resonance in a symmetry-broken plasmonic nanowire array consisting of displaced nanowire dimers.[452] The hybridization diagram shows how bonding (antisymmetric) dark and antibonding (symmetric) bright plasmon modes are formed from the interaction of the wire plasmons. The dark bonding mode shows up as a shoulder on the continuum of the bright antibonding mode. Such hybridization is expected for transverse polarization in a nanoparticle dimer.[427] Figure 28B shows theoretical investigations of EIT in a nanorod trimer.[442] A pronounced Fano resonance shows up in the electric field enhancements indicated by the red arrow in the top panel. Figure 28C shows the measured and calculated extinction spectra from a trimer structure.[449] A Fano resonance appears around 800 nm for vertical polarization. The charge density plots at the bottom show that the interference is caused by a dark collective plasmon mode consisting of individual dipolar nanorod modes oriented such that the dipole moment is very small. Figure 28D shows the effect of symmetry breaking in a gold quadrupolar antenna consisting of two vertically aligned nanorods and one horizontal rod.[447] For the symmetric configuration (top panels), no Fano resonance is observed. As the horizontal bar is displaced downward, a pronounced Fano resonance appears in the reflectance spectra due to the interference of the dipolar and quadrupolar modes.

Figure 29 shows some other recent examples of Fano resonances in lithographically fabricated structures where the interference is due to symmetry breaking. Figure 29A shows the transmission spectra of asymmetric coupled gold split-ring resonators.[453] The Fano resonance is caused by the interference of two hybridized modes, a bonding dark dipolar mode and an antibonding bright mode. The figure shows the effect of the EM coupling. With decreasing separation between the two structures, the dark bonding mode red shifts with respect to the bright mode resulting in less spectral overlap and a weaker Fano resonance. Figure 29B shows a more complex structure fabricated on an elastic substrate.[454] The degree of symmetry breaking can be controlled by stretching the substrate. This highly original structure offers interesting possibilities for dynamical tuning of the optical properties of metamaterials, with significant potential in chemical and biomolecular sensing applications and as an optical switching device. Figure 29C shows the hybridization diagram for a gold nanocross cavity consisting of a cross (X-structure) near a nanorod (I-structure).[455] The XI structure supports several different and very sharp Fano resonances caused by the interference of the quadrupolar and dipolar modes of the individual X and I structures. The two major resonances are a bonding quadrupolar X-mode (BQD) around 1100 nm and a subradiant bonding dipolar mode (BDD) around 1600 nm. In the hybridization diagram, to clearly see the dark quadrupolar resonance for the individual X-structure, it is necessary to increase retardation by using light of grazing incidence.[422] Both the BQD and BDD modes show significant potential for LSPR sensing and will be discussed in section 6.

One problem with lithographically fabricated nanostructures is that their surfaces can be rough and surface scattering contributes to plasmon damping. This results in additional broadening and less sharp Fano resonances. Chemically fabricated nanostructures are more monocrystalline and typically exhibit less broadening due to defects. Fano resonances can also be seen in chemically fabricated nanostructures, such as Fanoshells.[82] The Fanoshell particle is a simple metallodielectric nanomatryushka, consisting of a metallic core surrounded by a dielectric spacer and then a metallic shell. The center of the metallic shell is displaced with respect to the center of the metallic core.[82] This particle has similar optical response to the nonconcentric nanoegg consisting of a dielectric core surrounded by a metallic shell of nonuniform thickness.[456] Due to the symmetry breaking introduced by displacing the core, the dipolar modes of the inner core can interact with quadrupolar and higher multipolar plasmon modes of the outer shell, resulting in Fano interference. The resulting Fano resonance is almost isotropic, that is, independent of the polarization of the incident light, which is important in metamaterials applications.

Fano resonances can also be observed in nanoparticle clusters of sizes ranging from simple heterodimers,[427] trimers,[387] and quadrumers[457] to larger aggregates such as heptamers.[458−463] The larger nanoparticle aggregates are commonly referred to as

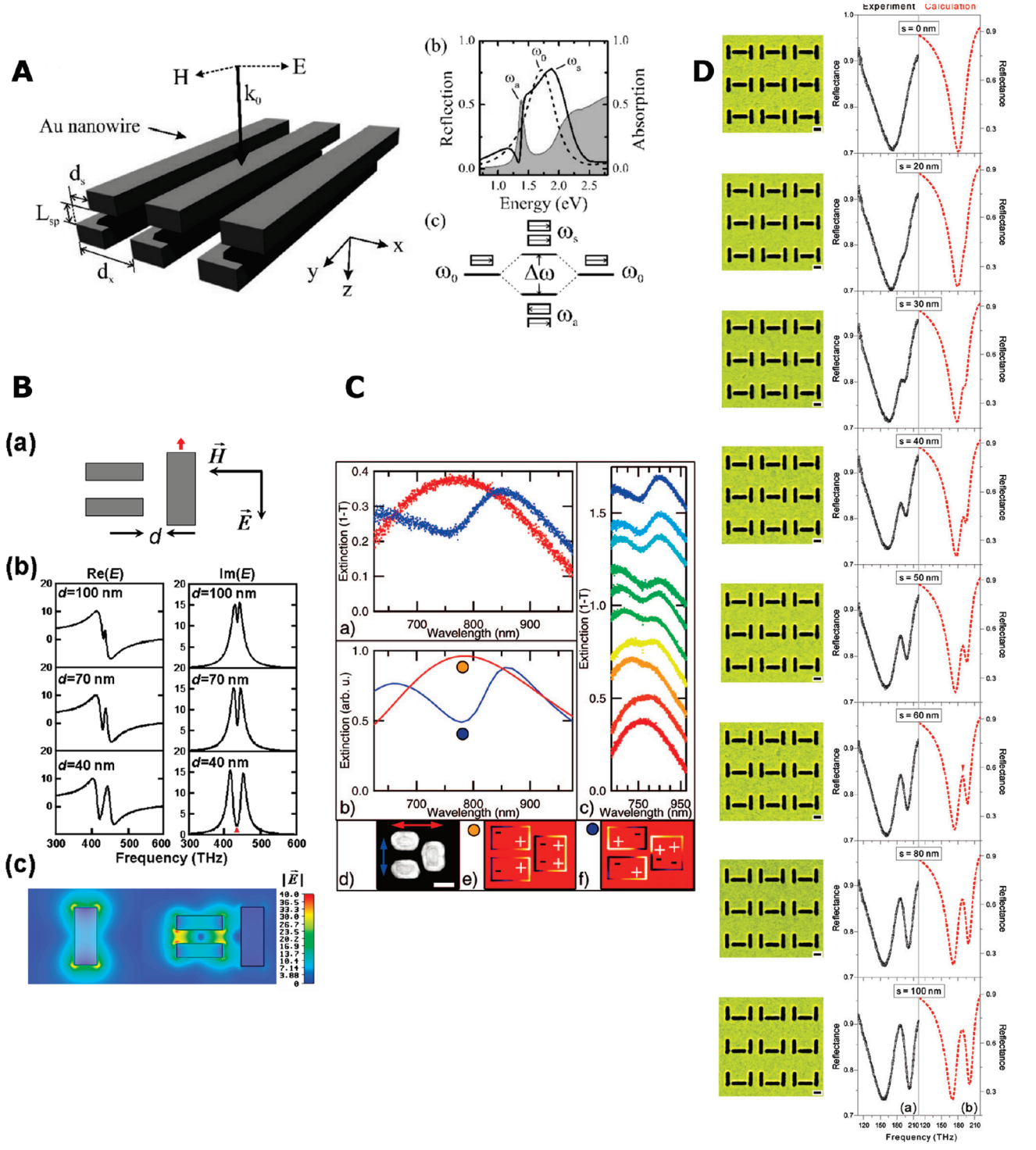

Figure 28. Fano resonances in symmetry-broken nanostructures. (A) Gold nanowire lattice: (left) geometry; (right top) reflection spectrum; (right bottom) plasmon hybridization showing the interaction of the wire plasmon modes.[452] (B) Nanorod trimer: (top) geometry; (middle) real and imaginary part of the electric near-field at the red arrow in the top panel; (bottom) electric field enhancements.[442] (C) Extinction spectra for a gold "dolmen" structure as shown in panel B: (top) measured extinction spectra; (middle) calculated extinction spectra for horizontal (red) and vertical (blue) polarizations. The bottom panels show the plasmon-induced charge densities for the bright (orange dot) and the dark (blue) modes causing the Fano interference.[449] (D) Gold quadrupole antennas: (left) geometry; (right) measured reflection (black) and calculated (red).[447] Reprinted with kind permission from refs 452, 442, 449, and 447. Copyright 2008 American Chemical Society (ref 452), Copyright 2008 American Physical Society. (ref 442), Copyright 2009 (ref 449), and Copyright 2010 American Chemical Society (ref 447).

plasmonic oligomer and exhibit a range of interesting properties. For regular and symmetric oligomers, the description of the collective plasmon modes can be simplified using group theory.[141,464] Cluster modes within the same irreducible representation can interact through their near-fields. Fano resonances in symmetric oligomers are caused by the interaction of a broad

dx.doi.org/10.1021/cr200061k |*Chem. Rev.* 2011, 111, 3913–3961

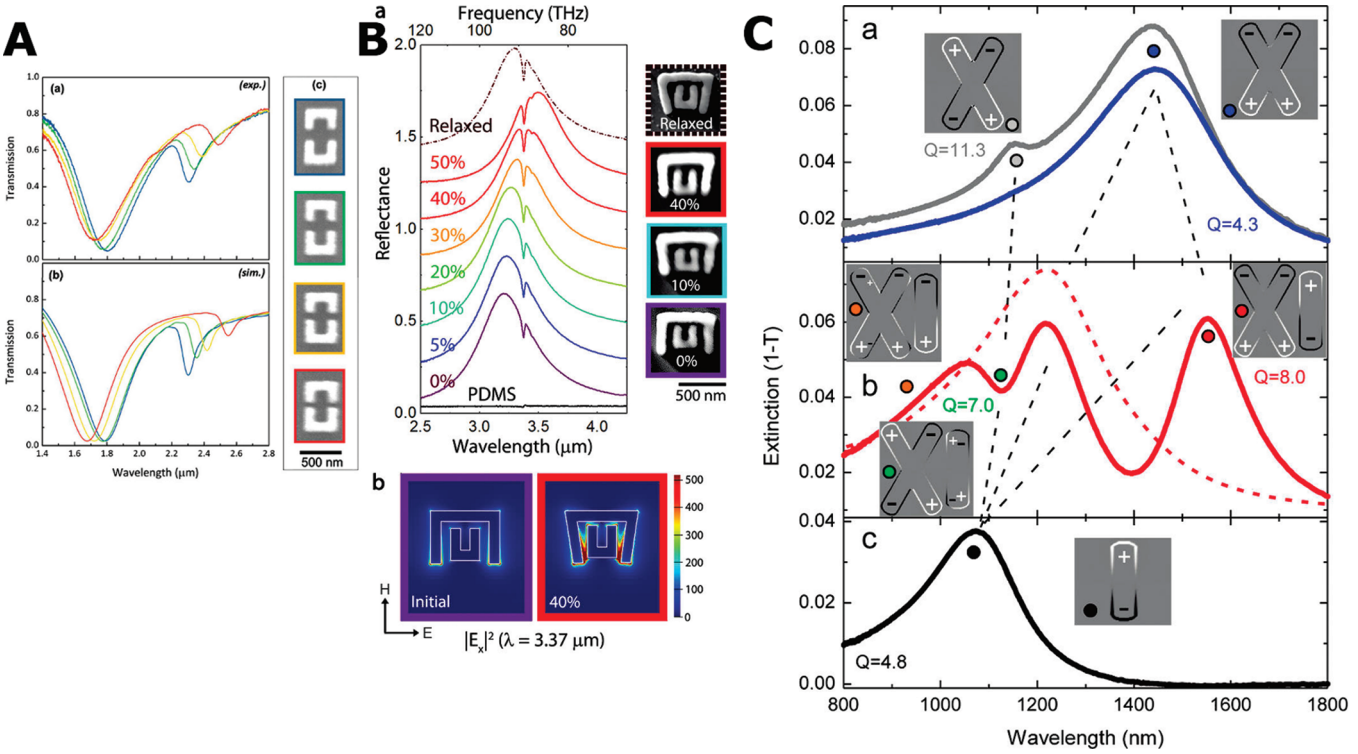

Figure 29. Fano resonances in symmetry-broken gold nanostructures. (A) A symmetry broken split ring resonator:[453] measured (top) and calculated (bottom) transmission spectra for different nanostructure separations. (B) Fano resonances in a symmetry-broken structure fabricated on a stretchable substrate for different substrate stretchings:[454](top) reflection spectra; (bottom) electric field enhancements. (C) Plasmon hybridization diagram in a nanocross cavity:[455] (top) measured extinction for a nanocross for normal (blue) and side (gray) illumination; (middle) measured extinction for the interacting structure; (bottom) measured extinction spectrum for the I-structure. Reprinted with kind permission from refs 453−455 Copyright 2010 Optical Society of America (ref 453) and Copyright 2010 (ref 454) and Copyright 2011 (ref 455) American Chemical Society.

super-radiant mode within a specific irreducible representation with dark modes within the same symmetry representation. For symmetric oligomers with more than four nanoparticles of sufficient size, dark modes with the same symmetry as the bright mode and that spectrally overlap the bright mode are present, and plasmonic Fano resonances are the rule rather than the exception.[459] For smaller oligomers such as the trimer[52,142] or the quadrumer,[457] symmetry breaking is typically required to induce an interaction between the bright and dark modes.

Figure 30 shows a few examples of Fano resonances in plasmonic oligomers. In Figure 30A, we show the scattering spectra of a symmetric heptamer.[462] The top panel shows the plasmon induced charge distribution for the bright mode around 1150 nm and dark mode around 1450 nm. The dark mode induces a clear asymmetric Fano resonance in the extinction spectrum. The two lower panels show the measured and calculated scattering spectra for the structure. In Figure 30B, the transmission spectra for different heptamers are shown for varying interparticle separation.[461] The data beautifully illustrate the effect of interparticle coupling strength on Fano interference.

6. APPLICATIONS

As the field of plasmonics has matured over the past couple of decades and researchers have developed ever more sophisticated control over the design and synthesis of nanoparticles with controlled functionality, numerous applications have been developing. From the earliest experiments in surface-enhanced Raman spectroscopy (SERS),[16,465] plasmon-enhanced fluorescence,[466,467] to the latest applications in biomedicine,[468,469] on-chip waveguiding[272,470] and catalysis, systems of coupled plasmons are leading the way to new technological advances. A comprehensive review of applications that use individual plasmonic nanoparticles is included in a previous paper in *Chemical Reviews*.[471] This section focuses on some real-life applications, especially biomedical in nature, that directly depend upon strongly coupled plasmons and their properties.

6.1. Plasmon Rulers

The formation of a coupled plasmonic nanoparticle pair produces two notable optical signatures: (1) a strong red shift of the plasmon resonance seen in its extinction spectrum and (2) a greatly enhanced field in the interparticle junction formed when the two nanoparticles approach each other. Both of these yield a strongly polarization-dependent response due to the orientation of the interparticle axis of the dimer. These unbleachable, nonblinking, straightforwardly monitored optical properties enable us to use pairs of nanoparticles to monitor nanoscale distances optically and to observe dynamical changes in nanoscale distance induced by chemical or biological processes on the nanometer length scale. The two optical signals enable two types of nanometer-scale metrology tools: one that can monitor interparticle distance according to its color response[70,173] and one that can monitor nanoscale aggregation events by the

dx.doi.org/10.1021/cr200061k |*Chem. Rev.* 2011, 111, 3913–3961

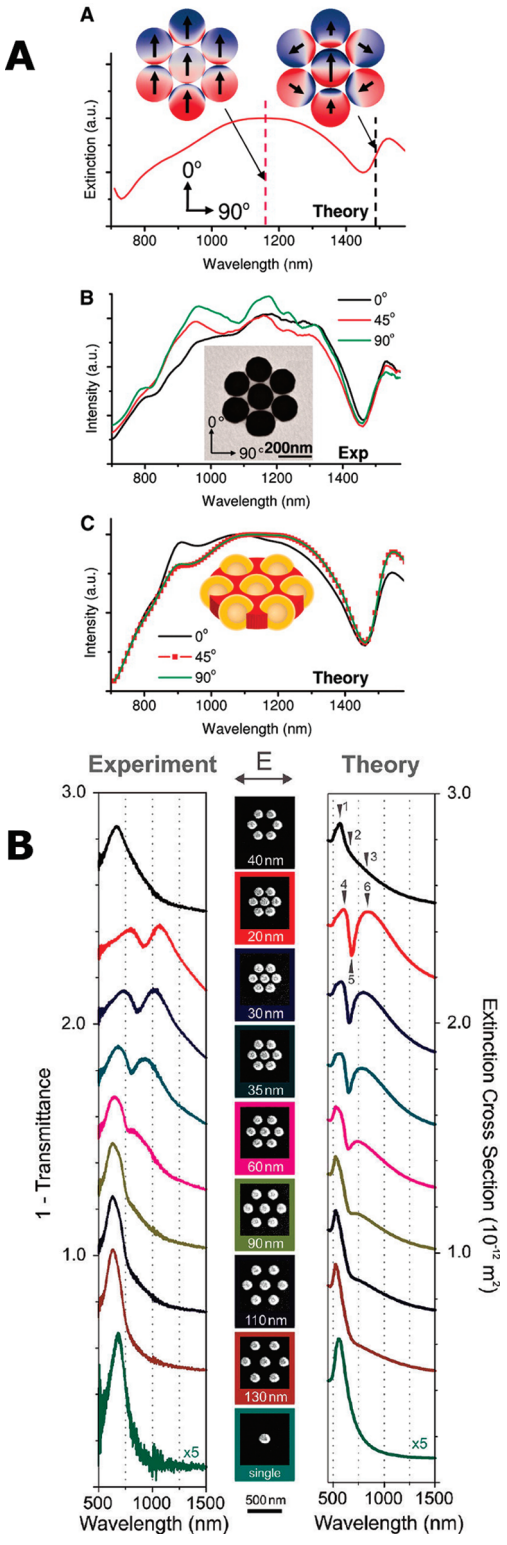

Figure 30. Fano resonances in plasmonic nanoparticle oligomers. (A) Fano resonance in a nanoshell heptamer:[462] (top) plasmon-induced charge distribution; (middle) measured scattering spectra for different in-plane polarization; (bottom) calculated scattering spectra. (B) Fano resonances in a variety of lithographically fabricated plasmonic disk oligomers with different nanoparticle separations:[461] (left) measured transmission; (right) calculated transmission. Reprinted with kind permission from refs 461 and 462. Copyright 2010 AAAS (ref 462) and Copyright 2010 American Chemical Society (ref 461).

formation of a hot spot and the production of a SERS signal.[472] Both types of monitors are developing increased use in the study of dynamical biological processes at subcellular distances.

The concept of the "plasmon ruler" was first demonstrated by linking a pair of small noble metal nanoparticles to each other using a double-stranded DNA tether (Figure 31A).[473] In this structure, the nanoparticle pairs are not "dimers" in the plasmonic sense, since the tethers used may be significantly longer than the nanoparticle diameters. The DNA tether is flexible, however, and a color change due to decreased interparticle distance is produced whenever there is a shortening of the tether. There are many biochemical processes that involve the interaction of DNA with other molecules, these interactions can result in the folding or buckling of the DNA tether.[474,475] As such, these processes can be monitored by the plasmonic dimer color change as the interparticle distance is decreased. This device has been used to study DNA-binding enzymes, specifically the type II restriction endonuclease *Eco*RV, an enzyme that bends the DNA prior to splicing it.[474,475] In addition to the study of DNA−protein dynamics, there are also small molecules of therapeutic importance in cancer (e.g., cisplatin) that are known to bend and kink DNA chains, interfering with the cell reproductive cycle. Plasmon rulers may also be useful in the study of viable drug candidates with this function. Other tethers, such as RNA or proteins, are equally of interest in the design of plasmon rulers, for the study of biochemical processes in which those types of molecules participate. In addition to studying the cleavage kinetics of specific nucleases, these types of experiments also allow the observation of the role of various molecular cofactors that modulate the enzymatic process. This approach may provide more quantitative ways to directly monitor complex biological processes such as enzyme regulation.[474]

While an ideal tool for the study of biological processes, the plasmon ruler concept can also be used to develop an optical strain monitor.[476] By fabricating a 2D array of interacting nanoparticles on a flexible substrate, strain of flexion induced on this patterned substrate will be visible optically. A 2D plasmonic array allows the directional monitoring of strain in the 2D structure by the polarization dependence of the observable optical color shifts.

Plasmon rulers based on the enhanced SERS response of nanoparticle dimers can also be used to study specific biological events. While this approach does not facilitate an optical "readout" of interparticle distance, it provides a strong optical signature when two nanoparticles are in close proximity. This approach was recently used to study the dynamics of receptor aggregation on cells.[472] Cells have receptors on their surfaces that mediate virtually all cellular signaling and communication processes. When specific molecules bind to cellular receptors, these receptors can aggregate on the cell surface, a process that can then initiate specific intracellular events. An example of this is the binding of certain specific molecules, such as adrenaline, to the andrenergic receptors on the surface of cardiac cells, which trigger the contraction of these cells and the beating of the mammalian heart. Receptor aggregation is vital to this process, but our ability to monitor the aggregation of receptors on cell surfaces is quite limited. Plasmonic nanoparticles, bound to specific cell surface receptors, can be designed to produce a SERS signal upon pairwise (and cluster) aggregation (Figure 31B). This detection method can be overlaid with other cell imaging modalities to identify the onset and the specific location of the combined plasmonic−receptor aggregates.

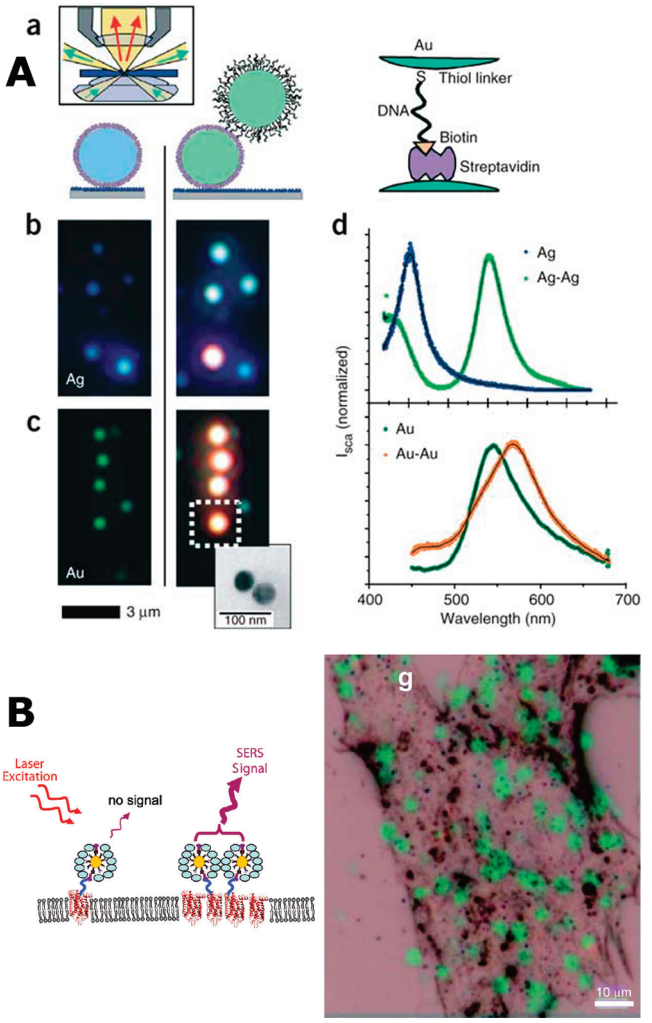

Figure 31. (A) Assembly and properties of plasmon rulers. (a) Nanoparticles functionalized with streptavidin are attached to the glass surface coated with BSA−biotin (left). Then, a second particle is attached to the first particle (center), again via biotin−streptavidin binding (right). The biotin on the second particle is covalently linked to the 3′ end of a 33 base pair long ssDNA strand bound to the particle via a thiol group at the 5′ end. Inset: principle of transmission dark-field microscopy. (b) Single silver particles appear blue (left) and particle pairs appear blue-green (right). The orange dot in the bottom comes from an aggregate of more than two particles. (c) Single gold particles appear green (left) and gold particle pairs orange (right). Inset: representative transmission electron microscopy image of a particle pair to show that each colored dot comes from light scattered from two closely lying particles, which cannot be separated optically. (d) Representative scattering spectra of single particles and particle pairs for silver (top) and gold (bottom). Silver particles show a larger spectral shift (102 nm) than gold particles (23 nm), stronger light scattering, and a smaller plasmon line width. Gold, however, is chemically more stable and is more easily conjugated to biomolecules via −SH, $-NH_2$ or −CN functional groups.[473] (B) (left) Antibody-conjugated Ag nanoparticles designed to bind to specific receptors on a cell surface: the nanoparticle surfaces are passivated with bovine serum albumin to prevent permanent aggregation. When receptor aggregation occurs, the aggregated nanoparticles produce a SERS signal. (right) Andrenergenic receptor aggregation, a process that controls the beating of the mammalian heart, is monitored on mouse cardiac myocyte cells using plasmon-ruler-induced SERS.[472] Reprinted with kind permission from refs 473 and 472. Copyright 2005 Nature Publishing Group (ref 473) and Copyright 2009 American Chemical Society (ref 472).

6.2. Localized Surface Plasmon Resonance (LSPR) Sensing

The plasmon resonance frequency of a nanoparticle or nanostructure is determined by the frequency-dependent dielectric function of the metal, the shape and size of the nanoparticle, and the dielectric function of the surrounding media.[413,414,477] Wet chemical synthesis methods have made it possible to fabricate plasmonic nanoparticles with a variety of shapes (spheres, triangles, rods, cubes, stars, bipyramids, nanoshells, nanorice, etc.).[373,478−488] The localized surface plasmon of these nanoparticles can vary across the visible into the near-infrared region.[489]

Modifying the embedding medium leads to a change in the spectral position of the plasmon resonance. Localized surface plasmon resonance (LSPR) sensing is based on monitoring this spectral change due to changes in the surrounding medium.[490,491] The LSPR sensitivity of a plasmonic nanoparticle is typically evaluated by its figure of merit (FoM),[488] defined as the ratio of the plasmon frequency shift per refractive index unit change in the surrounding medium divided by the width of the spectral resonance peak. This accounts for both the absolute shift in the resonance peak position and the width of the resonance in defining the sensitivity of an LSPR sensor. Large shifts with narrow resonances lead to higher FoM and sensitivity. The highest FoM reported for any individual nanoparticle is 5.4 for a sharply spiked gold nanostar.[490]

Recent reports of planar nanostructures and nanoparticle clusters that show collective plasmon modes and coherent phenomenon such as EIT and Fano resonances have been described in previous sections. The Fano resonance in these clusters arises from the interference between the coupled plasmon modes of the constituent nanoparticles. The narrow Fano resonances are extremely sensitive to the surrounding dielectric environment and shifts in a narrow line width are easier to detect. Thus strongly coupled systems that can sustain Fano resonances hold tremendous potential as LSPR sensors.[407,424,425,449,450,459,462]

One of the first predictions of the LSPR sensitivity for Fano resonances was in the nonconcentric disk−ring cavity (NCDRC) discussed in a previous section. Theoretical calculations of the FoM for Fano resonant plasmon modes have suggested an extraordinary potential for LSPR sensing. In Figure 32A, we show the calculated extinction spectra for a NCDRC on a glass substrate for full and partial dielectric filling of the cavity. The spectra show a strong red shift of both the Fano resonance around 1500 nm and the subradiant mode around 3000 nm. For full filling of the cavity, the FoM is predicted to be 7.3 for the subradiant mode and 8.3 for the Fano resonance.[424] Clearly such a large FoM would enable high-sensitivity LSPR sensing.

A plasmonic nanocube on a dielectric substrate can also exhibit a Fano resonance with very large FoM. For a silver nanocube on a glass substrate, the FoM has been measured at 5.4,[488] but further optimizations of this structural motif suggests that it may be possible to achieve FoMs of the order 10−20.[428] Another simple planar structure consisting of a slot cut in a uniform 30 nm thick gold film acting as a dipole antenna is coupled to a slot quadrupole antenna (Figure 32C).[292] The structure supports a Fano resonance in the reflectance spectrum when the dipole slot antenna is offset from the center of the quadrupole antenna. The experimentally observed Fano resonance in an array of these coupled antennas and the theoretically predicted spectrum are shown in Figure 32C. The depth of the resonance can be tuned by changing the offset between dipole antenna and the quadrupole antennas (Figure 28D). The

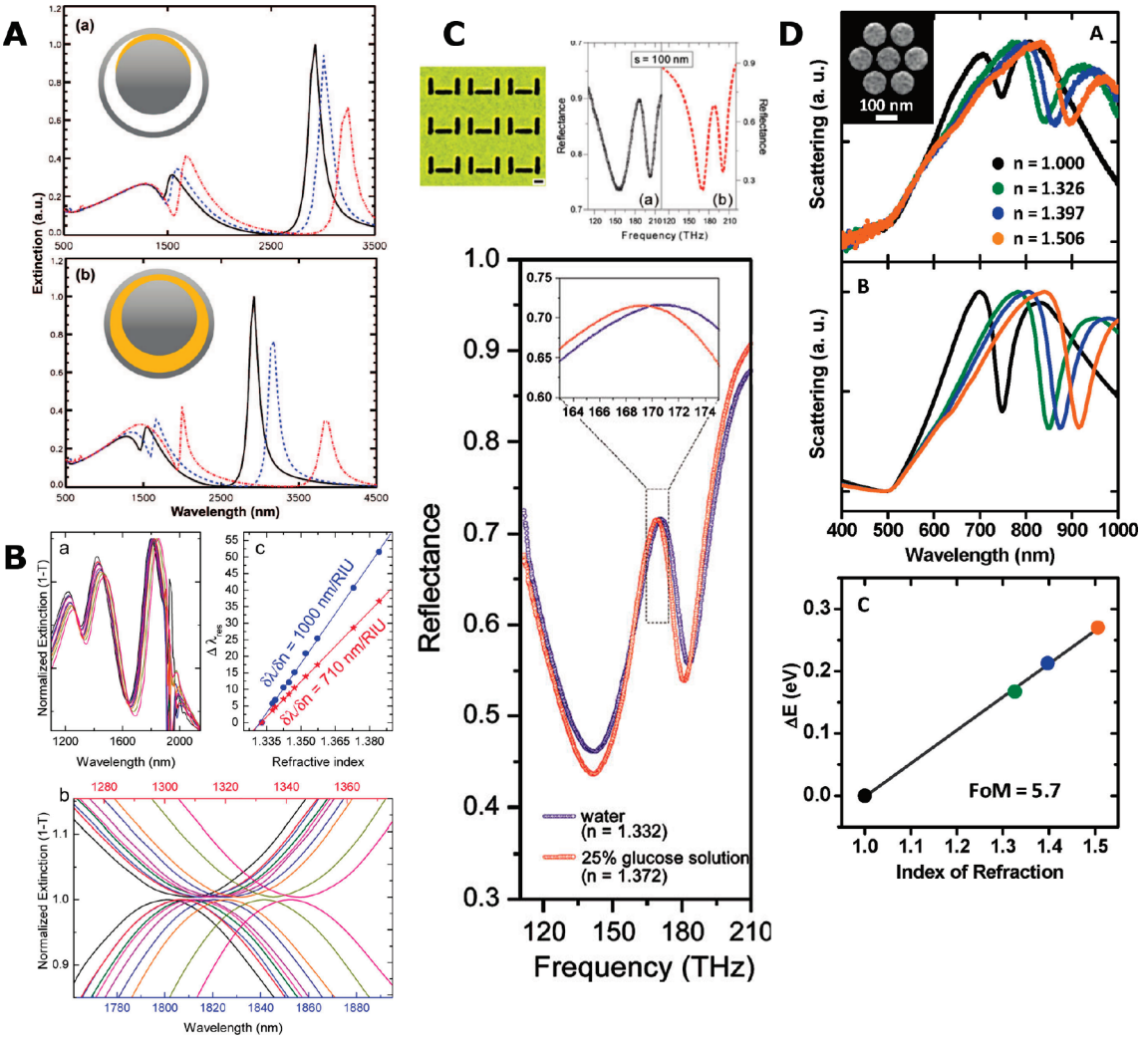

Figure 32. LSPR sensing using Fano resonances. (A) Theoretical calculations of the extinction spectra for a nonconcentric ring−disk nanocavity for different dielectric fillings $\varepsilon = 1$ (black), $\varepsilon = 1.5$ (blue), and $\varepsilon = 3$ (red):[424] (top) spectra for partial filling of the cavity; (bottom) spectra for complete filling of the cavity. (B) LSPR sensing using glycerol solutions of different concentrations on the XI structure in Figure 29C:[455] (top left) normalized extinction spectra; (bottom) zoom-in on the extinction spectra around the BDD (bottom curves) and the BQD (top curves) for different dielectric permittivities; (top right) LSPR shift of the BDD (blue) and BQD (red) peaks. (C) Experimental tuning of the EIR-like reflectance spectrum for the structure in Figure 28D with $s = 60$ nm by changing the liquid that is adjacent to the gold nanostructures from water to 25% aqueous glucose solution. The increase of the refractive index from water ($n = 1.332$) to 25% glucose solution ($n = 1.372$) causes a red shift of the resonance. Inset: enlarged figure of the reflectance peaks as highlighted by the dashed box.[447] (D) (a) LSPR sensing for heptamer. Four polarized scattering spectra are shown for different media (air, black; methanol, green; butanol, blue; immersion oil, orange). The values for the refractive indices of each medium are shown in the figure. (b) FDTD simulations corresponding to the experiment. (c) Linear plot of the LSPR shifts of the Fano resonance vs refractive index of the embedding medium.[460] Reprinted with kind permission from refs 424, 455, 447 and 460. Copyright 2008 (ref 424), 2011 (ref 455), and 2010 (refs 447 and 460) American Chemical Society.

sensitivity of the nanostructure was demonstrated by measuring the reflectance spectrum in water ($n = 1.332$) and a 25% glucose solution ($n = 1.372$). The shift in the spectral position of the reflectance peak can be seen in the lower panel of Figure 32B. The FoM sensitivity of this structure was calculated to be ~3.8. The advantage of the coupled dipole−quadrupole antenna system is the ease of fabrication and that as an LSPR sensor the surrounding media can fill the slot antennas.

In Figure 32B, we show measurements of the extinction spectra for the XI structure discussed in Figure 29C in glucose solutions of various concentrations. Both the BQD Fano resonance around 1300 nm and the subradiant BDD mode around 1800 nm exhibit large red shifts with increasing refractive index (glucose concentration). This is particularly clearly illustrated in the bottom panel, which is a zoom-in of the shifts of the BDD and BQD. The measured FoMs for these two modes are 4.6 and 4.7, respectively, only slightly smaller than the theoretical predictions of 5.0 and 6.6.

One of the simplest nanoparticle oligomer geometries investigated for LSPR sensing is a planar heptamer cluster with one nanoparticle in the center of a six nanoparticle ring (Figure 32D, inset).[460] The clusters were fabricated by electron beam lithography on a silicon substrate with a thick layer of SiO_2. Each gold disk in the cluster is 30 nm thick and 128 nm in diameter. Dark field scattering spectroscopy on individual clusters embedded in various dielectric media [air ($n = 1.0$), methanol ($n = 1.326$),[492] butanol ($n = 1.397$),[492] and index matching oil ($n = 1.506$, Cargill laboratories, internal documents)] shows the spectral shift in

dx.doi.org/10.1021/cr200061k |Chem. Rev. 2011, 111, 3913–3961

different media (Figure 32D). The Fano resonance shows a distinct red shift with increasing refractive index from 750 nm in air ($n = 1$) to 900 nm in immersion oil ($n = 1.5$). Finite difference time domain (FDTD) simulations shown in Figure 32D match the spectral shifts observed experimentally. The FoM determined from the experimental shifts is 5.7, which is the highest measured LSPR sensitivity for an individual plasmonic nanostructure. This LSPR sensitivity is observed in a nanostructure that is not optimized; therefore the sensitivity could be further enhanced by increasing the size of the disks in the cluster and reducing the gaps.

The concept of Fano resonance-based LSPR sensing is very recent, and we expect that the field will advance significantly in the near future. The structures investigated so far have not been optimized, and it is likely that much larger FoM can be achieved by further tuning of the plasmonic resonances or by using different metallic materials than gold or silver.

6.3. Surface-Enhanced Raman Scattering (SERS)

Surface-enhanced Raman spectroscopy is a very attractive spectroscopic technique because the Raman signal contains detailed information of the vibrational levels in the analyte and thus may be useful for chemical detection. Because the SERS signal depends upon the 4th power of the local field ($\sim E^4$ dependence) and extremely high fields are possible in the junctions between nanoparticles, SERS enhancement factors of greater than 10^6 have been reported by numerous researchers. This enhancement is sufficient for single or few molecule detection making SERS an extremely useful technique for chemical and biomolecular detection.[18,493,494]

The easily achieved high sensitivity of SERS also makes it an attractive technique to study one of the most complex environments that is not easily accessible otherwise: inside live cells.[495−500] Sousa et al. reported the first in vivo SERS measurements using aggregated gold colloid.[495] Gold nanoparticles were mixed with imidazole to form small aggregates. Imidazole is an important organic component of many proteins and enzymes. At slightly basic pH (pH ≈ 8), imidazole is protonated, and the positively charged imidazole bridges the citrate-stabilized net negatively charged gold nanoparticles.[501] The extinction spectrum of the gold nanoparticle solution before and after addition of the imidazole (Figure 33B) shows a strong LSPR peak at 520 nm for the gold nanoparticle in the borate buffer solution (pH ≈ 8) without the imidazole added and a strong shift to ∼800 nm after the addition of the imidazole. The corresponding normal Raman of imidazole in borate buffer (red curve) and the SERS spectrum (blue curve) are shown in Figure 33A. The weak imidazole ring mode at 931 cm^{-1} is highly enhanced in the SERS spectrum and shifts to 954 cm^{-1}.

To monitor the SERS spectrum *in vivo*, the Au−imidazole solution was injected into tumors in tumor-bearing mice. A fiber optic probe with a focal length of 7 mm was positioned 3 mm above the tumor, and SERS spectra were collected through the skin using a 785 nm laser and 15 s integration times. The SERS spectrum *in vivo* (Figure 33C, blue curve) is dominated by the strong imidazole ring mode. This is absent in the control measurement (green curve) taken from tumors that were injected with plain buffer solution.

Kneipp et al. have recently demonstrated *in vitro* mapping of pH inside live cells.[498,500,502] By monitoring of the pH in cells over time, important physiological information at the subcellular level may be obtained. The SERS spectrum of 4-mercaptobenzoic acid (pMBA) depends upon the pH of its environment, and the thiol moiety facilitates conjugation to gold surfaces.[503] Gold nanoparticles (30−50 nm) were incubated with 10^{-5} M pMBA solution. Next the pMBA conjugated nanoparticles or nanosensors were redispersed in culture medium and incubated with NIH/3T3 (mouse fibroblast cells) grown on coverslips. Following incubation, the cells on the coverslips were rinsed out with phosphate buffer solution at different times. SERS spectra were collected using a customized Raman microspectroscope. Raster scans over single cells were carried out using a computer-controlled $x-y$ stage with an 830 nm laser and a spot size of $\sim 2 \times 10^{-8}$ cm^{-2}. Thus a complete pH map of the cell can be created.

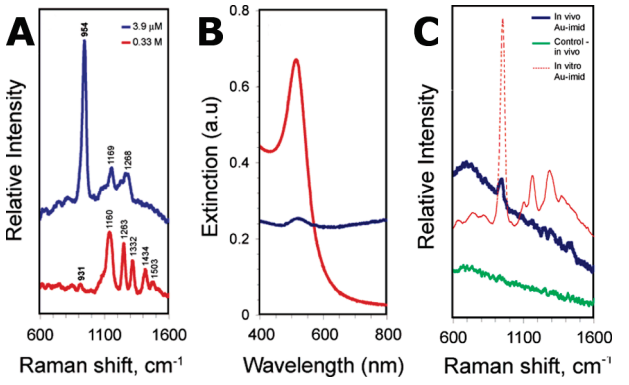

Figure 33. (A) Raman signal of 3.9 μM imidazole in 0.33 mM borate buffer, pH 8.0, enhanced by interaction with 17 nm Au NPs (blue spectrum, 60 s integration) and Raman spectrum of 0.3 M imidazole in borate buffer (red spectrum). Plots are offset for clarity. (B) UV−visible absorption spectra of a mixture of 3.9 μM imidazole in borate buffer with 17 nm Au NPs (blue spectrum) and 17 nm Au in borate buffer (red spectrum). Noninvasive NIR−SERS detection across skin in a tumor-bearing mouse that received 300 μL of Au−imidazole clusters (7.8 μM imidazole) administered locally in the tumor xenograft. SERS spectra description: the blue curve (*in vivo*) is the spectrum generated by the Au−imidazole assemblies inside the tumor with 15 s integration; red curve (*in vivo*) is the spectrum from tumor prior to administration of Au−imidazole assemblies injection with 15 s integration; green (*in vitro*) is the spectrum from Au−imidazole complexes in solution measured in a glass cuvette with 5 s integration.[495] Reprinted with kind permission from ref 495. Copyright 2006 American Chemical Society.

The bright field images in Figure 34 show the cells at three different time points when the coverslips were removed from the media and rinsed. The dark, electron dense spots are located where the gold nanosensors have accumulated. The SERS spectra from the various endosomal compartments can be seen in Figure 34A at 1 h. The raster scan image and the false color pH map are determined from the ratio of the lines at 1423 and 1076 cm^{-1}. The pH values range from 6.2−6.9 at 1 h to 5−7.4 at 4.5 and 6 h. The distribution of pH values at the later time points are consistent with aging of the endosomes for this cell line. Monitoring the pH distribution and dynamics in living cells can lead to understanding important physiological and metabolic processes inside the cell.

Another modality for SERS of the nucleus and cytoplasmic regions of the cell has been demonstrated by Vitol et al.[496] Aggregated gold colloid is known to be an efficient SERS substrate. Vitol et al. have developed a SERS-active glass nanopipette probe that provides control over positioning the probe in the region of interest. Hollow glass capillaries with ∼100−500 nm tips are functionalized with poly(L-lysine) and then coated

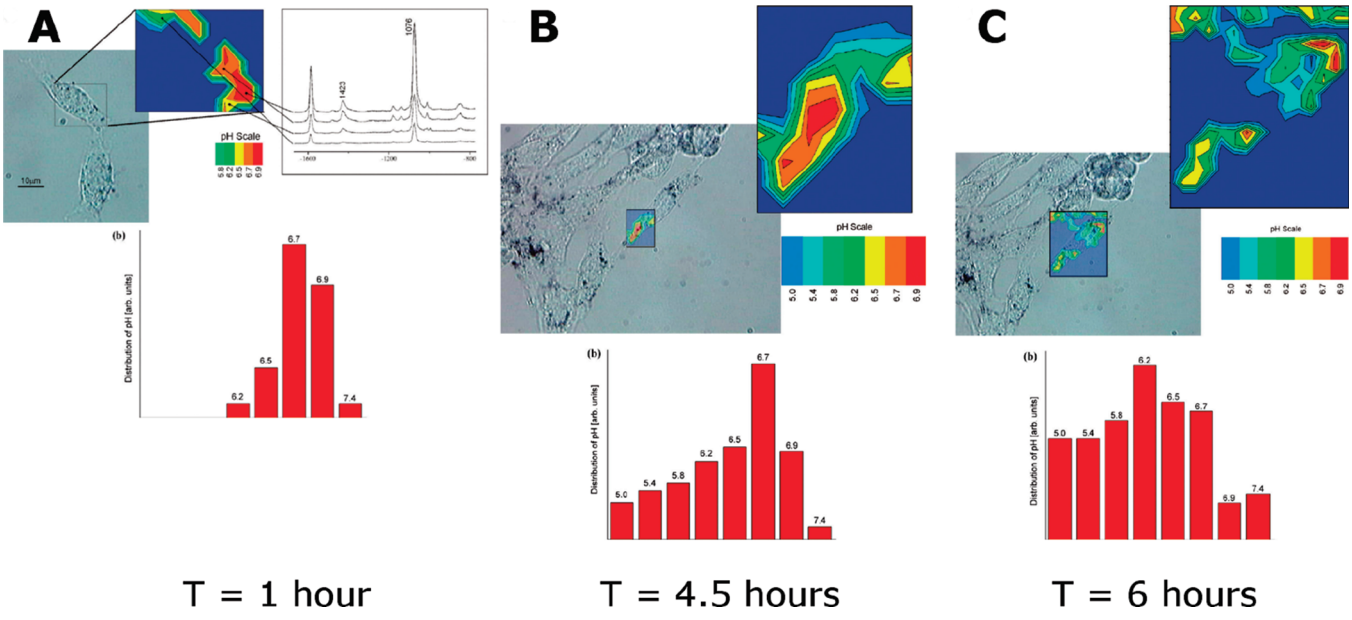

Figure 34. Probing and imaging pH in single live cells at different incubation times with SERS nanosensors. (i) The bright field image shows a 3T3 cell incubated with gold nanoparticles. The displayed SERS spectra are examples for spectra measured in different cellular compartments during a raster scan over the rectangle. The false color plot of the calibrated ratio of the Raman lines at 1423 and 1076 cm^{-1} displays a pH image of the cell. Scattering signals below a defined signal threshold, that is, from places where no SERS signals exist, appear in dark blue. The values given in the color scale bar determine the upper end value of each respective color. (ii) Distribution of pH based on SERS mapping over eight cells.[502] Reprinted with kind permission from ref 502. Copyright 2010 American Chemical Society.

with gold colloid. The time the pipet is incubated in the gold nanoparticle solution determines the density of the attached colloid. A dense coverage where the particles start forming small clusters is optimal for exciting with a 785 nm laser (Figure 35A). The glass pipettes can then be fixed in the pipet holder of a micromanipulator. A stepper motor attached to the micromanipulator allows the pipettes to be positioned and inserted into the cells. The cell membrane and nucleus can be distinguished under a microscope. The excitation laser is focused on the tip of the pipet, and SERS spectra are collected. The SERS spectrum from the nucleus and the cytoplasmic regions are shown in Figure 35B. The spectrum obtained from the cell nucleus has features primarily associated with the high amino acid content (1076, 1222, 1264, 1328, 1361 cm^{-1}) and with DNA (660, 722 cm^{-1}).[498,504] The cytoplasmic SERS spectrum does not show the DNA lines but contains peaks related to proteins present in the cytoplasm.

The nanopipette SERS probe can also be used to monitor cells under external stimulus. The nanopippet was inserted into the cytoplasmic region of the cell, and an aqueous solution of KCl was added to the medium to a final concentration of 55 mM. The KCl provides an external trigger for cellular activity. The presence of the KCl modifies the hydration level of the cell, which in turn modifies the configuration and concentration of the cytoplasmic proteins and other constituents. These modifications are monitored with SERS after the addition of KCl (Figure 35C,D).

6.4. Surface-Enhanced Infrared Absorption (SEIRA)

While Raman spectra provides detailed information of the vibrational levels associated with analyte molecules, a complementary technique that provides additional fingerprinting information about the analyte is infrared absorption. Most molecules have strong infrared absorption bands that are either weak Raman modes or are not easily accessible by Raman scattering measurements.[505] Complementary to SERS, surface-enhanced infrared absorption (SEIRA) can provide several orders of magnitude enhancement of modes in the IR region. Plasmonic substrates usually exploited are ones with a strong resonance in the IR region. Nanowires and rodlike antennas are some of the most popularly used substrates.[119,506−508] For long nanowires, the fundamental antenna resonances can be tuned into the IR and provide large SEIRA enhancements. Electron-beam lithography techniques allow facile fabrication of nanorods like antennas with varying resonances that can be tuned to enhance modes of interest. In addition to the antenna resonances in the IR region, arrays of nanowires with small gaps between the wires provide additional enhancements. Pucci et al. have demonstrated the effect of arrays of nanowires with small gaps by varying the gap size.[508] Gold nanowires of width 60 nm and height 60 nm and lengths varying from 0.3 to 2.5 μm were fabricated on ZnS substrates, which are transparent in the IR region of interest. The wires were spaced either 20 or 60 nm apart along the length of the wire and spaced 500 nm apart across their width. Figure 36A shows a SEM image of the nanowires with a 60 nm gap. Octadecanethiol (ODT) molecules were adsorbed onto the nanowires as an analyte to investigate the SEIRA enhancement. Infrared spectroscopy was performed at an IR beamline of a synchrotron light source with a circular aperture of ~16.7 μm. Eighty-three wires from the sample with 20 nm gaps and 70 wires from the sample with 60 nm gaps were interrogated within the beam. The relative transmittance from the 20 nm gap sample is shown in Figure 36B. For light polarized transverse to the wire, the signal is below the noise level. For light polarized parallel to the nanowires, a broad transmittance minimum due to the plasmon resonance of the nanowire array is seen. The SEIRA

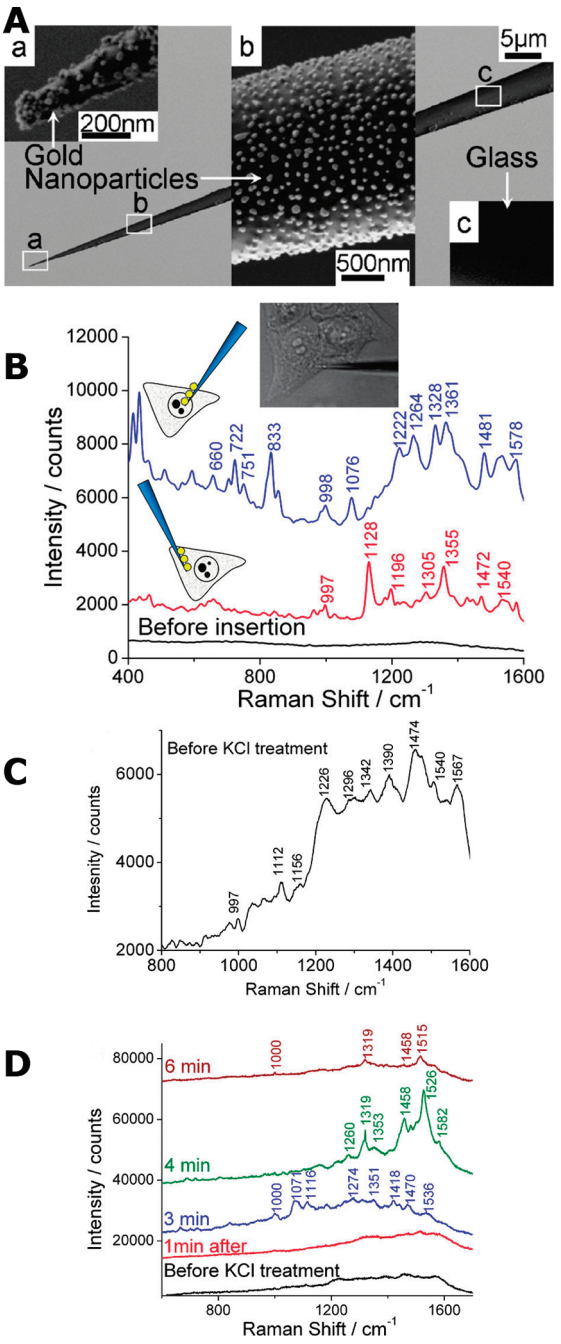

Figure 35. Scanning electron micrographs (SEM) of the SERS-active nanopipette. (A) (a) The nanopipette tip covered with gold nanoparticles; (b) magnified view of the nanoparticle coverage of the nanopipette about 10 nm away from the tip; (c) bare glass surface of the nanopipette. (B) SERS spectra from the cell nucleus (upper spectrum) and cytoplasm (middle spectrum) obtained with the SERS-active nanopipette show distinctly different features. The bottom spectrum (black line) was collected from the nanopipette tip before insertion; 785 nm excitation laser was used. The spectra are offset for clarity. (C) SERS spectrum collected from the nanopipette tip inserted in the HeLa cell cytoplasm and (D) representative time-resolved spectra showing HeLa cell response to treatment with KCl aqueous solution with the SERS-active nanopipette. Time-dependent variation of the cytoplasmic signal has been observed. Data acquisition time was 20 s. The spectra in panel D are offset for clarity.[496] Reprinted with kind permission from ref 496. Copyright 2009 American Chemical Society.

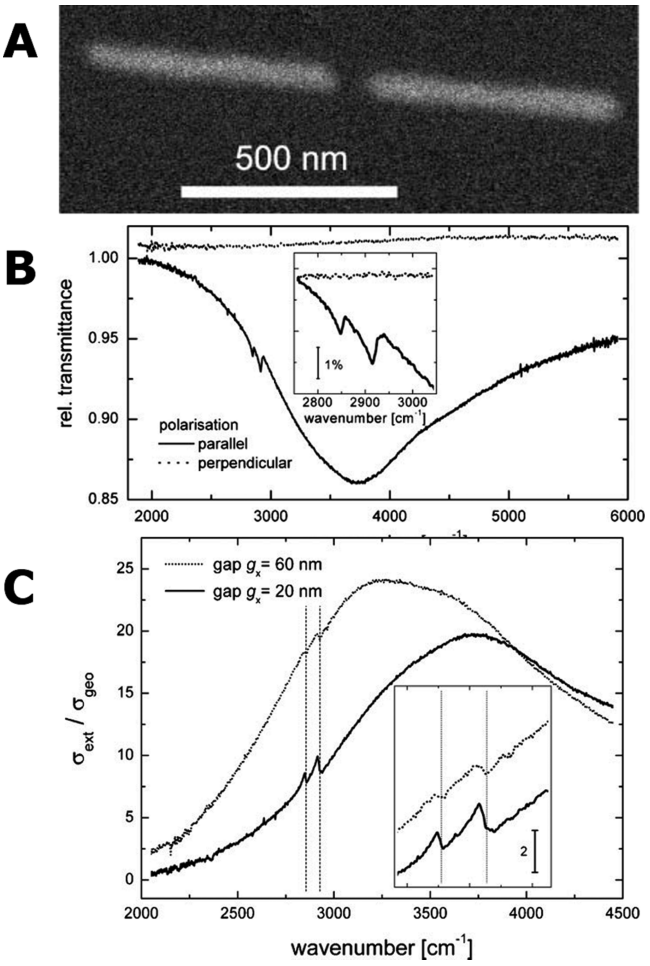

Figure 36. (A) Scanning electron microscopic picture of two nanowires in an array with 60 nm inline distance produced by electron-beam lithography on ZnS. (B) Relative IR transmittance of approximately 83 gold nanorods (L = 500 nm, width w, and height h = 60 nm) in an array with gaps of about 20 nm in x- and 5000 nm in y-direction. Due to the resonant field enhancement the ODT vibrational bands occur for parallel polarization. For perpendicular polarization, the ODT signal remains below the noise level. The inset shows a zoom to the vibrational signals of ODT. (C) Comparison of spectral extinction cross-section (normalized to the geometrical cross-section) of one nanowire covered with an ODT monolayer in an array with gap size 60 nm and gap size 20 nm.[508] Reprinted with kind permission from ref 508. Copyright 2010 Wiley-VCH Verlag GmbH&Co. KGaA.

bands are observed on top of this large minimum, and the inset shows a closer view of the absorption bands. Another interesting observation was that the signal observed from the array with 20 nm gaps is significantly larger than that observed from the sample with 60 nm gaps even though the antenna resonance is detuned from the vibrational levels. The comparative SEIRA signal from both samples is shown in Figure 36C. Thus by tuning the antenna resonance and tuning the gap size, the sensitivity of the SEIRA measurement can be enhanced to achieve attomolar sensitivity. Further optimization may allow even single-molecule sensitivity.

Adato et al. have demonstrated the enormous enhancement achievable by tuning both antenna resonance and the gap size.[506] By tuning of the gap size, the in phase dipolar coupling leads to a

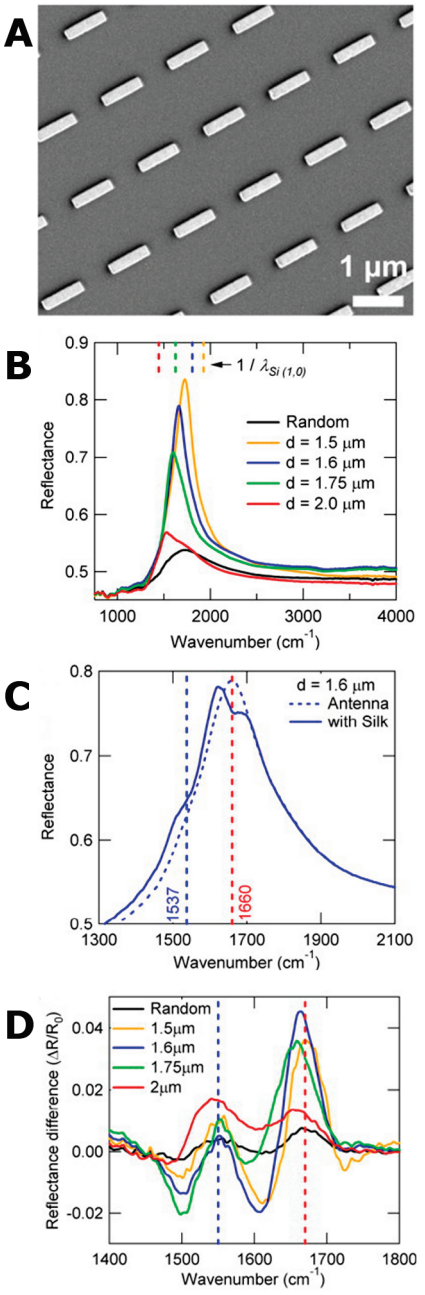

Figure 37. (A) Scanning electron microscope (SEM) images of a periodic array. (B) Reflectance spectra of periodic nanoantenna arrays. All of the antennas are 1100 nm long. The wavenumbers corresponding to $1/\lambda$ Si (1, 0) for a given periodicity are indicated by the dashed lines at the top of the figure. (C) Reflectance spectra from the 1.6 μm periodic array before (dashed line) and after coating of 2 nm thick protein film (solid line). Dashed vertical lines indicate the positions of the protein amide I and II absorption peaks. (D) Difference absorption spectra of the arrays whose spectral characteristics before protein coating are given in panel B.[506] Reprinted with kind permission from ref 506. Copyright 2009 National Academy of Sciences, U.S.A.

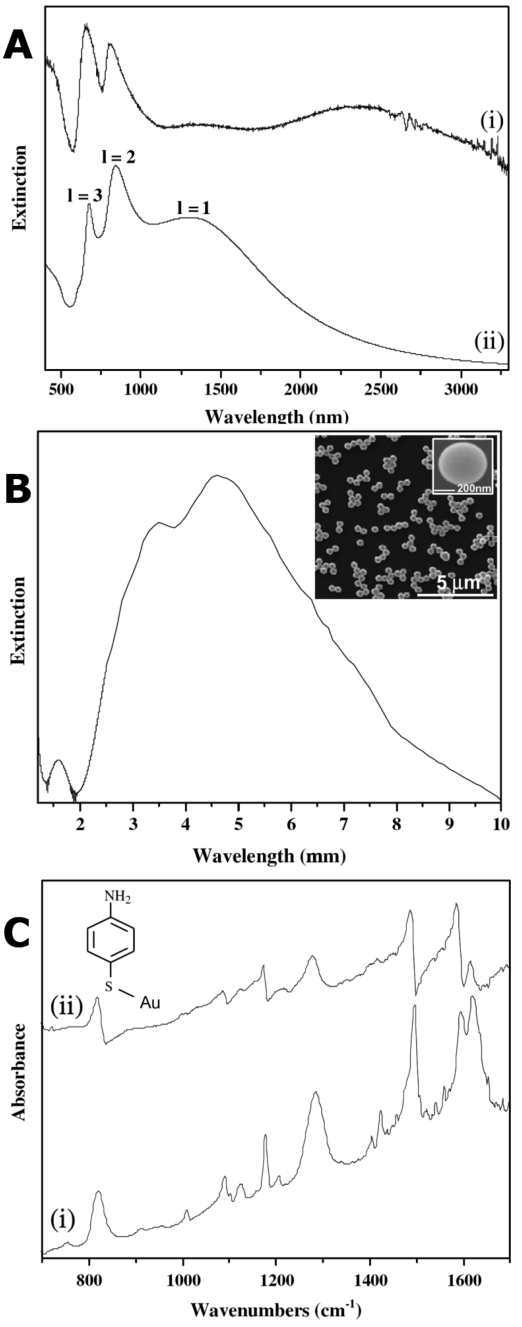

Figure 38. Aggregated nanoshell SEIRA. (A) Extinction spectrum on glass: (i) experimental spectrum; (ii) calculated spectrum. (B) Extinction spectrum on silicon spanning the near to mid-IR range. (inset) SEM image of aggregated nanoshells on silicon substrate. (C) (i) Normal IR absorption of pMA and (ii) SEIRA spectrum of pMA.[510] Reprinted with kind permission from ref 510. Copyright 2008 Elsevier.

collective excitation of the array providing large enhancements in the IR region. Adato et al. have called the combined effect "collectively enhanced IR absorption" or CEIRA. The collective enhancement due to both effects can easily reach 10^4-10^5, enough to achieve zeptomolar detection limits or ~145 molecules per nanowire. The gold nanoantenna arrays were fabricated by a masking and liftoff technique. Figure 37A is an SEM image of the nanoantenna array, and Figure 37B is a reflectance spectrum of the arrays of 1100 nm length and different periodicities. As compared with the sample with randomly arranged antennas the ordered arrays with varying spacing show enhanced reflectances and narrower line widths. To assess the SEIRA enhancement of the arrays, 2 nm thick silk protein

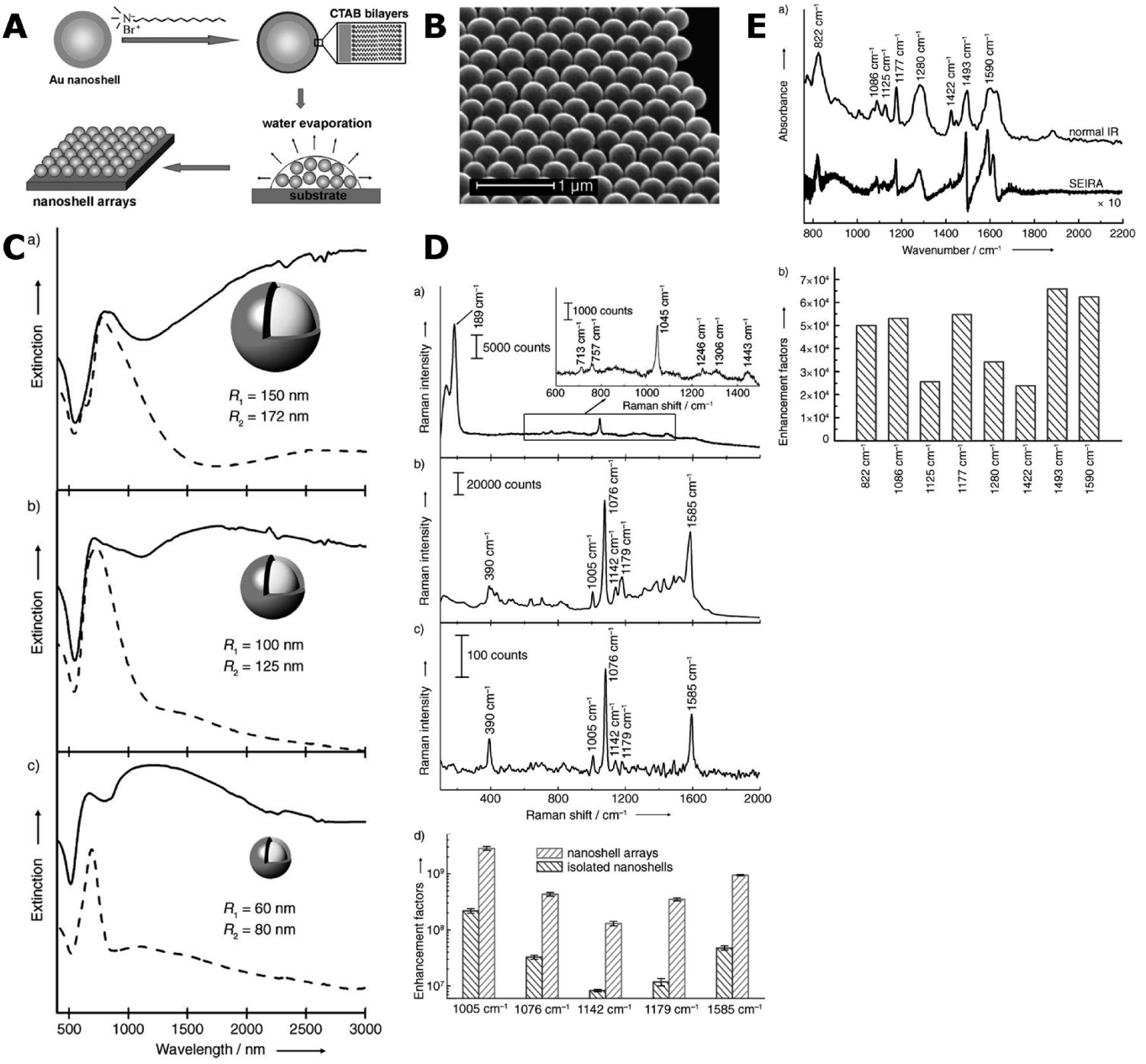

Figure 39. (A) Fabrication of Au nanoshell arrays. (B) SEM images of nanoshell arrays formed by drying 40 mL of aqueous solutions of CTAB-capped Au nanoshells on silicon wafers. (C) Normal-incidence extinction spectra of monolayer nanoshell arrays (solid curves) and submonolayers of isolated nanoshells (dashed curved) supported on glass slides. (D) SERS performance of the nanoshell arrays. SERS spectrum of (a) CTAB and (b) pMA on nanoshell monolayer arrays. (c) SERS spectrum of pMA on the isolated nanoshells. The coverage of the submonolayer of isolated nanoshells was determined to be 212 ± 15 particles in each beam spot according to the SEM images. (d) Empirical SERS enhancement factors of pMA adsorbed on nanoshell arrays and the isolated nanoshells. (E) SEIRA performance of the nanoshell arrays. (a) Normal IR spectrum of pure pMA and SEIRA spectrum of pMA SAMs on the nanoshell arrays. (b) SEIRA enhancement factors of different IR modes calculated on the basis of the experimental spectra.[511] Reprinted with kind permission from ref 511. Copyright 2007 Wiley-VCH Verlag GmbH&Co. KGaA.

films were deposited on the arrays. Silk protein was the protein of choice because of its ability to form uniform layers with excellent thickness control, and the protein backbone provided a model system for IR absorption measurements.[509] Figure 37C shows the reflectance spectrum before and after the silk film is applied. The dashed lines in the graph show the position of the amide I and amide II absorption peaks that define protein structures. The SEIRA spectra from the various films in panel B are shown in Figure 37D. The spectra correspond to the difference in reflectance and clearly show the enhanced amide I and amide II absorption peaks. In addition, the variations in the absorption line shape and intensity as the spectral overlap between the antenna resonance and the amide absorption changes can be observed.

While aggregated gold and silver nanoparticles provide hot spots where molecules trapped in the hot spot show large SERS

dx.doi.org/10.1021/cr200061k |*Chem. Rev.* 2011, 111, 3913–3961

enhancement, the aggregated colloid plasmon does not reach far into the infrared regime to access SEIRA modes. Kundu et al. have demonstrated the use of aggregated nanoshells as efficient SEIRA substrates.[510] Nanoshells have tunable plasmons that can be positioned in the infrared, and in analogy with aggregated colloid hot spots for SERS, aggregated nanoshells provide a broad infrared band that can provide enhancement for SEIRA (Figure 38A).

Nanoshells with $[r_1, r_2] = [190, 210]$ nm were fabricated using a standard nanoshell synthesis protocol.[483−484] The nanoshell solution was dropped dried onto silicon wafer pieces, and the nanoshells formed small aggregate clusters as can be seen in the SEM micrograph in the inset to Figure 38B. The silicon substrate further red shifts the plasmon resonance of the nanoshell aggregates. Next the nanoshells were incubated in a 1 mM ethanolic solution of *para*-mercaptoaniline (pMA). SEIRA spectra were collected using a FT-IR spectrometer with a liquid N_2 cooled MCT detector. Figure 38C compares the bulk IR spectrum and the SEIRA spectrum of pMA. Most of the peaks observed in the bulk spectrum are enhanced in the SEIRA spectrum. The SEIRA enhancement factor from these aggregated nanoshell films was estimated to be $\sim(1-4) \times 10^4$. This is one of the best reported SEIRA enhancement factors.

Hot spots formed in the junctions of nanoshells provide sufficient enhancement for SEIRA. Individual nanoshells with a plasmon resonance in the near-infrared regime can be optimized as substrates for SERS. Combining the two concepts, Wang et al. have designed a unique 2D nanoshell array substrate with <10 nm gaps that simultaneously enhances both SERS and SEIRA spectroscopies.[511] To form the arrays, nanoshells were dialyzed and functionalized with the surfactant cetyltrimethyl ammonium bromide (CTAB). Small drops of an aqueous solution of these functionalized nanoshells were applied to clean substrates and allowed to dry under ambient conditions. The nanoshells dry and form hexagonal close packed arrays (Figure 39A,B). The presence of the CTAB maintains a ~10 nm gap between adjacent nanoshells. The physical reasons for the electromagnetic enhancements of SERS and SEIRA in this structure are different: the SERS enhancements occur through resonant enhancement of the quadrupolar plasmon, due to the nanolens effect, while the SEIRA enhancements are due to the lightning rod effect.[458]

The extinction spectra of 2D arrays formed with three different sized nanoshells are shown in Figure 39C. Each array shows a resonance peak in two different spectral regions: A peak in the visible to near-infrared and a broad resonance covering the infrared regime. The arrays were evaluated as SERS−SEIRA substrates by adsorbing pMA on the arrays. The pMA effectively displaces the CTAB and forms a self-assembled monolayer (SAM) on the substrate. Figure 39D shows the SERS spectrum of the as-prepared array and the peaks associated with the CTAB modes. After the pMA adsorption, SAMs are formed on the arrays, the SERS spectrum is completely dominated by peaks arising from pMA modes, and none of the CTAB modes remain visible. The pMA SERS spectrum is highly reproducible on different parts of the substrate with a standard deviation of less than 10%. The SERS spectrum from a submonolayer film of isolated nanoshells with pMA is included for comparison. Signal enhancement factors were determined by comparing the ratio of the intensity of the SERS mode to the Raman intensity from unenhanced neat pMA films. The enhancement factor calculation also normalizes for the number of pMA molecules probed. The enhancement factors are estimated to be 10^8-10^9 and are 10−20 times larger than those achieved for isolated nanoshells. This represents the enhancement due to the array and is high enough to approach zeptomolar molecular detection limits.

The broad plasmon of the nanoshell arrays in the mid-IR region is used to enhance the IR absorption in this region. Figure 39E shows the IR absorption spectrum of neat pMA on a silicon substrate along with the SEIRA spectra of pMA measured on a nanoshell array. A high-quality SEIRA spectrum across much of the IR fingerprinting region with several of the characteristic vibrational modes enhanced can be observed. The SEIRA enhancement factors were determined in the same fashion as the SERS enhancement factor by comparing the ratio of the SEIRA modes to the unenhanced IR modes from neat pMA films. The SEIRA enhancement factors were determined to be on the order of 10^4. No SEIRA signals were observed from isolated nanoshell films.

This multifunctional array integrates complementary vibrational spectroscopies onto the same substrate and should enable better identification of unknown molecules and detailed investigation of molecular structure, orientation, and conformation.

7. CONCLUSIONS AND OUTLOOK

The topic of interacting plasmons has grown in scientific and technological importance from an interesting property of colloidal chemistry to a way to control electromagnetic radiation at the nanoscale, producing practical applications for chemical assays and nanoscale biological research. From the first theoretical analyses of the coupling between two metallic nanospheres to our advanced numerical modeling of complex structures, our abilities to understand the properties of coupled plasmonic systems have grown substantially. Experimental observations of nanoparticle clusters and their characteristic "hot spots" has driven interest in this area to achieve single-molecule sensitivity in chemical sensing and to achieve sufficient understanding of this effect to predictively design plasmonic structures with these properties. As a result of these efforts, a theoretical foundation that provides simple, intuitive physical insight into coupled plasmonic systems has emerged, based on the analogy of these systems with the hybridized wave functions of molecular orbital theory. The plasmon hybridization picture has led to the synthesis and fabrication of new nanostructures incorporating nanoparticle−film interactions and chains of plasmonic nanostructures for the propagation of plasmons along confined geometries. Strongly coupled plasmon systems also extend beyond classical electrodynamics, entering regimes where quantum mechanical processes such as tunneling can begin to dominate the physical properties of specific structures. As our understanding of quantum plasmonics advances, new media with strongly coupled plasmon−exciton mixed states are likely to emerge, with new and unique properties. Complex systems of coupled plasmons support a range of coherence effects, such as Fano resonances, which can be used to modify the properties of plasmonic media. While the past decade has seen a tremendous advance in our fundamental understanding of coupled plasmonic systems, with our increased understanding of these systems and expanded experimental capabilities, we anticipate even greater advances in this field.

AUTHOR INFORMATION

Corresponding Author
*E-mail: nordland@rice.edu.

BIOGRAPHIES

Naomi Halas is the Stanley C. Moore Professor of Electrical and Computer Engineering at Rice University, where she also holds faculty appointments in the Departments of Physics and Astronomy, Chemistry, and Bioengineering. Halas pursues fundamental studies of coupled plasmonic systems, investigating how they give rise to new nanoscale optical properties and effects. She is a Member of the American Academy of Arts and Sciences and a Fellow of the American Physical Society, the Optical Society of America, the International Society for Optical Engineering (SPIE), the Institute for Electrical and Electronics Engineers, and the American Association for the Advancement of Science. She is a Visiting Professor at the Institute of Physics, Chinese Academy of Sciences, and an Associate Editor of *Nano Letters*.

Surbhi Lal is a postdoctoral research associate in the Department of Electrical and Computer Engineering at Rice University in Houston, TX, working with Professor Naomi Halas. She is also the executive director of the Laboratory for Nanophotonics (LANP) at Rice University. She received her Ph.D. in 2006 from Rice University under the supervision of Professor Naomi Halas. Her current research interests are in nano-optics and surface-enhanced spectroscopy.

Wei-Shun Chang is a postdoctoral research associate working with Professor Stephan Link in the Department of Chemistry at Rice University in Houston, Texas. He received his Ph.D. from the University of Texas at Austin in 2007 under the supervision of Professor Paul F. Barbara. His current research is mainly focused on exploring radiative and nonradiative properties of strongly coupled plasmons in nanoparticle assemblies using single-nanoparticle spectroscopy.

Stephan Link is Assistant Professor of Chemistry and of Electrical and Computer Engineering at Rice University in Houston. He received his Ph.D. in chemistry in 2000 from the Georgia Institute of Technology where he worked for Professor Mostafa A. El-Sayed. In 2006, he joined the Rice Chemistry Department after postdoctoral positions at Georgia Tech and the University of Texas at Austin, where he worked for Professor Paul F. Barbara. His main research interests include the optical properties of single and assembled metallic nanoparticles and the diffusion and alignment of anisotropic nanostructures.

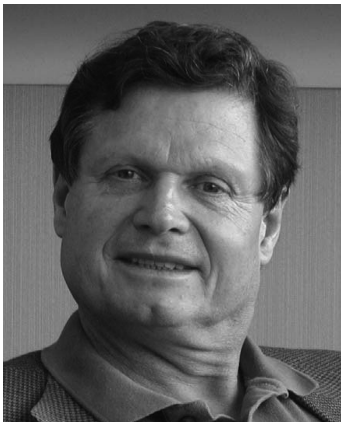

Peter Nordlander is Professor of Physics and Astronomy and of Electrical and Computer Engineering at Rice University in Houston. He received his Ph.D. in theoretical physics in 1985 from Chalmers University in Gothenburg, Sweden. He joined the Rice Physics department in 1989 after postdoctoral and visiting positions at IBM Thomas J Watson Research Center, AT&T Bell Laboratories, and Rutgers University. His main research interests concern the electronic and optical properties of metallic nanostructures and electron transport and relaxation dynamics in mesoscopic structures. He is a Fellow of the American Physical Society, the International Society for Optical Engineering (SPIE), and the American Association for the Advancement of Science (AAAS). He is an Associate Editor of *ACS Nano* and a Visiting Professor at the Institute of Physics, Chinese Academy of Sciences.

ACKNOWLEDGMENT

We acknowledge and thank Mark Knight for the TOC artwork and assistance with the review. This work was supported by the Robert A. Welch Foundation under Grants C-1220 (N.J.H.), C-1222 (P.N.), and C-1664 (S.L.). This work was supported by the Center for Advanced Solar Photophysics, an Energy Frontier Research Center funded by the U.S. DoE, Office of Basic Energy Sciences (Grant 78506-001-09), the Air Force Office of Scientific Research (Grant FA9550-10-1-0469), the Office of Naval Research (Grant N00014-10-1-0989), and the DoD National Security Science and Engineering Faculty Fellowship (Grant N00244-09-1-0067). S.L. acknowledges support from NSF (Grant CHE-0955286) and the American Chemical Society Petroleum Research Fund (Grant 50191-DNI6).

REFERENCES

(1) Mie, G. *Ann. Phys.* **1908**, *25*, 377.
(2) Kreibig, U.; Vollmer, M. *Optical Properties of Metal Clusters*; Springer: New York, 1995.
(3) Bohren, C. F.; Huffman, D. R. *Absorption and Scattering of Light by Small Particles*; John Wiley and Sons, Inc.: New York, 1983.
(4) Maier, S. A. *Plasmonics: Fundamentals and Applications*; Springer: New York, 2007.
(5) Dusemund, B.; Hoffmann, A.; Salzmann, T.; Kreibig, U.; Schmid, G. *Z. Phys. D: At., Mol. Clusters* **1991**, *20*, 305.
(6) Aravind, P. K.; Nitzan, A.; Metiu, H. *Surf. Sci.* **1981**, *110*, 189.
(7) Quinten, M.; Kreibig, U.; Schonauer, D.; Genzel, L. *Surf. Sci.* **1985**, *156*, 741.
(8) Quinten, M.; Kreibig, U. *Surf. Sci.* **1986**, *172*, 557.
(9) Elghanian, R.; Storhoff, J. J.; Mucic, R. C.; Letsinger, R. L.; Mirkin, C. A. *Science* **1997**, *277*, 1078.
(10) Mirkin, C. A.; Letsinger, R. L.; Mucic, R. C.; Storhoff, J. J. *Nature* **1996**, *382*, 607.
(11) Radwan, S. H.; Azzazy, H. M. E. *Expert Rev. Mol. Diagn.* **2009**, *9*, 511.
(12) Wang, Z. X.; Ma, L. N. *Coord. Chem. Rev.* **2009**, *253*, 1607.
(13) Sau, T. K.; Rogach, A. L. *Adv. Mater.* **2010**, *22*, 1781.
(14) Sau, T. K.; Rogach, A. L.; Jackel, F.; Klar, T. A.; Feldmann, J. *Adv. Mater.* **2010**, *22*, 1805.
(15) Giannini, V.; Fernandez-Dominguez, A. I.; Sonnefraud, Y.; Roschuk, T.; Fernandez-Garcia, R.; Maier, S. A. *Small* **2010**, *6*, 2498.
(16) Jeanmaire, D. L.; Vanduyne, R. P. *J. Electroanal. Chem.* **1977**, *84*, 1.
(17) Moskovits, M. *Rev. Mod. Phys.* **1985**, *57*, 783.
(18) Kneipp, K.; Wang, Y.; Kneipp, H.; Perelman, L. T.; Itzkan, I.; Dasari, R.; Feld, M. S. *Phys. Rev. Lett.* **1997**, *78*, 1667.
(19) Nie, S. M.; Emery, S. R. *Science* **1997**, *275*, 1102.
(20) Michaels, A. M.; Nirmal, M.; Brus, L. E. *J. Am. Chem. Soc.* **1999**, *121*, 9932.
(21) Xu, H.; Bjerneld, E. J.; Käll, M.; Börjesson, L. *Phys. Rev. Lett.* **1999**, *83*, 4357.
(22) Michaels, A. M.; Jiang, J.; Brus, L. *J. Phys. Chem. B* **2000**, *104*, 11965.
(23) Kneipp, K.; Kneipp, H.; Manoharan, R.; Hanlon, E. B.; Itzkan, I.; Dasari, R. R.; Feld, M. S. *Appl. Spectrosc.* **1998**, *52*, 1493.
(24) Kneipp, K.; Kneipp, H.; Kneipp, J. *Acc. Chem. Res.* **2006**, *39*, 443.
(25) Gresillon, S.; Aigouy, L.; Boccara, A. C.; Rivoal, J. C.; Quelin, X.; Desmarest, C.; Gadenne, P.; Shubin, V. A.; Sarychev, A. K.; Shalaev, V. M. *Phys. Rev. Lett.* **1999**, *82*, 4520.
(26) Talley, C. E.; Jackson, J. B.; Oubre, C.; Grady, N. K.; Hollars, C. W.; Lane, S. M.; Huser, T. R.; Nordlander, P.; Halas, N. J. *Nano Lett.* **2005**, *5*, 1569.
(27) Lu, J. Y.; Chao, H. Y.; Wu, J. C.; Wei, S. Y.; Chang, Y. H.; Chen, S. C. *Phys. E (Amsterdam, Neth.)* **2010**, *42*, 2583.
(28) Lee, S. Y.; Hung, L.; Lang, G. S.; Cornett, J. E.; Mayergoyz, I. D.; Rabin, O. *ACS Nano* **2010**, *4*, 5763.
(29) Encina, E. R.; Coronado, E. A. *J. Phys. Chem. C* **2010**, *114*, 16278.
(30) Yun, B. F.; Wang, Z. Y.; Hu, G. H.; Cui, Y. P. *Opt. Commun.* **2010**, *283*, 2947.
(31) Huang, J. S.; Kern, J.; Geisler, P.; Weinmann, P.; Kamp, M.; Forchel, A.; Biagioni, P.; Hecht, B. *Nano Lett.* **2010**, *10*, 2105.
(32) Alu, A.; Engheta, N. *Phys. Rev. Lett.* **2010**, *104*, No. 213902.
(33) Lu, J. Y.; Chang, Y. H. *Opt. Commun.* **2010**, *283*, 2627.
(34) Maher, R. C.; Maier, S. A.; Cohen, L. F.; Koh, L.; Laromaine, A.; Dick, J. A. G.; Stevens, M. M. *J. Phys. Chem. C* **2010**, *114*, 7231.
(35) Rycenga, M.; Camargo, P. H. C.; Li, W. Y.; Moran, C. H.; Xia, Y. *J. Phys. Chem. Lett.* **2010**, *1*, 696.
(36) Jain, P. K.; El-Sayed, M. A. *Chem. Phys. Lett.* **2010**, *487*, 153.
(37) Chau, Y. F. *Plasmonics* **2009**, *4*, 253.
(38) Wu, D. J.; Cheng, Y.; Liu, X. J. *Appl. Phys. B* **2009**, *97*, 497.
(39) Hou, Y. M.; Xu, J.; Wang, P. W.; Yu, D. P. *Appl. Phys. Lett.* **2010**, *96*, No. 203107.
(40) Encina, E. R.; Coronado, E. A. *J. Phys. Chem. C* **2010**, *114*, 3918.
(41) Ward, D. R.; Grady, N. K.; Levin, C. S.; Halas, N. J.; Wu, Y. P.; Nordlander, P.; Natelson, D. *Nano Lett.* **2007**, *7*, 1396.
(42) Ward, D. R.; Halas, N. J.; Ciszek, J. W.; Tour, J. M.; Wu, Y.; Nordlander, P.; Natelson, D. *Nano Lett.* **2008**, *8*, 919.
(43) Pernice, W. H. P. *J. Comput. Theor. Nanosci.* **2010**, *7*, 1.
(44) Chremmos, I. *J. Opt. Soc. Am. A* **2009**, *26*, 2623.
(45) Khoury, C. G.; Norton, S. J.; Vo-Dinh, T. *ACS Nano* **2009**, *3*, 2776.
(46) Teperik, T. V.; Borisov, A. G. *Phys. Rev. B* **2009**, *79*, 245409.
(47) Chau, Y. F.; Chen, M. W.; Tsai, D. P. *Appl. Opt.* **2009**, *48*, 617.
(48) Montgomery, J. M.; Lee, T. W.; Gray, S. K. *J. Phys.: Condens. Matter* **2008**.
(49) Mohammadi, A.; Jalali, T.; Agio, M. *Opt. Express* **2008**, *16*, 7397.
(50) Prodan, E.; Radloff, C.; Halas, N. J.; Nordlander, P. *Science* **2003**, *302*, 419.
(51) Liu, H.; Liu, Y. M.; Li, T.; Wang, S. M.; Zhu, S. N.; Zhang, X. *Phys. Status Solidi B* **2009**, *246*, 1397.
(52) Liu, N.; Liu, H.; Zhu, S. N.; Giessen, H. *Nat. Photonics* **2009**, *3*, 157.
(53) Kim, S. J.; Jang, D. J. *Mater. Lett.* **2008**, *62*, 4500.
(54) Moradi, A. *Opt. Commun.* **2009**, *282*, 3368.
(55) Yuan, Z.; Gao, S. W. *Phys. Rev. B* **2006**, *73*, No. 155411.
(56) Yang, Z. J.; Zhang, Z. S.; Zhang, W.; Hao, Z. H.; Wang, Q. Q. *Appl. Phys. Lett.* **2010**, *96*, No. 131113.
(57) Yang, S. C.; Kobori, H.; He, C. L.; Lin, M. H.; Chen, H. Y.; Li, C. C.; Kanehara, M.; Teranishi, T.; Gwo, S. *Nano Lett.* **2010**, *10*, 632.
(58) Funston, A. M.; Novo, C.; Davis, T. J.; Mulvaney, P. *Nano Lett.* **2009**, *9*, 1651.
(59) Hu, Y.; Noelck, S. J.; Drezek, R. A. *ACS Nano* **2010**, *4*, 1521.

(60) Wu, D. J.; Liu, X. J. *Appl. Phys. B* **2009**, *97*, 193.
(61) Ye, J.; Lagae, L.; Maes, G.; Borghs, G.; Van Dorpe, P. *Opt. Express* **2009**, *17*, 23765.
(62) Ye, J.; Verellen, N.; Van Roy, W.; Lagae, L.; Maes, G.; Borghs, G.; Van Dorpe, P. *ACS Nano* **2010**, *4*, 1457.
(63) Turner, M. D.; Hossain, M. M.; Gu, M. *New J. Phys.* **2010**, *12*, No. 083062.
(64) Davis, T. J.; Gomez, D. E.; Vernon, K. C. *Nano Lett.* **2010**, *10*, 2618.
(65) Liu, N.; Guo, H. C.; Fu, L. W.; Kaiser, S.; Schweizer, H.; Giessen, H. *Adv. Mater.* **2007**, *19*, 3628.
(66) Guo, H. C.; Liu, N.; Fu, L. W.; Meyrath, T. P.; Zentgraf, T.; Schweizer, H.; Giessen, H. *Opt. Express* **2007**, *15*, 12095.
(67) Liu, H.; Genov, D. A.; Wu, D. M.; Liu, Y. M.; Liu, Z. W.; Sun, C.; Zhu, S. N.; Zhang, X. *Phys. Rev. B* **2007**, *76*, No. 073101.
(68) Sheikholeslami, S.; Jun, Y. W.; Jain, P. K.; Alivisatos, A. P. *Nano Lett.* **2010**, *10*, 2655.
(69) Choi, C. L.; Alivisatos, A. P. *Annu. Rev. Phys. Chem.* **2010**, *61*, 369.
(70) Liu, S. D.; Cheng, M. T. *J. Appl. Phys.* **2010**, *108*, 034313.
(71) Hallock, A. J.; Redmond, P. L.; Brus, L. E. *Proc. Natl. Acad. Sci. U.S.A.* **2005**, *102*, 1280.
(72) Jain, P. K.; El-Sayed, M. A. *Nano Lett.* **2007**, *7*, 2854.
(73) Rechberger, W.; Hohenau, A.; Leitner, A.; Krenn, J. R.; Lamprecht, B.; Aussenegg, F. R. *Opt. Commun.* **2003**, *220*, 137.
(74) Gunnarsson, L.; Rindzevicius, T.; Prikulis, J.; Kasemo, B.; Käll, M.; Zou, S. L.; Schatz, G. C. *J. Phys. Chem. B* **2005**, *109*, 1079.
(75) Park, T. H.; Nordlander, P. *Chem. Phys. Lett.* **2009**, *472*, 228.
(76) Duraiswamy, S.; Khan, S. A. *Nano Lett.* **2010**, *10*, 3757.
(77) Wu, D. J.; Liu, X. J. *Appl. Phys. Lett.* **2010**, *97*, No. 061904.
(78) Norris, C. B.; Joseph, P. R.; Mackiewicz, M. R.; Reed, S. M. *Chem. Mater.* **2010**, *22*, 3637.
(79) Mahmoud, M. A.; Snyder, B.; El-Sayed, M. A. *J. Phys. Chem. C* **2010**, *114*, 7436.
(80) Preston, T. C.; Signorell, R. *ACS Nano* **2009**, *3*, 3696.
(81) Bardhan, R.; Mukherjee, S.; Mirin, N. A.; Levit, S. D.; Nordlander, P.; Halas, N. J. *J. Phys. Chem. C* **2010**, *114*, 7378.
(82) Mukherjee, S.; Sobhani, H.; Lassiter, J. B.; Bardhan, R.; Nordlander, P.; Halas, N. J. *Nano Lett.* **2010**, *10*, 2694.
(83) Radloff, C.; Halas, N. J. *Nano Lett.* **2004**, *4*, 1323.
(84) Willingham, B.; Brandl, D. W.; Nordlander, P. *Appl. Phys. B* **2008**, *93*, 209.
(85) Hao, F.; Nehl, C. L.; Hafner, J. H.; Nordlander, P. *Nano Lett.* **2007**, *7*, 729.
(86) Dolling, G.; Enkrich, C.; Wegener, M.; Zhou, J. F.; Soukoulis, C. M. *Opt. Lett.* **2005**, *30*, 3198.
(87) Cai, W. S.; Chettiar, U. K.; Yuan, H. K.; de Silva, V. C.; Kildishev, A. V.; Drachev, V. P.; Shalaev, V. M. *Opt. Express* **2007**, *15*, 3333.
(88) Shvets, G.; Urzhumov, Y. A. *J. Opt. A: Pure Appl. Opt.* **2006**, *8*, S122.
(89) Yuan, H. K.; Chettiar, U. K.; Cai, W. S.; Kildishev, A. V.; Boltasseva, A.; Drachev, V. P.; Shalaev, V. M. *Opt. Express* **2007**, *15*, 1076.
(90) Liu, N.; Giessen, H. *Angew. Chem., Int. Ed.* **2010**, *49*, 9838.
(91) Chen, S. Y.; Mock, J. J.; Hill, R. T.; Chilkoti, A.; Smith, D. R.; Lazarides, A. A. *ACS Nano* **2010**, *4*, 6535.
(92) Ye, J. A.; Shioi, M.; Lodewijks, K.; Lagae, L.; Kawamura, T.; Van Dorpe, P. *Appl. Phys. Lett.* **2010**, *97*, No. 163106.
(93) Hill, R. T.; Mock, J. J.; Urzhumov, Y.; Sebba, D. S.; Oldenburg, S. J.; Chen, S. Y.; Lazarides, A. A.; Chilkoti, A.; Smith, D. R. *Nano Lett.* **2010**, *10*, 4150.
(94) Park, W. H.; Kim, Z. H. *Nano Lett.* **2010**, *10*, 4040.
(95) Farcau, C.; Astilean, S. *J. Phys. Chem. C* **2010**, *114*, 11717.
(96) Vernon, K. C.; Funston, A. M.; Novo, C.; Gomez, D. E.; Mulvaney, P.; Davis, T. J. *Nano Lett.* **2010**, *10*, 2080.
(97) Hu, M.; Ghoshal, A.; Marquez, M.; Kik, P. G. *J. Phys. Chem. C* **2010**, *114*, 7509.
(98) Kang, T.; Yoo, S. M.; Yoon, I.; Lee, S. Y.; Kim, B. *Nano Lett.* **2010**, *10*, 1189.
(99) Li, H. J.; Fu, S. L.; Xie, S. X.; Xu, H. Q.; Zhou, X.; Wu, J. J. *Sci. China, Ser. G: Phys., Mech. Astron.* **2010**, *53*, 38.
(100) Kang, T.; Yoon, I.; Kim, J.; Hee, H.; Kim, B. *Chem.—Eur. J.* **2010**, *16*, 1351.
(101) Amarie, D.; Alileche, A.; Dragnea, B.; Glazier, J. A. *Anal. Chem.* **2010**, *82*, 343.
(102) Sukharev, M.; Seideman, T. *J. Phys. Chem. A* **2009**, *113*, 7508.
(103) Park, W. H.; Ahn, S. H.; Kim, Z. H. *ChemPhysChem* **2008**, *9*, 2491.
(104) Lévêque, G.; Martin, O. J. F. *Opt. Express* **2006**, *14*, 9971.
(105) (a) Knight, M. W.; Wu, Y. P.; Lassiter, J. B.; Nordlander, P.; Halas, N. J. *Nano Lett.* **2009**, *9*, 2188. (b) Wu, Y. P.; Nordlander, P. *J. Phys. Chem. C* **2010**, *114*, 7302.
(106) Aravind, P. K.; Metiu, H. *Surf. Sci.* **1983**, *124*, 506.
(107) Wind, M. M.; Vlieger, J.; Bedeaux, D. *Phys. A* **1987**, *141*, 33.
(108) Ruppin, R. *Phys. Rev. B* **1992**, *45*, 11209.
(109) Gozhenko, V. V.; Grechko, L. G.; Whites, K. W. *Phys. Rev. B* **2003**, *68*, No. 125422.
(110) (a) Futamata, M.; Maruyama, Y.; Ishikawa, M. *J. Phys. Chem. B* **2003**, *107*, 7607. (b) Larkin, I. A.; Stockman, M. I.; Achermann, M.; Klimov, V. I. *Phys. Rev. B* **2004**, *69*, No. 121403.
(111) Nordlander, P.; Prodan, E. *Nano Lett.* **2004**, *4*, 2209.
(112) Nordlander, P.; Oubre, C.; Prodan, E.; Li, K.; Stockman, M. I. *Nano Lett.* **2004**, *4*, 899.
(113) Knight, M. W.; Grady, N. K.; Bardhan, R.; Hao, F.; Nordlander, P.; Halas, N. J. *Nano Lett.* **2007**, *7*, 2346.
(114) Hao, F.; Nordlander, P. *Appl. Phys. Lett.* **2006**, *89*, No. 103101.
(115) Le, F.; Lwin, N. Z.; Steele, J. M.; Käll, M.; Halas, N. J.; Nordlander, P. *Nano Lett.* **2005**, *5*, 2009.
(116) Fano, U. *Phys. Rev.* **1961**, *1*, 1866.
(117) Orendorff, C. J.; Gole, A.; Sau, T. K.; Murphy, C. J. *Anal. Chem.* **2005**, *77*, 3261.
(118) Kumar, G. V. P. *Appl. Opt.* **2010**, *49*, 6872.
(119) Teo, S. L.; Lin, V. K.; Marty, R.; Large, N.; Llado, E. A.; Arbouet, A.; Girard, C.; Aizpurua, J.; Tripathy, S.; Mlayah, A. *Opt. Express* **2010**, *18*, 22271.
(120) Fan, Z. Y.; Govorov, A. O. *Nano Lett.* **2010**, *10*, 2580.
(121) Lin, V. K.; Teo, S. L.; Marty, R.; Arbouet, A.; Girard, C.; Alarcon-Llado, E.; Liu, S. H.; Han, M. Y.; Tripathy, S.; Mlayah, A. *Nanotechnology* **2010**, *21*, No. 305501.
(122) Jin, R. C. *Angew. Chem., Int. Ed.* **2010**, *49*, 2826.
(123) Liu, Z. W.; Hung, W. H.; Aykol, M.; Valley, D.; Cronin, S. B. *Nanotechnology* **2010**, *21*, 105304.
(124) Camargo, P. H. C.; Au, L.; Rycenga, M.; Li, W. Y.; Xia, Y. N. *Chem. Phys. Lett.* **2010**, *484*, 304.
(125) Ghosh, S. K.; Pal, T. *Chem. Rev.* **2007**, *107*, 4797.
(126) Alivisatos, A. P.; Johnsson, K. P.; Peng, X. G.; Wilson, T. E.; Loweth, C. J.; Bruchez, M. P.; Schultz, P. G. *Nature* **1996**, *382*, 609.
(127) Loweth, C. J.; Caldwell, W. B.; Peng, X. G.; Alivisatos, A. P.; Schultz, P. G. *Angew. Chem., Int. Ed.* **1999**, *38*, 1808.
(128) Chen, J. H.; Seeman, N. C. *Nature* **1991**, *350*, 631.
(129) Zhang, Y. W.; Seeman, N. C. *J. Am. Chem. Soc.* **1994**, *116*, 1661.
(130) Yang, X. P.; Wenzler, L. A.; Qi, J.; Li, X. J.; Seeman, N. C. *J. Am. Chem. Soc.* **1998**, *120*, 9779.
(131) Seeman, N. C. *Nature* **2003**, *421*, 427.
(132) Shih, W. M.; Quispe, J. D.; Joyce, G. F. *Nature* **2004**, *427*, 618.
(133) Mastroianni, A. J.; Claridge, S. A.; Alivisatos, A. P. *J. Am. Chem. Soc.* **2009**, *131*, 8455.
(134) Urzhumov, Y. A.; Shvets, G.; Fan, J.; Capasso, F.; Brandl, D.; Nordlander, P. *Opt. Express* **2007**, *15*, 14129.
(135) Stadler, B.; Solak, H. H.; Frerker, S.; Bonroy, K.; Frederix, F.; Voros, J.; Grandin, H. M. *Nanotechnology* **2007**, *18*, No. 155306.
(136) Xia, Y. N.; Yin, Y. D.; Lu, Y.; McLellan, J. *Adv. Funct. Mater.* **2003**, *13*, 907.

(137) Cui, Y.; Bjork, M. T.; Liddle, A.; Soennichsen, C.; Bousser, B.; Alivisatos, A. P. *Nano Lett.* **2004**, *4*, 1093.
(138) Liu, S. T.; Maoz, R.; Sagiv, J. *Nano Lett.* **2004**, *4*, 845.
(139) Yan, B.; Thubagere, A.; Premasiri, W. R.; Ziegler, L. D.; Dal Negro, L.; Reinhard, B. M. *ACS Nano* **2009**, *3*, 1190.
(140) Alegret, J.; Rindzevicius, T.; Pakizeh, T.; Alaverdyan, Y.; Gunnarsson, L.; Käll, M. *J. Phys. Chem. C* **2008**, *112*, 14313.
(141) Brandl, D. W.; Mirin, N. A.; Nordlander, P. *J. Phys. Chem. B* **2006**, *110*, 12302.
(142) Shegai, T.; Li, Z. P.; Dadosh, T.; Zhang, Z. Y.; Xu, H. X.; Haran, G. *Proc. Natl. Acad. Sci. U.S.A.* **2008**, *105*, 16448.
(143) Xu, H. X.; Aizpurua, J.; Käll, M.; Apell, P. *Phys. Rev. E* **2000**, *62*, 4318.
(144) Oubre, C.; Nordlander, P. *J. Phys. Chem. B* **2005**, *109*, 10042.
(145) Olk, P.; Renger, J.; Wenzel, M. T.; Eng, L. M. *Nano Lett.* **2008**, *8*, 1174.
(146) Hao, E.; Schatz, G. C. *J. Chem. Phys.* **2004**, *120*, 357.
(147) Ruppin, R. *Phys. Rev. B* **1982**, *26*, 3440.
(148) Stender, A. S.; Wang, G. F.; Sun, W.; Fang, N. *ACS Nano* **2010**, *4*, 7667.
(149) Ming, T. A.; Zhao, L.; Xiao, M. D.; Wang, J. F. *Small* **2010**, *6*, 2514.
(150) Huang, C. P.; Yin, X. G.; Kong, L. B.; Zhu, Y. Y. *J. Phys. Chem. C* **2010**, *114*, 21123.
(151) Maaroof, A. I.; Sutherland, D. S. *J. Phys. D: Appl. Phys.* **2010**, *43*, No. 405301.
(152) Theiss, J.; Pavaskar, P.; Echternach, P. M.; Muller, R. E.; Cronin, S. B. *Nano Lett.* **2010**, *10*, 2749.
(153) Alvarez-Puebla, R.; Liz-Marzan, L. M.; de Abajo, F. J. G. *J. Phys. Chem. Lett.* **2010**, *1*, 2428.
(154) Guerrini, L.; Izquierdo-Lorenzo, I.; Rodriguez-Oliveros, R.; Sanchez-Gil, J. A.; Sanchez-Cortes, S.; Garcia-Ramos, J. V.; Domingo, C. *Plasmonics* **2010**, *5*, 273.
(155) Yang, L. L.; Wang, H. Y.; Yan, B.; Reinhard, B. M. *J. Phys. Chem. C* **2010**, *114*, 4901.
(156) Oh, M. K.; Park, S.; Kim, S. K.; Lim, S. H. *J. Comput. Theor. Nanosci.* **2010**, *7*, 1085.
(157) Mu, C.; Zhang, J. P.; Xu, D. S. *Nanotechnology* **2010**, *21* No. 015604.
(158) Baik, J. M.; Lee, S. J.; Moskovits, M. *Nano Lett.* **2009**, *9*, 672.
(159) Gu, G. H.; Suh, J. S. *Langmuir* **2008**, *24*, 8934.
(160) Danckwerts, M.; Novotny, L. *Phys. Rev. Lett.* **2007**, *98*, No. 026104.
(161) Fromm, D. P.; Sundaramurthy, A.; Schuck, P. J.; Kino, G.; Moerner, W. E. *Nano Lett.* **2004**, *4*, 957.
(162) Atay, T.; Song, J. H.; Nurmikko, A. V. *Nano Lett.* **2004**, *4*, 1627.
(163) Cui, X. D.; Erni, D. *J. Comput. Theor. Nanosci.* **2010**, *7*, 1610.
(164) Schmelzeisen, M.; Zhao, Y.; Klapper, M.; Mullen, K.; Kreiter, M. *ACS Nano* **2010**, *4*, 3309.
(165) Shao, L.; Woo, K. C.; Chen, H. J.; Jin, Z.; Wang, J. F.; Lin, H. Q. *ACS Nano* **2010**, *4*, 3053.
(166) Lu, J. Y.; Chang, Y. H. *Opt. Express* **2009**, *17*, 19451.
(167) Mitra, J.; Feng, L.; Boyle, M. G.; Dawson, P. *J. Phys. D: Appl. Phys.* **2009**, *42*, No. 215101.
(168) Kim, D. S.; Heo, J.; Ahn, S. H.; Han, S. W.; Yun, W. S.; Kim, Z. H. *Nano Lett.* **2009**, *9*, 3619.
(169) Pecharroman, C. *Phys. Chem. Chem. Phys.* **2009**, *11*, 5922.
(170) Boyle, M. G.; Mitra, J.; Dawson, P. *Appl. Phys. Lett.* **2009**, *94*, No. 233118.
(171) Marhaba, S.; Bachelier, G.; Bonnet, C.; Broyer, M.; Cottancin, E.; Grillet, N.; Lerme, J.; Vialle, J. L.; Pellarin, M. *J. Phys. Chem. C* **2009**, *113*, 4349.
(172) Harris, N.; Arnold, M. D.; Blaber, M. G.; Ford, M. J. *J. Phys. Chem. C* **2009**, *113*, 2784.
(173) Hartling, T.; Alaverdyan, Y.; Hille, A.; Wenzel, M. T.; Käll, M.; Eng, L. M. *Opt. Express* **2008**, *16*, 12362.
(174) Romero, I.; Aizpurua, J.; Bryant, G. W.; de Abajo, F. J. G. *Opt. Express* **2006**, *14*, 9988.
(175) Perez-Gonzalez, O.; Zabala, N.; Borisov, A. G.; Halas, N. J.; Nordlander, P.; Aizpurua, J. *Nano Lett.* **2010**, *10*, 3090.
(176) Lassiter, J. B.; Aizpurua, J.; Hernandez, L. I.; Brandl, D. W.; Romero, I.; Lal, S.; Hafner, J. H.; Nordlander, P.; Halas, N. J. *Nano Lett.* **2008**, *8*, 1212.
(177) Slaughter, L. S.; Wu, Y.; Willingham, B. A.; Nordlander, P.; Link, S. *ACS Nano* **2010**, *4*, 4657.
(178) Fernández-Domínguez, A. I.; Maier, S. A.; Pendry, J. B. *Phys. Rev. Lett.* **2010**, *105*, No. 266807.
(179) Lei, D. Y.; Aubry, A.; Maier, S. A.; Pendry, J. B. *New J. Phys.* **2010**, *12*, No. 093030.
(180) Aubry, A.; Lei, D. Y.; Fernandez-Dominguez, A. I.; Sonnefraud, Y.; Maier, S. A.; Pendry, J. B. *Nano Lett.* **2010**, *10*, 2574.
(181) Aubry, A.; Lei, D. Y.; Maier, S. A.; Pendry, J. B. *Phys. Rev. B* **2010**, *82*, No. 125430.
(182) Zhao, J.; Pinchuk, A. O.; McMahon, J. M.; Li, S.; Ausman, L. K.; Atkinson, A. L.; Schatz, G. C. *Acc. Chem. Res.* **2008**, *41*, 1710.
(183) de Abajo, F. J. G. *J. Phys. Chem. C* **2008**, *112*, 17983.
(184) McMahon, J. M.; Gray, S. K.; Schatz, G. C. *J. Phys. Chem. C* **2010**, *114*, 15903.
(185) Aizpurua, J.; Rivacoba, A. *Phys. Rev. B* **2008**, *78*, No. 035404.
(186) Chang, R. L.; Leung, P. T. *Phys. Rev. B* **2006**, *73*, No. 125438.
(187) Jensen, L. L.; Jensen, L. *J. Phys. Chem. C* **2009**, *113*, 15182.
(188) Morton, S. M.; Jensen, L. *J. Am. Chem. Soc.* **2009**, *131*, 4090.
(189) Zangwill, A.; Soven, P. *Phys. Rev. A* **1980**, *21*, 1561.
(190) Cottancin, E.; Lerme, J.; Gaudry, M.; Pellarin, M.; Vialle, J. L.; Broyer, M.; Prevel, B.; Treilleux, M.; Melinon, P. *Phys. Rev. B* **2000**, *62*, 5179.
(191) Rubio, A.; Serra, L. *Phys. Rev. B* **1993**, *48*, 18222.
(192) Lerme, J.; Palpant, B.; Cottancin, E.; Pellarin, M.; Prevel, B.; Vialle, J. L.; Broyer, M. *Phys. Rev. B* **1999**, *60*, 16151.
(193) Ekardt, W. *Phys. Rev. Lett.* **1984**, *52*, 1925.
(194) Jacak, W.; Krasnyj, J.; Jacak, J.; Chepok, A.; Jacak, L.; Donderowicz, W.; Hu, D. Z.; Schaadt, D. M. *J. Appl. Phys.* **2010**, *108*, No. 084304.
(195) Frey, K.; Idrobo, J. C.; Tiago, M. L.; Reboredo, F. A.; Ogut, S. *Phys. Rev. B* **2009**, *80*, No. 153411.
(196) Quijada, M.; Borisov, A. G.; Muino, R. D. *Phys. Status Solidi A* **2008**, *205*, 1312.
(197) Kulish, V. V.; Tomchuk, P. M. *Surf. Sci.* **2008**, *602*, 1045.
(198) Aikens, C. M.; Li, S. Z.; Schatz, G. C. *J. Phys. Chem. C* **2008**, *112*, 11272.
(199) Jensen, L.; Aikens, C. M.; Schatz, G. C. *Chem. Soc. Rev.* **2008**, *37*, 1061.
(200) Prodan, E.; Nordlander, P. *Nano Lett.* **2003**, *3*, 543.
(201) Prodan, E.; Nordlander, P.; Halas, N. J. *Chem. Phys. Lett.* **2003**, *368*, 94.
(202) Prodan, E.; Lee, A.; Nordlander, P. *Chem. Phys. Lett.* **2002**, *360*, 325.
(203) Prodan, E.; Nordlander, P.; Halas, N. J. *Nano Lett.* **2003**, *3*, 1411.
(204) Baer, R.; Neuhauser, D.; Weiss, S. *Nano Lett.* **2004**, *4*, 85.
(205) Gao, S. W.; Yan, Z. *Phys. Rev. B* **2005**, *72*, No. 121406.
(206) Johnson, H. E.; Aikens, C. A. *J. Phys. Chem. A* **2009**, *113*, 4445.
(207) Zuloaga, J.; Prodan, E.; Nordlander, P. *ACS Nano* **2010**, *4*, 5269.
(208) Troparevsky, M. C.; Zhao, K.; Xiao, D.; Eguiluz, A. G.; Zhang, Z. Y. *Phys. Rev. B* **2010**, *82*, No. 045413.
(209) Troparevsky, M. C.; Zhao, K.; Xiao, D.; Zhang, Z. Y.; Eguiluz, A. G. *Nano Lett.* **2009**, *9*, 4452.
(210) Yan, J.; Yuan, Z.; Gao, S. W. *Phys. Rev. Lett.* **2007**, *98*, No. 216602.
(211) Zuloaga, J.; Prodan, E.; Nordlander, P. *Nano Lett.* **2009**, *9*, 887.
(212) Mao, L.; Li, Z. P.; Wu, B.; Xu, H. X. *Appl. Phys. Lett.* **2009**, *94*, No. 243102.

(213) Song, P.; Nordlander, P.; Gao, S. W. *J. Chem. Phys.* **2011**, *134*, No. 074701.
(214) Nabika, H.; Takase, M.; Nagasawa, F.; Murakoshi, K. *J. Phys. Chem. Lett.* **2010**, *1*, 2470.
(215) Hyldgaard, P. *Phys. Rev. B* **2008**, *78*, No. 165109.
(216) de Abajo, F. J. G. *Rev. Mod. Phys.* **2010**, *82*, 209.
(217) Chen, X. D.; Yeganeh, S.; Qin, L. D.; Li, S. Z.; Xue, C.; Braunschweig, A. B.; Schatz, G. C.; Ratner, M. A.; Mirkin, C. A. *Nano Lett.* **2009**, *9*, 3974.
(218) Moody, B.; McCarty, G. S. *Appl. Phys. Lett.* **2009**, *94*, No. 122104.
(219) Ioffe, Z.; Shamai, T.; Ophir, A.; Noy, G.; Yutsis, I.; Kfir, K.; Cheshnovsky, O.; Selzer, Y. *Nat. Nanotechnol.* **2008**, *3*, 727.
(220) Neuhauser, D.; Lopata, K. *J. Chem. Phys.* **2007**, *127* No. 154715.
(221) Galperin, M.; Nitzan, A.; Ratner, M. A. *Phys. Rev. B* **2007**, *76*, No. 035301.
(222) Galperin, M.; Ratner, M. A.; Nitzan, A. *J. Phys.: Condens. Matter* **2007**, *19*, No. 103201.
(223) Schnell, M.; Garcia-Etxarri, A.; Huber, A. J.; Crozier, K.; Aizpurua, J.; Hillenbrand, R. *Nat. Photonics* **2009**, *3*, 287.
(224) Chau, Y. F.; Lin, Y. J.; Tsai, D. P. *Opt. Express* **2010**, *18*, 3510.
(225) Berthelot, J.; Bouhelier, A.; Huang, C. J.; Margueritat, J.; Colas-des-Francs, G.; Finot, E.; Weeber, J. C.; Dereux, A.; Kostcheev, S.; El Ahrach, H. I.; Baudrion, A. L.; Plain, J.; Bachelot, R.; Royer, P.; Wiederrecht, G. P. *Nano Lett.* **2009**, *9*, 3914.
(226) Large, N.; Abb, M.; Aizpurua, J.; Muskens, O. L. *Nano Lett.* **2010**, *10*, 1741.
(227) van der Molen, S. J.; Liao, J. H.; Kudernac, T.; Agustsson, J. S.; Bernard, L.; Calame, M.; van Wees, B. J.; Feringa, B. L.; Schonenberger, C. *Nano Lett.* **2009**, *9*, 76.
(228) Zheng, Y. B.; Yang, Y. W.; Jensen, L.; Fang, L.; Juluri, B. K.; Flood, A. H.; Weiss, P. S.; Stoddart, J. F.; Huang, T. J. *Nano Lett.* **2009**, *9*, 819.
(229) Fofang, N. T.; Park, T. H.; Neumann, O.; Mirin, N. A.; Nordlander, P.; Halas, N. J. *Nano Lett.* **2008**, *8*, 3481.
(230) Savasta, S.; Saija, R.; Ridolfo, A.; Stefano, O. D.; Denti, P.; Borghese, F. *ACS Nano* **2010**, *4*, 6369.
(231) Govorov, A. O.; Fan, Z.; Hernandez, P.; Slocik, J. M.; Naik, R. R. *Nano Lett.* **2010**, *10*, 1374.
(232) Noginov, M. A.; Zhu, G.; Belgrave, A. M.; Bakker, R.; Shalaev, V. M.; Narimanov, E. E.; Stout, S.; Herz, E.; Suteewong, T.; Wiesner, U. *Nature* **2009**, *460*, 1110.
(233) Cheng, M. T.; Luo, Y.-Q.; Song, Y.-Y.; Zhao, G. X. *J. Mod. Opt.* **2010**, *57*, 2177.
(234) Chung, H. Y.; Leung, P. T.; Tsai, D. P. *Plasmonics* **2010**, *5*, 363.
(235) Zhou, Z.-K.; Li, M.; Yang, Z.-J.; Peng, X.-N.; Su, X.-R.; Zhang, Z.-S.; Li, J.-B.; Kim, N.-C.; Yu, X.-F.; Zhou, L.; Hao, Z.-H.; Wang, Q.-Q. *ACS Nano* **2010**, *4*, 5003.
(236) Zhang, J.; Fu., Yi; Lakowicz, J. R. *J. Phys. Chem. C* **2009**, *113*, 19404.
(237) Zhang, H.; Li, Y.; Ivanov, I. A.; Qu, Y.; Huang, Y.; Duan, X. *Angew. Chem., Int. Ed.* **2010**, *49*, 2865.
(238) Neretina, S.; Dreaden, E. C.; Qian, W.; El-Sayed, M. A.; Hughes, R. A.; Preston, J. S.; Mascher, P. *Nano Lett.* **2009**, *9*, 3772.
(239) D'Agostino, S.; Sala, F. D. *ACS Nano* **2010**, *4*, 4117.
(240) Witlicki, E. H.; Andersen, S. S.; Hansen, S. W.; Jeppesen, J. O.; Wong, E. W.; Jensen, L.; Flood, A. H. *J. Am. Chem. Soc.* **2010**, *132*, 6099.
(241) Hung, W. H.; Aykol, M.; Valley, D.; Hou, W.; Cronin, S. B. *Nano Lett.* **2010**, *10*, 1314.
(242) Liaw, J.-W.; Chen, J.-H.; Chen, C.-S.; Kuo, M.-K. *Opt. Express* **2009**, *17*, 13532.
(243) Ausman, L. K.; Schatz, G. C. *J. Chem. Phys.* **2009**, *131* No. 084708.
(244) Vandenbem, C.; Brayer, D.; Froufe, P.; eacute; rez, L. S.; Carminati, R. *Phys. Rev. B* **2010**, *81*, No. 085444.
(245) Wei, H.; Ratchford, D.; Li, X. E.; Xu, H.; Shih, C.-K. *Nano Lett.* **2009**, *9*, 4168.
(246) Wei, H.; Li, Z.; Tian, X.; Wang, Z.; Cong, F.; Liu, N.; Zhang, S.; Nordlander, P.; Halas, N. J.; Xu, H. *Nano Lett.* **2011**, *11*, 471.
(247) Li, Z.; Zhang, S.; Halas, N. J.; Nordlander, P.; Xu, H. *Small* **2011**, *7*, 593.
(248) de Waele, R.; Koenderink, A. F.; Polman, A. *Nano Lett.* **2007**, *7*, 2004.
(249) Haynes, C. L.; McFarland, A. D.; Zhao, L.; Van Duyne, R. P.; Schatz, G. C.; Gunnarsson, L.; Prikulis, J.; Kasemo, B.; Käll, M. *J. Phys. Chem. B* **2003**, *107*, 7337.
(250) Hicks, E. M.; Zou, S.; Schatz, G. C.; Spears, K. G.; Van Duyne, R. P.; Gunnarsson, L.; Rindzevicius, T.; Kasemo, B.; Käll, M. *Nano Lett.* **2005**, *5*, 1065.
(251) Koenderink, A. F.; de Waele, R.; Prangsma, J. C.; Polman, A. *Phys. Rev. B* **2007**, *76*, 201403.
(252) Lamprecht, B.; Schider, G.; Lechner, R. T.; Ditlbacher, H.; Krenn, J. R.; Leitner, A.; Aussenegg, F. R. *Phys. Rev. Lett.* **2000**, *84*, 4721.
(253) Maier, S. A.; Kik, P. G.; Atwater, H. A. *Appl. Phys. Lett.* **2002**, *81*, 1714.
(254) Maier, S. A.; Kik, P. G.; Atwater, H. A.; Meltzer, S.; Harel, E.; Koel, B. E.; Requicha, A. A. G. *Nat. Mater.* **2003**, *2*, 229.
(255) Salerno, M.; Krenn, J. R.; Hohenau, A.; Ditlbacher, H.; Schider, G.; Leitner, A.; Aussenegg, F. R. *Opt. Commun.* **2005**, *248*, 543.
(256) Henzie, J.; Lee, M. H.; Odom, T. W. *Nat. Nanotech.* **2007**, *2*, 549.
(257) Wei, Q.-H.; Su, K.-H.; Durant, S.; Zhang, X. *Nano Lett.* **2004**, *4*, 1067.
(258) Sung, J.; Hicks, E. M.; Van Duyne, R. P.; Spears, K. G. *J. Phys. Chem. C* **2008**, *112*, 4091.
(259) Maier, S. A.; Kik, P. G.; Atwater, H. A. *Phys. Rev. B* **2003**, *67*, No. 205402.
(260) Auguie', B.; Barnes, W. L. *Phys. Rev. Lett.* **2008**, *101*, No. 143902.
(261) Giannini, V.; Vecchi, G.; Gomez-Rivas, J. *Phys. Rev. Lett.* **2010**, *105*, No. 266801.
(262) (a) Vecchi, G.; Giannini, V.; Gomez-Rivas, J. *Phys. Rev. Lett.* **2009**, *102*, No. 146807. (b) Chu, Y.; Schonbrun, E.; Yang, T.; Crozier, K. B. *Appl. Phys. Lett.* **2008**, *93*, 181108.
(263) Guffey, M. J.; Scherer, N. F. *Nano Lett.* **2010**, *10*, 4302.
(264) Urban, A. S.; Lutich, A. A.; Stefani, F. D.; Feldmann, J. *Nano Lett.* **2010**, *10*, 4794.
(265) Kraus, T.; Malaquin, L.; Schmid, H.; Riess, W.; Spencer, N. D.; Wolf, H. *Nature Nanotechnol.* **2007**, *2*, 570.
(266) Zou, S.; Schatz, G. C. *J. Chem. Phys.* **2004**, *121*, 12606.
(267) Brongersma, M. L.; Hartman, J. W.; Atwater, H. A. *Phys. Rev. B* **2000**, *62*, No. R16356.
(268) Quinten, M.; Leitner, A.; Krenn, J. R.; Aussenegg, F. R. *Opt. Lett.* **1998**, *23*, 1331.
(269) Zou, S.; Schatz, G. C. *Phys. Rev. B* **2006**, *74*, No. 125111.
(270) Nomura, W.; Ohtsu, M.; Yatsui, T. *Appl. Phys. Lett.* **2005**, *86*, No. 181108.
(271) Maier, S. A.; Brongersma, M. L.; Kik, P. G.; Atwater, H. A. *Phys. Rev. B* **2002**, *65*, No. 193408.
(272) Maier, S. A.; Brongersma, M. L.; Kik, P. G.; Meltzer, S.; Requicha, A. A. G.; Atwater, H. A. *Adv. Mater.* **2001**, *13*, 1501.
(273) Alu, A.; Engheta, N. *Phys. Rev. B* **2006**, *74*, No. 205436.
(274) Kawata, S.; Ono, A.; Verma, P. *Nat. Photonics* **2008**, *2*, 438.
(275) Malyshev, A. V.; Malyshev, V. A.; Knoester, J. *Nano Lett.* **2008**, *8*, 2369.
(276) Sukharev, M.; Seideman, T. *Nano Lett.* **2006**, *6*, 715.
(277) Nordlander, P. *Nat. Photonics* **2008**, *2*, 387.
(278) Bouhelier, A.; Bachelot, R.; Im, J. S.; Wiederrecht, G. P.; Lerondel, G.; Kostcheev, S.; Royer, P. *J. Phys. Chem. B* **2005**, *109*, 3195.
(279) (a) Citrin, D. S. *Nano Lett.* **2004**, *4*, 1561. (b) Citrin, D. S. *Nano. Lett.* **2005**, *5*, 985.
(280) Fung, K. H.; Chan, C. T. *Opt. Commun.* **2008**, *281*, 855.
(281) Govyadinov, A. A.; Markel, V. A. *Phys. Rev. B* **2008**, *78* No. 035403.
(282) Koenderink, A. F.; Polman, A. *Phys. Rev. B* **2006**, *74*, No. 033402.

(283) Simovski, C. R.; Viitanen, A. J.; Tretyakov, S. A. *Phys. Rev. E* **2005**, *72*, No. 066606.
(284) Park, S. Y.; Stroud, D. *Phys. Rev. B* **2004**, *69*, No. 125418.
(285) Weber, W. H.; Ford, G. W. *Phys. Rev. B* **2004**, *70*, No. 125429.
(286) Alu, A.; Engheta, N. *Phys. Rev. B* **2009**, *79*, No. 235412.
(287) Crozier, K. B.; Togan, E.; Simsek, E.; Yang, T. *Opt. Express* **2007**, *15*, 17482.
(288) Quidant, R.; Girard, C.; Weeber, J.-C.; Dereux, A. *Phys. Rev. B* **2004**, *69*, No. 085407.
(289) Markel, V. A.; Sarychev, A. K. *Phys. Rev. B* **2007**, *75*, No. 085426.
(290) Citrin, D. S. *J. Opt. Soc. Am. B* **2005**, *22*, 1763.
(291) Stockman, M. I.; Faleev, S. V.; Bergman, D. J. *Phys. Rev. Lett.* **2001**, *87*, No. 167401.
(292) Liu, M.; Lee, T.-W.; Gray, S. K.; Guyot-Sionnest, P.; Pelton, M. *Phys. Rev. Lett.* **2009**, *102*, No. 107401.
(293) Hernandez, J. V.; Noordam, L. D.; Robicheaux, F. *J. Phys. Chem. B* **2005**, *109*, 15808.
(294) Alu, A.; Belov, P. A.; Engheta, N. *Phys. Rev. B* **2009**, *80* No. 113101.
(295) Bergman, D. J.; Stockman, M. I. *Phys. Rev. Lett.* **2003**, *90* No. 027402.
(296) Gather, M. C.; Meerholz, K.; Danz, N.; Leosson, K. *Nat. Photonics* **2010**, *4*, 457.
(297) Oulton, R. F.; Sorger, V. J.; Zentgraf, T.; Ma, R. M.; Gladden, C.; Dai, L.; Bartal, G.; Zhang, X. *Nature* **2009**, *461*, 629.
(298) Seidel, J.; Grafström, S.; Eng, L. *Phys. Rev. Lett.* **2005**, *94* No. 177401.
(299) Li, H.; Rothberg, L. *Proc. Nat. Acad. Sci. U.S.A.* **2004**, *101*, 14036.
(300) Pileni, M. P. *J. Phys. Chem. B* **2001**, *105*, 3358.
(301) Chen, C.-F.; Tzeng, S.-D.; Chen, H.-Y.; Lin, K.-J.; Gwo, S. *J. Am. Chem. Soc.* **2007**, *130*, 824.
(302) Tao, A. R.; Huang, J.; Yang, P. *Acc. Chem. Res.* **2008**, *41*, 1662.
(303) Evanoff, D. D., Jr.; Chumanow, G. *ChemPhysChem* **2005**, *6*, 1221.
(304) Collier, C. P.; Saykally, R. J.; Shiang, J. J.; Henrichs, S. E.; Heath, J. R. *Science* **1997**, *277*, 1978.
(305) Tang, Z.; Kotov, N. A. *Adv. Mater.* **2005**, *17*, 951.
(306) Marinakos, S. M.; Brousseau, L. C., III; Jones, A.; Feldheim, D. L. *Chem. Mater.* **1998**, *10*, 1214.
(307) Sawitowski, T.; Miquel, Y.; Heilmann, A.; Schmid, G. *Adv. Funct. Mater.* **2001**, *11*, 435.
(308) Yin, Y.; Lu, Y.; Gates, B.; Xia, Y. *J. Am. Chem. Soc.* **2001**, *123*, 8718.
(309) Kang, Y. *Chem. Lett.* **2008**, *37*, 874.
(310) Zeng, J.; Huang, J.; Lu, W.; Wang, X.; Wang, B.; Zhang, S.; Hou, J. *Adv. Mater.* **2007**, *79*, 2172.
(311) Hermanson, K. D.; Lumsdon, S. O.; Williams, J. P.; Kaler, E. W.; Velev, O. D. *Science* **2001**, *294*, 1082.
(312) Hu, X.; Cheng, W.; Wang, T.-J.; Wang, E.; Dong, S. *Nanotechnology* **2005**, *16*, 2164.
(313) Joseph, S. T. S.; Ipe, B. I.; Pramod, P.; Thomas, K. G. *J. Phys. Chem. B* **2006**, *110*, 150.
(314) Sardar, R.; Shumaker-Parry, J. S. *Nano Lett.* **2008**, *8*, 731.
(315) DeVries, G. A.; Brunnbauer, M.; Hu, Y.; Jackson, A. M.; Long, B.; Neltner, B. T.; Uzun, O.; Wunsch, B. H.; Stellacci, F. *Science* **2007**, *315*, 358.
(316) Novak, J. P.; Feldheim, D. L. *J. Am. Chem. Soc.* **2000**, *122*, 3979.
(317) Zhang, S.; Kou, X.; Yang, Z.; Shi, Q.; Stucky, G. D.; Sun, L.; Wang, J.-K.; Yan, C. *Chem. Commun.* **2007**, 1816.
(318) Hussain, I.; Brust, M.; Barauskas, J.; Cooper Andrew, I. *Langmuir* **2009**, *25*, 1934.
(319) Mirin, N. A.; Hainey, M., Jr; Halas, N. J. *Adv. Mater.* **2008**, *20*, 535.
(320) Lee, J.; Hasan, W.; Lee, M. H.; Odom, T. W. *Adv. Mater.* **2007**, *19*, 4387.
(321) Lin, S.; Li, M.; Dujardin, E.; Girard, C.; Mann, S. *Adv. Mater.* **2005**, *17*, 2553.
(322) Zhang, H.; Fung, K.-H.; Hartmann, J.; Chan, C. T.; Wang, D. *J. Phys. Chem. C* **2008**, *112*, 16830.
(323) Mulvaney, P.; Liz-Marzan, L. M.; Giersig, M.; Ung, T. *J. Mater. Chem.* **2000**, *10*, 1259.
(324) Chen, C.-L.; Zhang, P.; Rosi, N. L. *J. Am. Chem. Soc.* **2008**, *130*, 13555.
(325) Thomas, K. G.; Barazzouk, S.; Ipe, B. I.; Joseph, S. T. S. J.; Kamat, P. V. *J. Phys. Chem. B* **2004**, *108*, 13066.
(326) Caswell, K. K.; Wilson, J. N.; Bunz, U. H. F.; Murphy, C. J. *J. Am. Chem. Soc.* **2003**, *125*, 13914.
(327) Nie, Z.; Fava, D.; Kumacheva, E.; Zou, S.; Walker, G. C.; Rubinstein, M. *Nat. Mater.* **2007**, *6*, 609.
(328) Liu, K.; Nie, Z.; Zhao, N.; Li, W.; Rubinstein, M.; Kumacheva, E. *Science* **2010**, *329*, 197.
(329) Bunz, U. H. F. *Adv. Mater.* **2006**, *18*, 973.
(330) Khanal, B. P.; Zubarev, E. R. *Angew. Chem., Int. Ed.* **2007**, *46*, 2195.
(331) Bonell, F.; Sanchot, A.; Dujardin, E.; Pechou, R.; Girard, C.; Li, M.; Mann, S. *J. Chem. Phys.* **2009**, *130*, No. 034702.
(332) Sendroiu, I. E.; Mertens, S. F. L.; Schiffrin, D. J. *Phys. Chem. Chem. Phys.* **2006**, *8*, 1430.
(333) Zhong, Z.; Patskovskyy, S.; Bouvrette, P.; Luong, J. H. T.; Gedanken, A. *J. Phys. Chem. B* **2004**, *108*, 4046.
(334) Girard, C.; Dujardin, E.; Li, M.; Mann, S. *Phys. Rev. Lett.* **2006**, *97*, No. 100801.
(335) Khlebtsov, B.; Zharov, V.; Melnikov, A.; Tuchin, V.; Khlebtsov, N. *Nanotechnology* **2006**, *17*, 5167.
(336) Moerner, W. E.; Fromm, D. P. *Rev. Sci. Instrum.* **2003**, *74*, 3597.
(337) Moerner, W. E.; Orrit, M. *Science* **1999**, *283*, 1670.
(338) Hu, M.; Chen, J.; Marquez, M.; Xia, Y.; Hartland, G. V. *J. Phys. Chem. C* **2007**, *111*, 12558.
(339) Jin, R.; Jureller, J. E.; Kim, H. Y.; Scherer, N. F. *J. Am. Chem. Soc.* **2005**, *127*, 12482.
(340) Jin, R.; Jureller, J. E.; Scherer, N. F. *Appl. Phys. Lett.* **2006**, *88*, No. 263111.
(341) Hu, M.; Novo, C.; Funston, A.; Wang, H.; Staleva, H.; Zon, S.; Mulvaney, P.; Xia, Y.; Hartland, G. V. *J. Mater. Chem.* **2008**, *18*, 1949.
(342) Mock, J. J.; Barbic, M.; Smith, D. R.; Schultz, D. A.; Schultz, S. *J. Chem. Phys.* **2002**, *116*, 6755.
(343) Novo, C.; Funston, A. M.; Pastoriza-Santos, I.; Liz-Marzan, L. M.; Mulvaney, P. *Angew. Chem., Int. Ed.* **2007**, *46*, 3517.
(344) Munechika, K.; Smith, J. M.; Chen, Y.; Ginger, D. S. *J. Phys. Chem. C* **2007**, *111*, 18906.
(345) McMahon, J. M.; Wang, Y.; Sherry, L. J.; Van Duyne, R. P.; Marks, L. D.; Gray, S. K.; Schatz, G. C. *J. Phys. Chem. C* **2009**, *113*, 2731.
(346) Chang, W. S.; Ha, J. W.; Slaughter, L. S.; Link, S. *Proc. Natl. Acad. Sci. U.S.A.* **2010**, *107*, 2781.
(347) Slaughter, L. S.; Chang, W.-S.; Swanglap, P.; Tcherniak, A.; Khanal, B. P.; Zubarev, E. R.; Link, S. *J. Phys. Chem. C* **2010**, *114*, 4934.
(348) Lee, J.; Hasan, W.; Stender, C. L.; Odom, T. W. *Acc. Chem. Res.* **2008**, *41*, 1762.
(349) Kang, Y.; Erickson Kris, J.; Taton, T. A. *J. Am. Chem. Soc.* **2005**, *127*, 13800.
(350) Chang, W.-S.; Slaughter, L. S.; Khanal, B. P.; Manna, P.; Zubarev, E. R.; Link, S. *Nano Lett.* **2009**, *9*, 1152.
(351) Pérez-Juste, J.; Pastoriza-Santos, I.; Liz-Marzán, L. M.; Mulvaney, P. *Coord. Chem. Rev.* **2005**, *249*, 1870.
(352) Encina, E. R.; Coronado, E. A. *J. Phys. Chem. C* **2007**, *111*, 16796.
(353) Khlebtsov, B. N.; Khlebtsov, N. G. *J. Phys. Chem. C* **2007**, *111*, 11516.
(354) Gunn, J. M.; Ewald, M.; Dantus, M. *Nano Lett.* **2006**, *6*, 2804.
(355) Krenn, J. R.; Schider, G.; Rechberger, W.; Lamprecht, B.; Leitner, A.; Aussenegg, F. R.; Weeber, J. C. *Appl. Phys. Lett.* **2000**, *77*, 3379.

(356) Wei, H.; Reyes-Coronado, A.; Nordlander, P.; Aizpurua, J.; Xu, H. *ACS Nano* **2010**, *4*, 2649.
(357) Bryant, G. W.; Garcıa de Abajo, F. J.; Aizpurua, J. *Nano Lett.* **2008**, *8*, 631.
(358) (a) Payne, E. K.; Shuford, K. L.; Park, S.; Schatz, G. C.; Mirkin, C. A. *J. Phys. Chem. B* **2006**, *110*, 2150. (b) Kim, S.; Shuford, K. L.; Bok, H.-M.; Kim, S. K.; Park, S. *Nano. Lett.* **2008**, *8*, 800.
(359) Imura, K.; Nagahara, T.; Okamoto, H. *J. Am. Chem. Soc.* **2004**, *126*, 12730.
(360) Imura, K.; Nagahara, T.; Okamoto, H. *J. Phys. Chem. B* **2004**, *108*, 16344.
(361) Okamoto, H.; Imura, K. *J. Mater. Chem.* **2006**, *16*, 3920.
(362) Vesseur, E. J. R.; De Waele, R.; Kuttge, M.; Polman, A. *Nano Lett.* **2007**, *7*, 2843.
(363) Douillard, L.; Charra, F.; Fiorini, C.; Adam, P. M.; Bachelot, R.; Kostcheev, S.; Lerondel, G.; Lamy de la Chapelle, M.; Royer, P. *J. Appl. Phys.* **2007**, *101*, No. 083518.
(364) Douillard, L.; Charra, F.; Korczak, Z.; Bachelot, R.; Kostcheev, S.; Lerondel, G.; Adam, P.-M.; Royer, P. *Nano Lett.* 2008, *8*, 935.
(365) Novotny, L. *Phys. Rev. Lett.* **2007**, *98*, No. 266802.
(366) Schaich, W. L.; Schider, G.; Krenn, J. R.; Leitner, A.; Aussenegg, F. R.; Puscasu, I.; Monacelli, B.; Boreman, G. *Appl. Opt.* **2003**, *42*, 5714.
(367) Schider, G.; Krenn, J. R.; Hohenau, A.; Ditlbacher, H.; Leitner, A.; Aussenegg, F. R. *Phys. Rev. B* **2003**, *68*, No. 155427.
(368) Neubrech, F.; Weber, D.; Lovrincic, R.; Pucci, A.; Lopes, M.; Toury, T.; Chapelle, d. L.; Lamy, M. *Appl. Phys. Lett.* **2008**, *93* No. 163105.
(369) Aizpurua, J.; Bryant, G. W.; Richter, L. J.; de Abajo, F. J. G.; Kelley, B. K.; Mallouk, T. *Phys. Rev. B* **2005**, *71*, No. 235420.
(370) Schmucker, A. L.; Harris, N.; Banholzer, M. J.; Blaber, M. G.; Osberg, K. D.; Schatz, G. C.; Mirkin, C. A. *ACS Nano* **2010**, *4*, 5453.
(371) Jana, N. R.; Gearheart, L.; Murphy, C. J. *J. Phys. Chem. B* **2001**, *105*, 4065.
(372) Murphy, C. J.; Sau, T. K.; Gole, A. M.; Orendorff, C. J.; Gao, J.; Gou, L.; Hunyadi, S. E.; Li, T. *J. Phys. Chem. B* **2005**, *109*, 13857.
(373) Nikoobakht, B.; El-Sayed, M. A. *Chem. Mater.* **2003**, *15*, 1957.
(374) Lamprecht, B.; Krenn, J. R.; Schider, G.; Ditlbacher, H.; Salerno, M.; Felidj, N.; Leitner, A.; Aussenegg, F. R.; Weeber, J. C. *Appl. Phys. Lett.* **2001**, *79*, 51.
(375) Charbonneau, R.; Berini, P.; Berolo, E.; Lisicka-Shrzek, E. *Opt. Lett.* **2000**, *25*, 844.
(376) Leosson, K.; Nikolajsen, T.; Boltasseva, A.; Bozhevolnyi, S. I. *Opt. Express* **2006**, *14*, 314.
(377) Sandtke, M.; Engelen, R. J. P.; Schoenmaker, H.; Attema, I.; Dekker, A.; Cerjak, I.; Korterik, J. P.; Segerink, F. B.; Kuipers, L. *Rev. Sci. Instrum.* **2008**, *79*, No. 013704.
(378) Zia, R.; Selker, M. D.; Brongersma, M. L. *Phys. Rev. B* **2005**, *71*, No. 165431.
(379) Dickson, R. M.; Lyon, L. A. *J. Phys. Chem. B* **2000**, *104*, 6095.
(380) Sanders, A. W.; Routenberg, D. A.; Wiley, B. J.; Xia, Y.; Dufresne, E. R.; Reed, M. A. *Nano Lett.* **2006**, *6*, 1822.
(381) Staleva, H.; Skrabalak, S. E.; Carey, C. R.; Kosel, T.; Xia, Y.; Hartland, G. V. *Phys. Chem. Chem. Phys.* **2009**, *11*, 5889.
(382) Pyayt, A. L.; Wiley, B.; Xia, Y.; Chen, A.; Dalton, L. *Nat. Nanotechnol.* **2008**, *3*, 660.
(383) Hutchison, J. A.; Centeno, S. P.; Odaka, H.; Fukumura, H.; Hofkens, J.; Uji-i, H. *Nano Lett.* **2009**, *9*, 995.
(384) Fang, Y. R.; Wei, H.; Hao, F.; Nordlander, P.; Xu, H. *Nano Lett.* **2009**, *9*, 2049.
(385) Ditlbacher, H.; Hohenau, A.; Wagner, D.; Kreibig, U.; Rogers, M.; Hofer, F.; Aussenegg, F. R.; Krenn, J. R. *Phys. Rev. Lett.* **2005**, *95*, No. 257403.
(386) Yan, R. X.; Pausauskie, P.; Huang, J. X.; Yang, P. D. *Proc. Natl. Acad. Sci. U.S.A.* **2009**, *106*, 21045.
(387) (a) Li, Z. P.; Shegai, T.; Haran, G.; Xu, H. X. *ACS Nano* **2009**, *3*, 637. (b) Li, Z. P.; Hao, F.; Huang, Y. Z.; Fang, Y. R.; Nordlander, P.; Xu, H. X. *Nano Lett.* **2009**, *9*, 4383.
(388) Tran, M. L.; Centeno, S. P.; Hutchison, J. A.; Engelkamp, H.; Liang, D.; van Tendeloo, G.; Sels, B. F.; Hofkens, J.; Uji-i, H. *J. Am. Chem. Soc.* **2008**, *130*, 17240.
(389) Allione, M.; Temnov, V. V.; Fedutik, Y.; Woggon, U.; Artemyev, M. V. *Nano Lett.* **2008**, *8*, 31.
(390) Tang, Y.; Ouyang, M. *Nat. Mater.* **2007**, *6*, 754.
(391) Graff, A.; Wagner, D.; Ditlbacher, H.; Kreibig, U. *Eur. Phys. J. D* **2005**, *34*, 263.
(392) Bouhelier, A.; Huser, T. R.; Tamaru, H.; Guentherodt, H.-J.; Pohl, D. W.; Baida, F. I.; Van Labeke, D. *Phys. Rev. B* **2001**, *63* No. 155404.
(393) Smolyaninov, I. I.; Mazzoni, D. L.; Mait, J.; Davis, C. C. *Phys. Rev. B* **1997**, *56*, 1601.
(394) Guo, X.; Qiu, M.; Bao, J.; Wiley, B. J.; Yang, Q.; Zhang, X.; Ma, Y.; Yu, H.; Tong, L. *Nano Lett.* **2009**, *9*, 4515.
(395) Wiley, B. J.; Lipomi, D. J.; Bao, J.; Capasso, F.; Whitesides, G. M. *Nano Lett.* **2008**, *8*, 3023.
(396) Dorfmueller, J.; Vogelgesang, R.; Weitz, R. T.; Rockstuhl, C.; Etrich, C.; Pertsch, T.; Lederer, F.; Kern, K. *Nano Lett.* **2009**, *9*, 2372.
(397) Verhagen, E.; Spasenovic, M.; Polman, A.; Kuipers, L. *Phys. Rev. Lett.* **2009**, *102*, No. 203904.
(398) Ma, Y.; Li, X.; Yu, H.; Tong, L.; Gu, Y.; Gong, Q. *Opt. Lett.* **2010**, *35*, 1160.
(399) Ditlbacher, H.; Krenn, J. R.; Felidj, N.; Lamprecht, B.; Schider, G.; Salerno, M.; Leitner, A.; Aussenegg, F. R. *Appl. Phys. Lett.* **2002**, *80*, 404.
(400) Solis, D., Jr.; Chang, W.-S.; Khanal, B. P.; Bao, K.; Nordlander, P.; Zubarev, E. R.; Link, S. *Nano Lett.* **2010**, *10*, 3482.
(401) Akimov, A. V.; Mukherjee, A.; Yu, C. L.; Chang, D. E.; Zibrov, A. S.; Hemmer, P. R.; Park, H.; Lukin, M. D. *Nature* **2007**, *450*, 402.
(402) Fedutik, Y.; Temnov, V. V.; Schops, O.; Woggon, U.; Artemyev, M. V. *Phys. Rev. Lett.* **2007**, *99*, No. 136802.
(403) Chang, D. E.; Soerensen, A. S.; Hemmer, P. R.; Lukin, M. D. *Phys. Rev. B* **2007**, *76*, No. 035420.
(404) Lee, J.; Hernandez, P.; Lee, J.; Govorov, A. O.; Kotov, N. A. *Nat. Mater.* **2007**, *6*, 291.
(405) Fang, Y. R.; Li, Z.; Huang, Y.; Zhang, S.; Nordlander, P.; Halas, N. J.; Xu, H. *Nano Lett.* **2010**, *10*, 1950.
(406) Miroshnichenko, A. E.; Flach, S.; Kivshar, Y. S. *Rev. Mod. Phys.* **2010**, *82*, 2257.
(407) Luk'yanchuk, B.; Zheludev, N. I.; Maier, S. A.; Halas, N. J.; Nordlander, P.; Giessen, H.; Chong, C. T. *Nat. Mater.* **2010**, *9*, 707.
(408) Alzar, C. L. G.; Martinez, M. A. G.; Nussenzveig, P. *Am. J. Phys.* **2002**, *70*, 37.
(409) Ruan, Z. C.; Fan, S. H. *J. Phys. Chem. C* **2010**, *114*, 7324.
(410) Ruan, Z. C.; Fan, S. H. *Phys. Rev. Lett.* **2010**, *105*, No. 013901.
(411) Hao, Q. Z.; Juluri, B. K.; Zheng, Y. B.; Wang, B.; Chiang, I. K.; Jensen, L.; Crespi, V.; Eklund, P. C.; Huang, T. J. *J. Phys. Chem. C* **2010**, *114*, 18059.
(412) Pakizeh, T.; Langhammer, C.; Zoric, I.; Apell, P.; Käll, M. *Nano Lett.* **2009**, *9*, 882.
(413) Kelly, K. L.; Coronado, E.; Zhao, L. L.; Schatz, G. C. *J. Phys. Chem. B* **2003**, *107*, 668.
(414) Grady, N. K.; Halas, N. J.; Nordlander, P. *Chem. Phys. Lett.* **2004**, *399*, 167.
(415) Chu, M. W.; Myroshnychenko, V.; Chen, C. H.; Deng, J. P.; Mou, C. Y.; de Abajo, F. J. G. *Nano Lett.* **2009**, *9*, 399.
(416) Koh, A. L.; Bao, K.; Khan, I.; Smith, W. E.; Kothleitner, G.; Nordlander, P.; Maier, S. A.; McComb, D. W. *ACS Nano* **2009**, *3*, 3015.
(417) Maier, S. A. *Nat. Mater.* **2009**, *8*, 699.
(418) Stockman, M. I. *Nature* **2010**, *467*, 541.
(419) Miroshnichenko, A. E. *Phys. Rev. A* **2010**, *81*, No. 053818.
(420) Kante, B.; de Lustrac, A.; Lourtioz, J. M. *Phys. Rev. B* **2009**, *80*, No. 035108.
(421) Pinchuk, A. O.; Schatz, G. C. *Appl. Phys. B* **2008**, *93*, 31.
(422) Hao, F.; Larsson, E. M.; Ali, T. A.; Sutherland, D. S.; Nordlander, P. *Chem. Phys. Lett.* **2008**, *458*, 262.

(423) Hao, F.; Nordlander, P.; Burnett, M. T.; Maier, S. A. *Phys. Rev. B* **2007**, *76*, No. 245417.
(424) Hao, F.; Sonnefraud, Y.; Van Dorpe, P.; Maier, S. A.; Halas, N. J.; Nordlander, P. *Nano Lett.* **2008**, *8*, 3983.
(425) Sonnefraud, Y.; Verellen, N.; Sobhani, H.; Vandenbosch, G. A. E.; Moshchalkov, V. V.; Van Dorpe, P.; Nordlander, P.; Maier, S. A. *ACS Nano* **2010**, *4*, 1664.
(426) Bachelier, G.; Russier-Antoine, I.; Benichou, E.; Jonin, C.; Del Fatti, N.; Vallee, F.; Brevet, P. F. *Phys. Rev. Lett.* **2008**, *101*, No. 197401.
(427) Brown, L. V.; Sobhani, H.; Lassiter, J. B.; Nordlander, P.; Halas, N. J. *ACS Nano* **2010**, *4*, 819.
(428) Zhang, S. P.; Bao, K.; Halas, N. J.; Xu, H. X.; Nordlander, P. *Nano Lett* **2011**, *11*, 1657.
(429) Ortuno, R.; Garcia-Meca, C.; Rodriguez-Fortuno, F. J.; Martinez, A. *Opt. Lett.* **2010**, *35*, 4205.
(430) Ziegler, J. I.; Haglund, R. F. *Nano Lett.* **2010**, *10*, 3013.
(431) Liu, H.; Li, T.; Wang, S. M.; Zhu, S. N. *Front. Phys. China* **2010**, *5*, 277.
(432) Kang, B.; Choi, E.; Lee, H. H.; Kim, E. S.; Woo, J. H.; Kim, J.; Hong, T. Y.; Kim, J. H.; Wu, J. W. *Opt. Express* **2010**, *18*, 11552.
(433) Geiselmann, M.; Utikal, T.; Lippitz, M.; Giessen, H. *Phys. Rev. B* **2010**, *81*, No. 235101.
(434) Vallecchi, A.; Campione, S.; Capolino, F. *J. Nanophotonics* **2010**, *4*, No. 041577.
(435) Neubrech, F.; Garcia-Etxarri, A.; Weber, D.; Bochterle, J.; Shen, H.; de la Chapelle, M. L.; Bryant, G. W.; Aizpurua, J.; Pucci, A. *Appl. Phys. Lett.* **2010**, *96*, No. 213111.
(436) Gomez, D. E.; Vernon, K. C.; Davis, T. J. *Phys. Rev. B* **2010**, *81*, No. 075414.
(437) Su, X. R.; Zhang, Z. S.; Zhang, L. H.; Li, Q. Q.; Chen, C. C.; Yang, Z. J.; Wang, Q. Q. *Appl. Phys. Lett.* **2010**, *96*, No. 043113.
(438) Ye, J.; Van Dorpe, P.; Van Roy, W.; Borghs, G.; Maes, G. *Langmuir* **2009**, *25*, 1822.
(439) Zhang, Z.; Weber-Bargioni, A.; Wu, S. W.; Dhuey, S.; Cabrini, S.; Schuck, P. J. *Nano Lett.* **2009**, *9*, 4505.
(440) Bitzer, A.; Wallauer, J.; Helm, H.; Merbold, H.; Feurer, T.; Walther, M. *Opt. Express* **2009**, *17*, 22108.
(441) Zharov, A. A.; Noskov, R. E.; Tsarev, M. V. *J. Appl. Phys.* **2009**, *106*, No. 073104.
(442) Zhang, S.; Genov, D. A.; Wang, Y.; Liu, M.; Zhang, X. *Phys. Rev. Lett.* **2008**, *101*, No. 047401.
(443) Dong, Z. G.; Liu, H.; Xu, M. X.; Li, T.; Wang, S. M.; Cao, J. X.; Zhu, S. N.; Zhang, X. *Opt. Express* **2010**, *18*, 22412.
(444) Dong, Z. G.; Liu, H.; Xu, M. X.; Li, T.; Wang, S. M.; Zhu, S. N.; Zhang, X. *Opt. Express* **2010**, *18*, 18229.
(445) Jin, X.; Lu, Y.; Zheng, H.; Lee, Y.; Rhee, J. Y.; Jang, W. H. *Opt. Express* **2010**, *18*, 13396.
(446) Chen, Y. T.; Chern, R. L.; Lin, H. Y. *Appl. Opt.* **2010**, *49*, 2819.
(447) Liu, N.; Weiss, T.; Mesch, M.; Langguth, L.; Eigenthaler, U.; Hirscher, M.; Sonnichsen, C.; Giessen, H. *Nano Lett.* **2010**, *10*, 1103.
(448) Liu, N.; Langguth, L.; Weiss, T.; Kastel, J.; Fleischhauer, M.; Pfau, T.; Giessen, H. *Nat. Mater.* **2009**, *8*, 758.
(449) Verellen, N.; Sonnefraud, Y.; Sobhani, H.; Hao, F.; Moshchalkov, V. V.; Van Dorpe, P.; Nordlander, P.; Maier, S. A. *Nano Lett.* **2009**, *9*, 1663.
(450) Hao, F.; Nordlander, P.; Sonnefraud, Y.; Van Dorpe, P.; Maier, S. A. *ACS Nano* **2009**, *3*, 643.
(451) Liu, N.; Fu, L. W.; Kaiser, S.; Schweizer, H.; Giessen, H. *Adv. Mater.* **2008**, *20*, 3859.
(452) Christ, A.; Martin, O. J. F.; Ekinci, Y.; Gippius, N. A.; Tikhodeev, S. G. *Nano Lett.* **2008**, *8*, 2171.
(453) Aydin, K.; Pryce, I. M.; Atwater, H. A. *Opt. Express* **2010**, *18*, 13407.
(454) Pryce, I. M.; Aydin, K.; Kelaita, Y. A.; Briggs, R. M.; Atwater, H. A. *Nano Lett.* **2010**, *10*, 4222.
(455) Verellen, N.; Dorpe, P. V.; Huang, C.; Lodewijks, K.; Vandenbosch, G. A. E.; lagae, L.; Moschalkov, V. V. *Nano Lett.* **2011**, *11*, 391.
(456) Wang, H.; Wu, Y. P.; Lassiter, B.; Nehl, C. L.; Hafner, J. H.; Nordlander, P.; Halas, N. J. *Proc. Natl. Acad. Sci. U.S.A.* **2006**, *103*, 10856.
(457) Fan, J. A.; Bao, K.; Wu, C.; Bao, J.; Bardhan, R.; Halas, N. J.; Manoharan, V. N.; Shvets, G.; Nordlander, P.; Capasso, F. *Nano Lett.* **2010**, 4680.
(458) Le, F.; Brandl, D. W.; Urzhumov, Y. A.; Wang, H.; Kundu, J.; Halas, N. J.; Aizpurua, J.; Nordlander, P. *ACS Nano* **2008**, *2*, 707.
(459) Bao, K.; Mirin, N. A.; Nordlander, P. *Appl. Phys. A: Mater. Sci. Process.* **2010**, *100*, 333.
(460) Lassiter, J. B.; Sobhani, H.; Fan, J. A.; Kundu, J.; Capasso, F.; Nordander, P.; Halas, N. J. *Nano Lett.* **2010**, *10*, 3184.
(461) Hentschel, M.; Saliba, M.; Vogelgesang, R.; Giessen, H.; Alivisatos, A. P.; Liu, N. *Nano Lett.* **2010**, *10*, 2721.
(462) Fan, J. A.; Wu, C. H.; Bao, K.; Bao, J. M.; Bardhan, R.; Halas, N. J.; Manoharan, V. N.; Nordlander, P.; Shvets, G.; Capasso, F. *Science* **2010**, *328*, 1135.
(463) Mirin, N. A.; Bao, K.; Nordlander, P. *J. Phys. Chem. A* **2009**, *113*, 4028.
(464) Zhang, W.; Gallinet, B.; Martin, O. J. F. *Phys. Rev. B* **2010**, *81*, No. 233407.
(465) Albrecht, M. G.; Creighton, J. A. *J. Am. Chem. Soc.* **1977**, *99*, 5215.
(466) Muskens, O. L.; Giannini, V.; Sánchez-Gil, J. A.; Rivas, J. G. *Nano Lett.* **2007**, *7*, 2871.
(467) Kinkhabwala, A.; Yu, Z.; Fan, S.; Avlasevich, Y.; Müllen, K.; Moerner, W. E. *Nat. Photonics* **2009**, 654.
(468) (a) Lal, S.; Grady, N. K.; Kundu, J.; Levin, C. S.; Lassiter, J. B.; Halas, N. J. *Chem. Soc. Rev.* **2008**, *37*, 898. (b) Lal, S.; Clare, S. E.; Halas, N. J. *Acc. Chem. Res.* **2008**, *41*, 1842.
(469) Peer, D.; Karp, J. M.; Hong, S.; Farokhzad, O. C.; Margalit, R.; Langer, R. *Nat. Nanotechnol.* **2007**, *2*, 751.
(470) Zia, R.; Schuller, J. A.; Chandran, A.; Brongersma, M. L. *Mater. Today* **2006**, *9*, 20.
(471) Stewart, M. E.; Anderton, C. R.; Thompson, L. B.; Maria, J.; Gray, S. K.; Rogers, J. A.; Nuzzo, R. G. *Chem. Rev.* **2008**, *108*, 494.
(472) Kennedy, D. C.; Tay, L. L.; Lyn, R. K.; Rouleau, Y.; Hulse, J.; Pezacki, J. P. *ACS Nano* **2009**, *3*, 2329.
(473) Sönnichsen, C.; Reinhard, B. M.; Liphardt, J.; Alivisatos, A. P. *Nat. Biotechnol.* **2005**, *23*, 741.
(474) Reinhard, B. M.; Yassif, J. M.; Vach, P.; Liphardt, J. In *Single Molecule Tools*, Methods in Enzymology, Vol 475; Elsevier Academic Press Inc: San Diego, 2010; Part B.
(475) Reinhard, B. M.; Sheikholeslami, S.; Mastroianni, A.; Alivisatos, A. P.; Liphardt, J. *Proc. Natl. Acad. Sci. U.S.A.* **2007**, *104*, 2667.
(476) Sannomiya, T.; Hafner, C.; Voros, J. *Opt. Lett.* **2009**, *34*, 2009.
(477) Mock, J. J.; Smith, D. R.; Schultz, S. *Nano Lett.* **2003**, *3*, 485.
(478) Grabar, K. C.; Freeman, R. G.; Hommer, M. B.; Natan, M. J. *Anal. Chem.* **1995**, *67*, 735.
(479) Hulteen, J. C.; Duyne, R. P. V. *J. Vac. Sci. Technol. A* **1995**, *13*, 1553.
(480) Bastys, V.; Pastoriza-Santos, I.; Rodríguez-González, B.; Vaisnoras, R.; Liz-Marzán, L. M. *Adv. Funct. Mater.* **2006**, *16*, 766.
(481) Sun, Y.; Mayers, B.; Xia, Y. *Adv. Mater.* **2003**, *15*, 641.
(482) Sun, Y. G.; Xia, Y. N. *Science* **2002**, *298*, 2176.
(483) Oldenburg, S. J.; Averitt, R. D.; Westcott, S. L.; Halas, N. J. *Chem. Phys. Lett.* **1998**, *288*, 243.
(484) Jackson, J. B.; Halas, N. J. *J. Phys. Chem. B* **2001**, *105*, 2743.
(485) Lee, S.; Mayer, K. M.; Hafner, J. H. *Anal. Chem.* **2009**, *81*, 4450.
(486) Nehl, C. L.; Hafner, J. H. *J. Mater. Chem.* **2008**, *18*, 2415.
(487) Nehl, C. L.; Liao, H. W.; Hafner, J. H. *Nano Lett.* **2006**, *6*, 683.
(488) Sherry, L. J.; Chang, S. H.; Schatz, G. C.; Van Duyne, R. P.; Wiley, B. J.; Xia, Y. N. *Nano Lett.* **2005**, *5*, 2034.
(489) Lal, S.; Link, S.; Halas, N. J. *Nat. Photonics* **2007**, *1*, 641.
(490) Liao, H.; Nehl, C. L.; Hafner, J. H. *Nanomedicine* **2006**, *1*, 201.
(491) Haes, A.; Van Duyne, R. P. *Anal. Bioanal. Chem.* **2004**, *379*, 920.
(492) El-Kashef, H. *Phys. B* **2000**, *279*, 295.

(493) Nie, S.; Emory, S. R. *Science* **1997**, *275*, 1102.
(494) Moskovits, M.; Jeong, D. H. *Chem. Phys. Lett.* **2004**, *397*, 91.
(495) Souza, G. R.; Levin, C. S.; Hajitou, A.; Pasqualini, R.; Arap, W.; Miller, J. H. *Anal. Chem.* **2006**, *78*, 6232.
(496) Vitol, E. A.; Orynbayeva, Z.; Bouchard, M. J.; Azizkhan-Clifford, J.; Friedman, G.; Gogotsi, Y. *ACS Nano* **2009**, *3*, 3529.
(497) Chourpa, I.; Lei, F. H.; Dubois, P.; Manfaita, M.; Sockalingum, G. D. *Chem. Soc. Rev.* **2008**, *37*, 993.
(498) Kneipp, J.; Kneipp, H.; McLaughlin, M.; Brown, D.; Kneipp, K. *Nano Lett.* **2006**, *6*, 2225.
(499) Kneipp, J.; Kneipp, H.; Wittig, B.; Kneipp, K. *Nanomedicine* **2010**, *6*, 214.
(500) Kneipp, J.; Kneipp, H.; Wittig, B.; Kneipp, K. *Nano Lett.* **2007**, *7*, 2819.
(501) Holze, R. *Electrochim. Acta* **1993**, *38*, 947.
(502) Kneipp, J.; Kneipp, H.; Wittig, B.; Kneipp, K. *J. Phys. Chem. C* **2010**, *114*, 7421.
(503) Bishnoi, S. W.; Rozell, C. J.; Levin, C. S.; Gheith, M. K.; Johnson, B. R.; Johnson, D. H.; Halas, N. J. *Nano Lett.* **2006**, *6*, 1687.
(504) Zeiri, L.; Bronk, B. V.; Shabtai, Y.; Eichler, J.; Efrima, S. *Appl. Spectrosc.* **2004**, *58*, 33.
(505) Schrader, B. *Infrared and Raman Spectroscopy: Methods and Applications*; VCH: Weinheim, New York, 1995.
(506) Adato, R.; Yanik, A. A.; Amsden, J. J.; Kaplan, D. L.; Omenetto, F. G.; Hong, M. K.; Erramilli, S.; Altug, H. *Proc. Natl. Acad. Sci. U.S.A.* **2009**, *106*, 19227.
(507) Neubrech, F.; Pucci, A.; Cornelius, T. W.; Karim, S.; Garcia-Etxarri, A.; Aizpurua, J. *Phys. Rev. Lett.* **2008**, *101*, No. 157403.
(508) Pucci, A.; Neubrech, F.; Weber, D.; Hong, S.; Toury, T.; de la Chapelle, M. L. *Phys. Status Solidi B* **2010**, *247*, 2071.
(509) Lawrence, B. D.; Omentetto, F. G.; Chi, K.; Kaplan, D. L. *J. Mater. Sci.* **2008**, *43*, 6967.
(510) Kundu, J.; Le, F.; Nordlander, P.; Halas, N. J. *Chem. Phys. Lett.* **2008**, *452*, 115.
(511) Wang, H.; Kundu, J.; Halas, N. J. *Angew. Chem., Int. Ed.* **2007**, *46*, 9040.